Numerical Modeling of Drug Delivery to Solid Tumor Microvasculature

by

Madjid Soltani

A thesis
presented to the University of Waterloo
in fulfillment of the
thesis requirement for the degree of
Doctor of Philosophy
in
Chemical Engineering

Waterloo, Ontario, Canada, 2013

I hereby declare that I am the sole author of this thesis. This is a true copy of the thesis, including any required final revisions, as accepted by my examiners.

I understand that my thesis may be made electronically available to the public.

Abstract

Modeling interstitial fluid flow involves processes such as fluid diffusion, convective transport in the extracellular matrix, and extravasation from blood vessels. In all of these processes, computational fluid dynamics can play a crucial role in elucidating the mechanisms of fluid flow in solid tumors and surrounding tissues. To date, microvasculature flow modeling has been most extensively studied with simple tumor shapes and their capillaries at different levels and scales. With our proposed numerical model, however, more complex and realistic tumor shapes and capillary networks can be studied.

First, a mathematical model of interstitial fluid flow is developed, based on the application of the governing equations for fluid flow, i.e., the conservation laws for mass and momentum, to physiological systems containing solid tumors. Simulations of interstitial fluid transport in a homogeneous solid tumor demonstrate that, in a uniformly perfused tumor, i.e., one with no necrotic region, the interstitial pressure distribution results in a non-uniform distribution of drug particles. Pressure distribution for different values of necrotic radii is examined, and two new parameters, the critical tumor radius and critical necrotic radius, are defined. In specific ranges of these critical dimensions the interstitial fluid pressure is relatively lower, which in turn leads to a diminished opposing force against drug movement and a subsequently higher drug concentration and potentially enhanced therapeutic effects.

In this work, the numerical model of fluid flow in solid tumors is further developed to incorporate and investigate non-spherical tumor shapes such as prolate and oblate ones. Using this enhanced model, tumor shape and size effects on drug delivery to solid tumors are then studied. Based on the assumption that drug particles flow with the interstitial fluid, the pressure and velocity maps of the latter are used to illustrate the drug delivery pattern in a solid tumor. Additionally, the effects of the surface area per unit volume of the tissue, as well as vascular and interstitial hydraulic conductivity on drug delivery efficiency, are investigated.

Using a tumor-induced microvasculature architecture instead of a uniform distribution of vessels provides a more realistic model of solid tumors. To this end, continuous and discrete mathematical models of angiogenesis were utilized to observe the effect of matrix density and matrix degrading enzymes on capillary network formation in solid tumors. Additionally, the interactions between matrix-degrading enzymes, the extracellular matrix and endothelial cells are mathematically modeled. Existing continuous and discrete models of angiogenesis were modified to impose the effect of matrix density on the solution. The imposition has been performed by a specific function in movement potential. Implementing realistic boundary and initial conditions showed that, unlike in previous models, the

endothelial cells accelerate as they migrate toward the tumor. Now, the tumor-induced microvasculature network can be applied to the model developed in Chapters 2 and 3.

Once the capillary network was set up, fluid flow in normal and cancerous tissues was numerically simulated under three conditions: constant and uniform distribution of intravascular pressure in the whole domain, a rigid vascular network, and an adaptable vascular network. First, governing equations of sprouting angiogenesis were implemented to specify the different domains for the network and interstitium. Governing equations for flow modeling were introduced for different domains. The conservation laws for mass and momentum, Darcys equation for tissue, and a simplified Navier Stokes equation for blood flow through capillaries were then used for simulating interstitial and intravascular flows. Finally, Starlings law was used to close this system of equations and to couple the intravascular and extravascular flows. The non-continuous behavior of blood and the adaptability of capillary diameter to hemodynamics and metabolic stimuli were considered in blood flow simulations through a capillary network. This approach provided a more realistic capillary distribution network, very similar to that of the human body.

This work describes the first study of flow modeling in solid tumors to realistically couple intravascular and extravascular flow through a network generated by sprouting angiogenesis, consisting of one parent vessel connected to the network. Other key factors incorporated in the model for the first time include capillary adaptation, non-continuous viscosity blood, and phase separation of blood flow in capillary bifurcation. Contrary to earlier studies which arbitrarily assumed veins and arteries to operate on opposite sides of a tumor network, the present approach requires the same vessel to run and from the network. Expanding the earlier models by introducing the outlined components was performed in order to achieve a more-realistic picture of blood flow through solid tumors. Results predict an almost doubled interstitial pressure and are in better agreement with human biology compared to the more simplified models generally in use today.

Acknowledgements

First of all, I would like to thank my supervisor, Professor Pu Chen. He has been many things to me in the past five years: mentor, motivator, teacher, and role model. He deserves special acknowledgement for instilling in me an appreciation for the art of presenting one's work to others.

I would like to express my gratitude to all members of my dissertation committee, Professors Ioannis (John) Chatzis, Ali Elkamel, Rajinder Pal from Chemical Engineering Department, Professor Mohammad Kohandel from Applied Math Department, and Professor Lance L. Munn, from Radiation Oncology Department at Harvard Medical School. Each has been a great source of input and constructive criticism. I value having such an array of insightful minds concerned about and interested in my research.

I would also like to express my sincere appreciation to Dr. Amy L. Bauer from Los Alamos National Laboratory, who provided me with substantial directional guidance in this research project and lots of help through these years.

I am deeply grateful to have interactions with so many excellent scientists over the past few years. In particular, I enjoyed enlightening discussions with Professor Axel R. Pries at Charit - Universittsmedizin Berlin, as well as interesting conversations on angiogenesis with Dr. Angelique Stephanou at the Institut de l'Ingnierie et de l'Information de Sant. I treasure my collaboration with Dr. Larry Baxter at Advanced Process Combinatorics, Inc. Special thanks to Professor Timothy W. Secomb, at the University of Arizona and his Colleague Dr. Ardith El-Kareh for helpful comments and discussions, and Professor Arthur Carty in WIN for endless support!

My colleagues and friends here at Waterloo have been a constant source of encouragement, assistance, friendship, and even amusement. Thanks must go to all of them. I would like to remember all people with whom I interacted with during my Ph.D. studies (the list would be too long and incomplete) for understanding, support, interest and affection, especially all my friends.

No acknowledgement would be complete without thanking my parents for their tremendous love and support in times past, present, and future, and for the countless opportunities that they provided for my educational, moral, and spiritual growth. Dad, if you were not willing to take some big risks for my education and development, I would have never made it this far. Dad, treasured in my heart you will stay, until we meet again someday, rest in peace in heaven. Mom, thanks for letting me grow up, and training me to make important decisions on my own. You are a special person that I love!

My siblings, relatives, and in-laws have always been very supportive of my education, and I especially appreciate the thought-provoking conversations I have had with them over the years on work, research, and family.

I owe a special debt to Mojtaba. I remember well all of our talks together, his enthusiasm, books given to me, and projects. The more I reflect, the more I remember how many subjects he made come alive for me. Thank you, Grandteacher.

I acknowledge the Ministry of Science and Research and Technology of Iran, and the Natural Sciences and Engineering Research Council of Canada (NSERC) for supporting me during these years at the Department of Chemical Engineering University of Waterloo and Waterloo Institute for Nanotechnology (WIN).

I would like to thank the University of Waterloo, Department of Chemical Engineering and WIN for making Waterloo such a great place to live and work. I would not be here without the effort of the faculty and the departmental staff. In particular, I would like to thank Liz, Rose, Judy, Lorna, and Dennis and all the others in the department who helped me navigate the whole Ph.D. process. Special thanks to Mary in the Writing Center!

Despite what everyone else has done for me, I dedicate this thesis to my wife, Zohreh Gharali. No one else has been so directly involved, or such a strong ally and supporter. She has helped me a lot and has remained supportive through lonely times of war-effort for a paper, test, or a conference. I look forward to many happy years with the woman I love.

There is one to whom I owe an even greater debt, which I can never repay. The God has been good to me. Though I have often let Him down by my own selfishness, stubbornness, and pride, He forgives and strengthens me. In the midst of frustration He is a comforter.

I hope I have made a good impression at the University of Waterloo. To any I have offended or hurt, please accept my apologies.

Dedication

To my dear son, Soroush, all my hope for the future.

Table of Contents

List of Tables

List of Figures

Nomenclature

IFP Interstitial fluid pressure

CFD Computational fluid dynamics

$MAbs$ Monoclonal Antibodies

GAG Glycosaminoglycans

μ Viscosity of the interstitial fluid

k Hydraulic conductivity of the interstitium

P_i Interstitial fluid pressure

v Interstitial fluid velocity

r Radial position

REV Representative elementary volume

R_n Radius of the necrotic core

ϵ Porosity or the volume fraction of fluid

$\mathbf{v}_f$ Fluid velocity averaged in the volume of fluid phase

ϕ_B Fluid source term or the rate of fluid flow per unit volume from blood vessels into the interstitial space

ϕ_L Lymphatic drainage term or the rate of fluid flow per unit volume from the interstitial space into lymph vessels

$\frac{J_V}{V}$ Volumetric flow rate out of the vasculature per unit volume of tissue

$\frac{S}{V}$ Surface area per unit volume of tissue for transport in the interstitium

L_p Hydraulic conductivity of the microvascular wall

P_B Vascular pressure

σ_s Average osmotic reflection coefficient for the plasma proteins

π_B Osmotic pressure of the plasma

π_i Osmotic pressure of the interstitial fluid

$\frac{J_L}{V}$ Volumetric flow rate into the lymphatics

L_{pL} Hydraulic conductivity of the lymphatic wall

P_L Hydrostatic pressure of the lymphatics

α Ratio of interstitial resistance to vascular resistance

P_{SS} Steady state pressure

P_e Effective pressure

IFV Interstitial fluid velocity

R^- Tumor tissue radius at the outer edge of the solid tumor

R^+ Normal tissue radius at the outer edge of the solid tumor

k_t Hydraulic conductivity of the interstitium in tumor tissue

k_n Hydraulic conductivity of the interstitium in normal tissue

$EB-FVM$ Element based finite volume method

FEM Finite element method

FVM Finite volume method

$SIMPLE$ Semi-implicit method for pressure linked equations

SOR Successive over-relaxation

DTI Diffusion tensor imaging

R_{nc} Critical necrotic radius

R Radius of spherical solid tumor

P_{sur} Surrounding pressure

Ω^- Tumor tissue at the outer edge of the solid tumor

Ω^+ Normal tissue at the outer edge of the solid tumor

L_p^{opt} Optimum value of hydraulic conductivity

λ (or a/b) Ratio of minor to major axes of both prolate and oblate spheroids

R_{eq} Radius of a spherical tumor with the same volume as both prolate and oblate tumors

ECM Extracellular matrix

$VEGF$ Vascular endothelial growth factor

$bFGF$ Basic fibroblast growth factor

EC Endothelial cell

MDE Matrix degrading enzyme

MMP Matrix metalloprotease

TAF Tumor angiogenic factor

n Endothelial cell density

D_n Random motility coefficient

c TAF concentration

τ Chemotactic function

τ_0 Chemotactic coefficient

κ Positive constant in chemotactic function

f Fibronectin concentration

m MDE concentration

ψ Haptotactic coefficient

R Matrix density function

D_c Diffusion coefficient of TAF

θ Decay rate of TAF

B Amount of TAF binds to the EC receptors

λ Uptake coefficient of TAF

ω Production coefficient of fibronectin

μ Uptake of fibronectin by ECs

D Nondimensional random motility coefficient

Z Nondimensional matrix density function

ρ Matrix density

ρ_0 Matrix density reference value

χ_0 Nondimensional chemotactic coefficient

δ Positive constant in nondimensional chemotactic function

ϕ Nondimensional haptotactic coefficient

η Nondimensional uptake coefficient of TAF

β Nondimensional production coefficient of fibronectin

γ Nondimensional uptake coefficient of fibronectin

ξ Normal outward unit vector

σ Constant in the matrix density function

ϵ_3 Constant in initial EC density distribution

α Production rate of MDE

ϵ Diffusion coefficient of MDE

ν Decay rate of MDE

ζ Decay rate of fibronectin due to MDE

P_0 Probability of EC to remain stationary

P_1 Probability of EC movement to left

P_2 Probability of EC movement to right

P_3 Probability of EC movement upward

P_4 Probability of EC movement downward

Q_c^k Net flow rate for each capillary

$Q_{B,c}^k$ Blood flow through each capillary

$Q_{t,c}^k$ Extravasation flux of fluid across the vascular or transvascular flow

ΔP Driving pressure

D Tube diameter

L Length

μ Blood viscosity

$\bar{P_B}$ Average blood pressure in vessels

$\bar{P_i}$ Average interstitial fluid pressure outside of the vascular element

V_i Interstitial fluid velocity

μ_{app} Apparent viscosity

H Hematocrit

μ_{rel} Relative apparent viscosity

μ_{45} Relative apparent blood viscosity for a fixed hematocrit of 0.45

C A factor that describes the shape of viscosity dependency on the hematocrit

ζ A phenomenological parameter that accounts for the strength of the non-symmetry of the hematocrit distribution at bifurcations

U_{cr} Critical ratio of the velocities of the branches

Δt Time step

S_{tot} Total stimuli

S_{wss} Wall shear stress stimuli

S_p Intravascular pressure stimuli

S_m Metabolic mechanism depending on the blood hematocrit stimuli

τ_w Actual wall shear stress in a vessel segment

τ_{ref} A small constant included to avoid singular behavior at low wall shear stress rates

$\tau_e(P_B)$ Wall shear stress resulting from the blood pressure

Q_{ref} The largest value of Q_B in the network

k_p Sensitivity of the adaptive response of vessel diameter to changes in intravascular pressure

k_m Sensitivity of the adaptive response of vessel diameter to changes in metabolic state

k_s Shrinking tendency

q Number of iterations

Chapter 1

Introduction

Although heart and blood vessel diseases were the main causes of death for many years, more than 12 million new cancer diagnoses were reported in 2011, making it the new leading cause of death. At least 30% of people develop cancer, and 25% of men's and 20% of women's deaths are due to it. More than 85% of cancers involve solid tumors [43]. Since cancer arises from disturbances in cell proliferation, differentiation, and development, understanding each of these mechanisms that may lead to tumor formation is very important in finding more effective therapies. Because of its complexity in formation, development, and cure, cancer is known as one of the main medical challenges worldwide. This challenge is more highlighted in mathematical modeling of tumor development and related blood flow and transport.

Modeling interstitial fluid flow involves processes such as fluid diffusion, convective transport in extracellular matrices, and extravasation from blood vessels. In all of these processes, computational fluid dynamics (CFD) can play a crucial role in elucidating the mechanisms of fluid flow in solid tumors and surrounding tissues. The research conducted for this dissertation concentrates on developing mathematical models of drug delivery to solid tumors, including a discrete model of angiogenesis used to create a capillary network model of microvasculature. This network is then used in a fluid flow model to couple intravascular and extravascular flow. This fluid flow model captures key features that occur in both tissue and microvasculature. Using this model, the important factors in both angiogenesis and drug delivery are investigated. This dissertation is organized in the following manner.

Chapter 2 provides a general model of interstitial fluid flow in both cancerous and normal tissues. Instead of representing a discrete and heterogeneous vasculature, a continuous

and homogenized source term is considered throughout the tissue. This chapter provides a background to the biological and physiological characteristics of cancerous tissues and highlights the complexity of transport phenomena in a solid tumor, even for a more specific geometry (spherical shape) and uniform distribution of microvessels. Also included is a discussion of the importance of two new parameters introduced in this dissertation. Certain key features of those two new parameters conclude the chapter. Results presented in Chapter 2 have already been published in *PLoS ONE* [92].

Chapter 3 presents of an overview of tumor shape and size effects on drug delivery to solid tumors. These effects are established by application of the governing equations for fluid flow, i.e., the conservation laws for mass and momentum, to physiological systems containing solid tumors, under an assumption that drug particles flow with the interstitial fluid. Drug delivery problems have been most extensively researched in spherical tumors, which have been the simplest to examine with analytical methods. With our numerical method introduced in Chapters 2 and 3, however, more complex tumor shapes can be studied. The numerical model of fluid flow in solid tumors previously introduced by our group is further developed to incorporate and investigate non-spherical tumors such as prolate and oblate ones. The chapter also explores the effects of the surface area per unit volume of the tissue, vascular and interstitial hydraulic conductivity on drug delivery. Results presented in Chapter 3 have already been published in the *Journal of Biological Engineering* [93].

Cancer invasion and metastasis rely on tumor-induced angiogenesis, the formation of new blood vessels from existing vasculature in response to tumor angiogenic factors. Angiogenesis is a complicated phenomenon including even more complex interactions such as cell-cell and cell-matrix communication. The details of processes required for angiogenesis to occur and also details of modifications of some features of the previously presented continuous and discrete models of angiogenesis are discussed in Chapter 4. These modifications are on the initial distribution of fibronectin and tumor angiogenic factor (TAF) in the domain and also in the interpretation of the effect of matrix degrading enzyme (MDE) in the continuous and discrete model. One of the main advantages of this study is the realistic movement probability distribution achieved. Capillaries should accelerate as they move toward the tumor, a phenomenon not reflected in previous modeling. Here, changing the function of the chemotactic coefficient and also real initial conditions leads to more realistic movement probability distribution in the domain; thus, capillaries demonstrate an increased probability to move toward the tumor as they approach a tumor. Fibronectin degradation is clearly shown to establish haptotactic movement, and in the absence of MDE, the expected haptotactic movement decreases. Results presented in Chapter 4 have already been submitted to a scientific journal.

To date, microvasculature flow modeling has been most extensively studied with simple tumor shapes and their microvessels at different levels and scales. However, with our numerical model proposed in Chapter 5, more complex and realistic tumor shapes and capillary networks can be studied. This chapter formulates a fluid flow model of blood in a capillary network model of a solid tumor and its surrounding tissue. First, governing equations of angiogenesis are implemented to specify the different domains for the network and interstitium. Once the initial and boundary conditions are set, the discretized form of the governing equations for the capillary network can be solved. Then, fluid flow equations are introduced for different domains. A comprehensive continuum mathematical model of interstitial fluid flow in a solid tumor has already been developed for physiological systems containing solid tumors in Chapters 2 and 3. As introduced in these chapters, this model is based on the governing equations for fluid flow, i.e., the conservation laws for mass and momentum, and Darcy's equation. The equations governing blood flow through capillaries are the Navier-Stokes equations that are simplified to the Poiseuille equation for this study. Starling's law closes this system of equations and couples the intravascular and extravascular flows. Using an element-based finite volume numerical method, the discretized form of the governing equations, with appropriate boundary conditions, has been developed to calculate the interstitial fluid and intravascular pressures.

Also in Chapter 5, in order to show the effect of individual vessels in normal and cancerous tissues instead of having a uniform and continuous distribution of microvessels such as those used in Chapters 2 and 3, a capillary network model introduced in Chapter 4 is considered because it gives a more realistic distribution of microvessels, one very close to that in the human body. After setting up the capillary network, a mass conservation equation must be applied at each node for intravascular flow, as in any other network flow model. This is the first study to naturalistically couple intravascular and extravascular flow through a loop made of a parent vessel connected to the network. That is, the same vessel runs to and from the network and engages in that network, in contrast to the situations portrayed in other studies that unrealistically consider veins and arteries to operate on opposite sides of a tumor network. For intravascular flow, this study considers the effect of viscosity dependency on hematocrit and vessel diameter. Vessel adaptation and phase separation are also considered in this work for intravascular flow. All of these assumptions are added to previous models in the hope of more realistic results. Results presented in Chapter 5 have already been submitted to a scientific journal.

1.1 Objectives

Numerical simulation provides a good understanding of the mechanism of drug delivery and is also very instructive to show some of the major barriers in this process of drug delivery to solid tumors. For instance, one can find an optimum schedule of treatments based on the different values of simulation parameters. To design an optimum mechanism for drug delivery, the transport mechanisms and their obstacles have to be clarified, which was one of the main objectives of this research.

The main goal of this study was to simulate drug delivery to solid tumor microvasculature. To cover the following parts missing from the literature, the specific objectives of this study were as follows:

- Study the effect of the size, shape and physical properties of solid tumors,
- Improve the previous model to include nanoparticle drug delivery,
- Include the heterogeneity and discontinuous form of blood vessels in the model,
- Solve the governing equations simultaneously as a multi-scale problem,
- Study the capillary network model of tumor-induced angiogenesis for both continuous and discrete models,
- Study fluid flow models for different models of microvessels such as uniform, non-uniform, and network-based, and finally,
- Couple the fluid flow in tissues and blood flow in microvasculature for different networks.

Chapter 2

Numerical Modeling of Fluid Flow in Solid Tumors

2.1 Introduction

Cancer is the second leading cause of death, today causing one of every four deaths in North America [43]. Although the most important treatment is surgical removal of tumors, the key to a successful cure is often an efficient delivery of anticancer drugs after the surgery. Many new drugs have been developed to eradicate cancer but are ineffective when used in humans for lack of efficient delivery. Moreover, all drugs have possible side effects, such as toxicity to normal cells and the development of drug resistance [49]. Residual tumor cells and re-growth of tumors are common sequels to the use of most of these drugs. The drugs' most noticeable limitation is their inability to reach a targeted area without affecting healthy tissues or cells. The two considerations in effective cancer treatment, from an engineering point of view, are drug transport and drug conversion or reaction at the tumor site [7, 45]. Many drugs cannot be delivered to their targets because of transport limitations. Other drugs induce biochemical reactions in the body that produce toxicity.

It is known that more than 85% of human cancers involve solid tumors, and current chemotherapy depends on the adequate delivery of therapeutic agents to tumor sites [43]. It is also well recognized that the blood supply to a solid tumor is highly heterogeneous [46, 40]. Although small drugs such as taxol distribute pretty well in tumor tissue as they can diffuse and do not rely on convection, larger drugs behave differently. In fact, for large particles such as antibodies, drug concentration is highest closest to vasculature, well-perfused areas, and on the peripheral walls of the tumor, but very low or no drug

reaches 90% of the tumor [51, 87]. However, for successful cancer treatment, all areas of the tumor must be exposed to chemotherapy agents; otherwise, the tumor will eventually regrow [34].

According to clinical research findings, even though drug delivery through systemic administration may inhibit tumor growth, most drug treatments fail to eliminate malignant tumors completely [12]. Some experimental and computational investigations show that systemic administration cannot distribute drugs uniformly in tumors. Baxter *et al.* have shown that, in addition to blood flow heterogeneities and impeded interstitial transport, another mechanism effectively contributes to the non-uniform distribution of drugs: high interstitial pressure in solid tumors [38, 39, 44]. There are two important effects of this high interstitial pressure, and both limit transport in solid tumors. These two effects are illustrated schematically in Figure 2.1. The first is a decrease in driving force for transcapillary exchange of fluid and therefore drugs. This effect is highlighted in Figure 2.1. Low filtration occurs at the center of the tumor as a result of the high interstitial pressure, and high filtration occurs at the periphery of the tumor as a result of the low interstitial pressure. The second effect is a radially outward convective flux in the interstitium as fluid flows towards the outer layers of the tumor. This effect is illustrated in Figure 2.1 as an outward convection due to pressure gradient. The value of the radially outward fluid velocity at the tumor rim for a tumor with a $1cm$ radius, $4.2g$, is $0.1 \sim 0.2\mu m/s$ [7]. Another important process in drug delivery is indicated in this schematic as an inward diffusion due to concentration gradient of the drug. Effective penetration into a solid tumor requires that the velocity of the diffusion process be higher than that of the convection process [41]. On the other hand, uniformly distributed high interstitial pressure in the center of a tumor blocks convection and, consequently, causes the heterogeneous perfusion of blood into the center of tumors, resulting in the heterogeneous distribution of the drug [44]. The existence of pressure gradients in tumors was discovered by Baxter *et al.* and confirmed by Boucher *et al.* [13]. Baxter and Jain, using their theoretical framework, further found that the drug diffusivity, pressure and velocity of interstitial fluids, vascular permeability and lymphatic drainage are important factors in determining the drug concentration in tumors [7, 8, 9]. Netti *et al.* showed that interstitial fluid pressure (IFP) depends on microvascular pressure and blood flow within tumors [67].

Extending the one-dimensional models of Baxter and Jain [7, 8, 9] and Saltzman and Radomsky [85] to a three-dimensional geometry, Wang et al. [103, 99, 33, 101, 100, 104] developed a simulation framework of drug delivery to tumors. They considered high interstitial pressure in tumors [44], the consequences of blood and lymphatic drainage, and the chemical reaction of drug with the tissue. The main focus of their work was on using diffusion-convection kinetics to improve simulation result accuracy. They showed that the

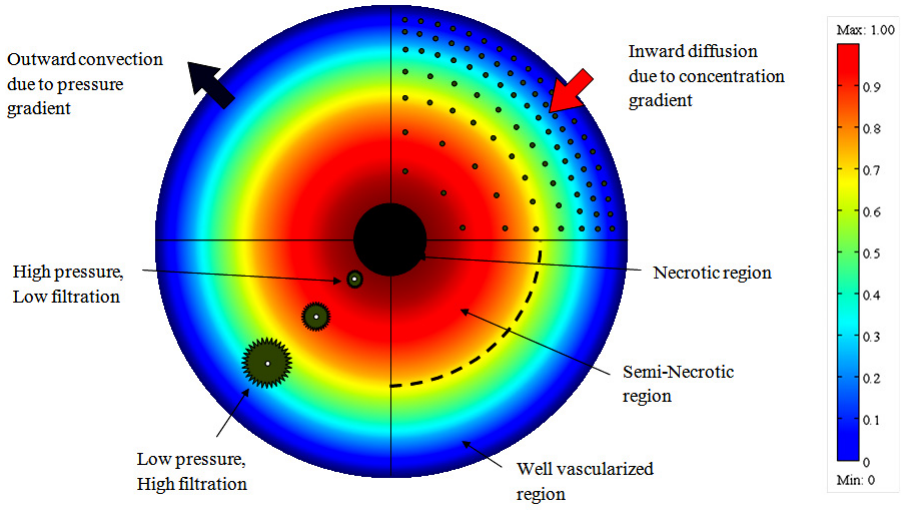

Figure 2.1: Cross sectional schematic of a solid tumor that shows the three different regions of a solid tumor, IFP distribution, drug concentration and filtration distribution from blood vessels.

in vitro release profile of the drug from controlled release devices can be combined with state-of-the-art computational fluid dynamics (CFD) simulations to predict drug delivery behavior, both temporally and spatially, in both normal and cancerous tissues. The focus of their work was the mathematical modeling of the drug release from polymer implants that have certain characteristics of release profile. By applying sensitivity analysis, Zhao *et al.* [115] determined the effect of spatially changing tissue transport properties on interstitial fluid (including drug particles) transport.

Knowledge of tumor modeling has recently been expanded to include spatial and temporal changes in blood flow by considering capillary network or single vessel approaches [75, 19]. Before Baxter *et al.* [7, 8, 9] introduced their innovative model of interstitial pressure as a function of tumor radius, little was known about tumor modeling, except that interstitial pressure was highest at the center of a tumor [105] and that pressure is directly proportional to tumor size [111, 105]. The promising combined therapies such as radiotherapy and antiangiogenic therapy in addition to chemotherapy in tumor treatment are good examples that can show the crucial role of the modeling. For example, computational fluid dynamics modeling results can be applied to optimize the interaction effect of irradiation to the drug delivery efficiency.

The main focus of future drug delivery modeling will be on drug transport in tissues

after drug release using either systemic administration or implantation mechanisms. Modeling drug delivery involves different processes such as drug diffusion, convective transport in extracellular matrices, drug extravasation from blood vessels, tissue elimination by the lymphatic system, and intracellular internalization. In all of these processes, CFD can play a crucial role. To clarify the mechanisms of drug delivery from the injection site to absorption by a solid tumor, computational fluid dynamics has shown promise. So far, drug delivery problems have been most extensively studied with spherical tumors, the simplest to examine with analytical methods. With our proposed numerical method, however, more complex shapes of tumor can be studied. Numerical simulations provide a detailed understanding of the mechanisms of interstitial fluid transport and are also instructive to show some of the major barriers to drug delivery to solid tumors. With this knowledge, one can find, for example, an optimum schedule of drug treatment based on the simulation results. To design an optimum scheme for drug delivery, the transport mechanisms and their obstacles have to be clarified, which is one of the main objectives of this study.

The proposed CFD model is made for a spherical tumor and its surrounding normal tissue. However, this model can be extended to study non-spherical tumors, especially if its geometries are reconstructed from high-resolution images. Grid generation divides the whole domain or geometry into finite volumes, called meshes. Tetrahedral elements can be used to handle non-spherical tumors. The tumor and its surrounding tissue are assumed to be rigid porous media. The vasculature as a source term varies spatially. Interstitial fluid flow equations in porous media are solved using a CFD code that employs unstructured grids. In studying interstitial fluid pressure distribution, the numerical method, which introduces two critical parameters (tumor radius and necrotic radius), is more effective than the analytical method.

2.2 Drug Transport within Solid Tumors

Fluid seeps slowly but constantly from blood vessels into surrounding tissues in most normal tissues. The lymphatic system then reabsorbs this lost fluid and returns it to the blood stream. However, no such lymphatic drainage system for solid tumors has been reported in the literature [7, 45]. Computer simulations show that this lack of lymphatic system involvement may result in a buildup of interstitial pressure, leading to cessation of the usual blood seepage from vessels. As a consequence, large molecules (including cancer-fighting drugs) cannot be carried out of vessels to interact with tissue. Thus, cancer drugs cannot reach the tumor site.

Some drug particles, such as Monoclonal Antibodies (MAbs), are relatively large and

move very slowly within tissues [7]. To be effective, these large anticancer agents have to cross the blood vessel wall, traverse the interstitial space that contains the cancer cells, bind to the cancer cell membranes and, if the target is intracellular, penetrate the cancer cell membranes.

Tissue spaces are made up of three parts, all of which are relevant to the delivery of drugs to tumors: the vascular, the interstitial, and the cellular. The vascular space comprises the blood vessels, arteries, arterioles, capillaries, venules, and veins [16]. The interstitial space, a gel-like region between blood vessels and cells, is filled with fibers such as collagen, and gives structural stability, glycosaminoglycans (GAG), and other proteins. The cellular space includes specific tissue cells (cancer cells in a solid tumor), in addition to other cells, such as pericytes, macrophages, and fibroblasts [7, 8, 9].

2.3 Mathematical Model of Interstitial Fluid Transport

The distribution of vasculature and cells in solid tumors is spatially heterogeneous. In the center of solid tumors, there is a necrotic core where most of the cells are dead. The outer boundary of solid tumors contains many exchange vessels, a large blood supply, and fast-dividing cells. Therefore, the mathematical model should be accurate enough to include the dependency of physiological parameters, such as hydraulic conductivity, on space; that is, it must be able to clearly represent all the physical variations in a tumor. Nevertheless, because the time scale of transport phenomena is much less than that of tumor growth, the physiological parameters can be considered time independent [7]. For the sake of simplicity, solid tumors are considered here to be spherical. In a macroscopic model, only the distribution of variables, such as interstitial pressure and concentration, over the length scale of the tumor radius is important, and microscopic characteristics, such as blood vessels, cells, and the interstitial matrix, are not involved directly in the model. Comparison of the tumor radius, on the order of magnitude of $1cm$, $O(1cm)$, with the intercapillary distance (the average distance between two capillaries), $O(100\mu m)$, indicates that variations over microscopic length scales can be averaged out [84]. The screening length, $\sqrt{\mu k}$ (in which μ and k are the viscosity of the interstitial fluid and the hydraulic conductivity of the interstitium, respectively), is on the order of $60\mathring{A}$; therefore, the fluid transport in the tumor interstitium can be described by Darcy's law for flow through a porous medium [84, 45, 88, 35, 25, 10]:

$$\begin{array}{ll} \mathbf{v} = -k\nabla P_i & \text{in general} \\ v = -k\dfrac{\partial P_i}{\partial r} & \text{for axisymmetric flow} \end{array} \tag{2.1}$$

where $k[cm^2/mmHg\ \ s]$, $P_i[mmHg]$, $v[m/s]$ and $r[cm]$ are the hydraulic conductivity of the interstitium, the interstitial fluid pressure, the interstitial fluid velocity and the radial position, respectively. In the case of anisotropic and heterogeneous porous media, k is a tensor and function of the location in the medium. There are some limitations to the use of Darcy's law. For instance, it is not applicable for non-Newtonian fluids, Newtonian fluids at high velocities, or for gases at very low or very high velocities. It is also shown that the friction within the fluid and exchange of momentum between the fluid and solid phases are neglected by Darcy's law. Fortunately, in the interstitium of biological tissues, all these exceptional cases are rare (most of the phenomena are low velocity for Newtonian fluids) except for the friction within the fluid; therefore, Darcy's law is quite applicable to the analysis of interstitial fluid flow.

The mass balance equation for a steady state incompressible fluid is that the divergence of the fluid is zero, or mathematically,

$$\nabla \cdot \mathbf{v} = 0 \tag{2.2}$$

The same equation is also applicable in porous media if there is no fluid source or fluid sink in the medium. However, in most biological tissues, sources and sinks are present. For instance, between interstitial space and the blood or lymph vessels, fluid is exchanged; therefore, the steady state incompressible form of the continuity equation must be modified as

$$\nabla \cdot \mathbf{v} = \phi_B(r) - \phi_L(r) \tag{2.3}$$

where $\mathbf{v}$ is the fluid velocity in the representative elementary volume (REV). The continuity equation can also be written as

$$\nabla \cdot (\epsilon \mathbf{v}_f) = \begin{cases} \phi_B(r) - \phi_L(r) & \text{for } r \geq R_n \\ 0 & \text{for } r < R_n \end{cases} \tag{2.4}$$

where $R_n[cm]$, ϵ, $\mathbf{v}_f[ms^{-1}]$, $\phi_B(r)[s^{-1}]$, and $\phi_L(r)[s^{-1}]$ are the radius of the necrotic core, the porosity or the volume fraction of fluid, the fluid velocity averaged in the volume of fluid phase, the fluid source term, and the lymphatic drainage term, respectively. In biological

tissues, the two last terms signify the rate of fluid flow per unit volume from blood vessels into the interstitial space and from the interstitial space into lymph vessels, respectively. Both rates can be evaluated through Starling's law. It should be noted that Equation 2.4 in this general form is applicable to any kind of biological tissue, whether normal or cancerous. In dead tissues, with no flow in the blood or lymph vessels, the value for both terms is zero. The fluid source term is governed by Starling's law as follows [94, 23]:

$$\phi_B(r) = \frac{J_V}{V} = \frac{L_P S}{V}(P_B - P_i - \sigma_s(\pi_B - \pi_i)) \tag{2.5}$$

The parameters used in Equation 2.5 are: $\frac{J_V}{V}[s^{-1}]$, volumetric flow rate out of the vasculature per unit volume of tissue; $\frac{S}{V}[cm^{-1}]$, surface area per unit volume for transport in the tumor; $L_p[\frac{cm}{mmHg\ s}]$, hydraulic conductivity of the microvascular wall; $P_B[mmHg]$, vascular pressure; σ_s, average osmotic reflection coefficient for plasma proteins; $\pi_B[mmHg]$, osmotic pressure of the plasma; and $\pi_i[mmHg]$, osmotic pressure of the interstitial fluid. Different types of pressure used in Equation 2.5 are shown in Figure 2.2. It should be noted that the lymphatic drainage term is proportional to the pressure difference between the interstitium and the lymphatics:

$$\begin{aligned} \phi_L(r) &= \frac{J_L}{V} = \frac{L_{PL} S_L}{V}(P_i - P_L) \qquad \text{for } r \geq R_n \\ \phi_B(r) &= \phi_L(r) = 0 \qquad\qquad\qquad\quad \text{for } r < R_n \end{aligned} \tag{2.6}$$

The parameters used in these equations are: $\frac{J_L}{V}[s^{-1}]$, volumetric flow rate into the lymphatics; $L_{pL}[\frac{cm}{mmHg\ s}]$, hydraulic conductivity of the lymphatic wall; and $P_L[mmHg]$, hydrostatic pressure of the lymphatics.

Combination of Darcy's law and the continuity equation results in

$$-\nabla \cdot k \nabla P_i = \phi_B(r) - \phi_L(r) \tag{2.7}$$

For a very special case, when k is constant and there are no sinks and sources (for example, in the necrotic core), the interstitial pressure can be expressed by the very well-known Laplace equation.

$$\nabla^2 P_i = 0 \tag{2.8}$$

If all parameters except P_i are assumed to be constant, substituting Equations 2.5 and 2.6 in Equation 2.7 results in

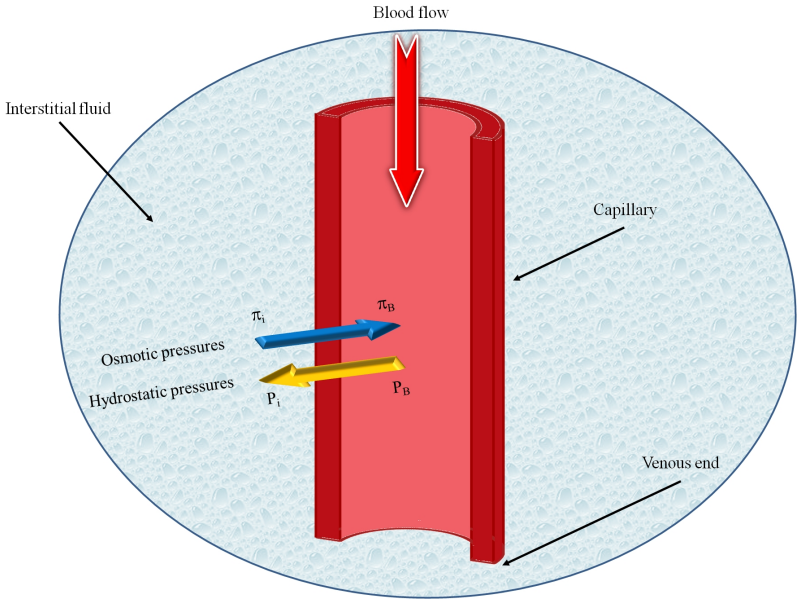

Figure 2.2: Capillary microcirculation schematic and different types of pressure

$$-k\nabla^2 P_i = \frac{L_P S}{V}(P_B - P_i - \sigma_s(\pi_B - \pi_i)) - \frac{L_{PL} S_L}{V}(P_i - P_L) \tag{2.9}$$

Rearranging Equation 2.9 for a spherical solid tumor with radius R,

$$\nabla^2 P_i = \frac{\alpha^2}{R^2}(P_i - P_{ss}) \tag{2.10}$$

P_{SS} is defined later by Equation 2.14. Using the definition of the Laplace operator, Equation 2.11, in the spherical coordinate system, Equation 2.10 is written as Equation 2.12.

$$\Delta = \nabla^2 = \frac{1}{r^2}\frac{\partial}{\partial r}\left(r^2\frac{\partial}{\partial r}\right) + \frac{1}{r^2\sin\theta}\frac{\partial}{\partial\theta}\left(\sin\theta\frac{\partial}{\partial\theta}\right) + \frac{1}{r^2\sin^2\theta}\frac{\partial^2}{\partial^2\phi} \tag{2.11}$$

$$\frac{1}{r^2}\frac{\partial}{\partial r}\left(r^2\frac{\partial P_i}{\partial r}\right) = \frac{\alpha^2}{R^2}(P_i - P_{ss}) \tag{2.12}$$

in Equations 2.10 and 2.12, the ratio of interstitial resistance to vascular resistance is introduced in terms of α, the dimensionless parameter defined by Equation (2.13).

$$\alpha = R\sqrt{(L_P S + L_{PL} S_L)/kV} \tag{2.13}$$

$$P_{SS} = (L_P S P_e + L_{PL} S_L P_L)/(L_P S + L_{PL} S_L) \tag{2.14}$$

The steady state pressure, P_{SS}, is the interstitial pressure at which the efflux from the vasculature and influx into the lymphatics are equal, and is defined by Equation 2.14. Effective pressure, P_e, in Equation 2.14, is a parameter defined by vascular pressure, plasma osmotic pressure, and interstitial osmotic pressure through Equation 2.15.

$$P_e = P_B - \sigma_s(\pi_B - \pi_i) \tag{2.15}$$

Applying the appropriate boundary conditions and also all the constants mentioned earlier, the governing equation, Equation 2.10 or 2.12, can be used to calculate the interstitial fluid velocity (IFV) and interstitial fluid pressure (IFP) profiles in solid tumors. No lymph vessels in a solid tumor means $S_L = 0$; thus, Equations 2.12 and 2.13 can be simplified as follows:

$$\frac{1}{r^2}\frac{\partial}{\partial r}\left(r^2\frac{\partial P_i}{\partial r}\right) = \frac{\alpha^2}{R^2}(P_i - P_e) \tag{2.16}$$

$$\alpha = R\sqrt{(L_P S)/kV} \tag{2.17}$$

in which the interstitial pressure that yields zero net volume flux out of the vasculature is called the effective pressure, P_e, Equation 2.15. The steady state pressure and effective pressure in solid tumors with no lymph vessels are the same. If $P_i = P_e$, no exchange of fluid occurs between the interstitial space and blood vessels.

Due to symmetry, there is a no flux boundary condition at the center of the tumor; i.e.,

$$\nabla P_i = 0 \quad \text{or} \quad \frac{\partial P_i}{\partial r} = 0 \qquad \text{for } r = 0 \tag{2.18}$$

At the outer edge of the solid tumor, $r = R$, two types of boundary conditions are possible. In the first type, where the pressure in the surrounding tissue is fixed, the tumor pressure at the outer edge is the same as the surrounding pressure, P_{sur}.

$$P_i = P_{sur} \qquad \text{for } r = R \tag{2.19}$$

This condition is applicable for an isolated tumor [36, 14]. In the second type, the solid tumor is surrounded by normal tissues. Pressure decreases smoothly over a distance; therefore, the continuity of pressure and velocity should be considered as an appropriate boundary condition for this case as the following conditions occur simultaneously:

$$-k_t \frac{dP_i}{dr}\bigg|_{R^-} = -k_n \frac{dP_i}{dr}\bigg|_{R^+} \tag{2.20}$$

$$P_i|_{R^-} = P_i|_{R^+} \tag{2.21}$$

where R^- and R^+ indicate the tumor and normal tissue radius at the outer edge of the solid tumor; k_t and k_n are the hydraulic conductivity of the interstitium in tumor and normal tissues, respectively. It should be noted that, in the second type, all the equations mentioned for the tumor tissue have to be solved for the normal tissue, as well. It is clear that for the normal tissue, far enough from the solid tumor that the pressure is constant, the first type of boundary condition, Equation 2.19, must be applied. These two types of boundary conditions are shown in Figure 2.3. The solution now can be obtained analytically or numerically to find the IFV and IFP profiles for each of the two boundary conditions. Analytical solutions, based on Baxter et al. [7] and Jain et al. [45], for both IFV and IFP distributions in case of an isolated solid tumor are shown in Figure 2.4 and Figure 2.5, respectively. In this work, the numerical method has been used. An element based finite volume method (EB-FVM) is applied to discretize the equations. The EB-FVM has the capability of the finite element method (FEM) in handling complex geometries and also the sound physical-based properties of the finite volume method (FVM) [91]. The discretized form of the governing equations, in their general form, is then linearized and solved implicitly. The SIMPLE (Semi Implicit Method for Pressure Linked Equations) algorithm is used as the coupling method for pressure and velocity terms. Finally, the converged form of the solution is calculated using an iterative method. In order to improve the convergence rate, the method of successive over-relaxation (SOR) is applied with an under relaxation factor equal to 0.75. The criterion for the convergence is to reduce the residual by 6 orders of magnitude. In order to check the grid independency of the code, the results for three different grids are compared, indicating the conservative property of the numerical method. Final choice of the grid includes 11904 control volumes.

The material properties for tumor and normal tissue were taken from the simulation studies of Jain and Baxter [44] and are shown in Table 2.1. It should be noted that tissue

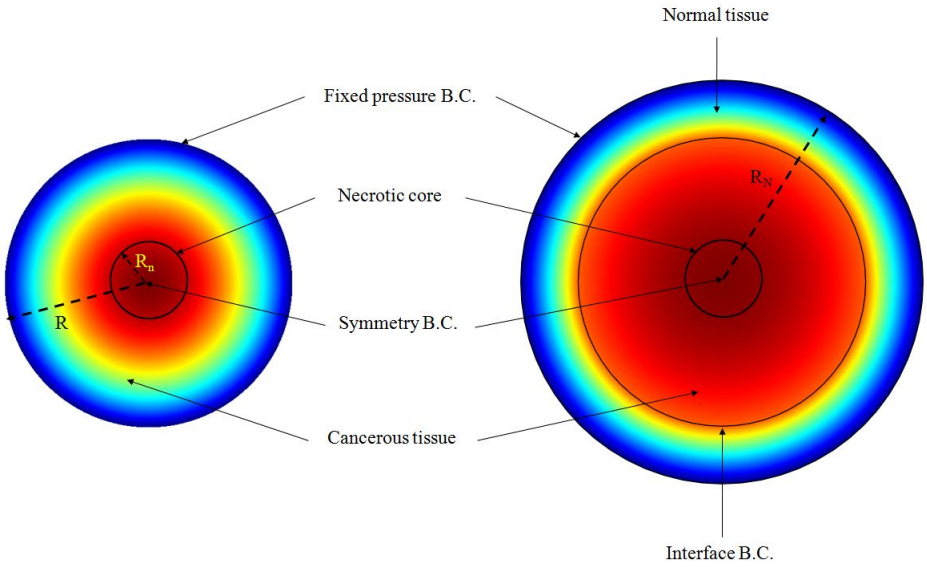

Figure 2.3: Two types of boundary conditions at the outer edge of the tissue

properties vary greatly among different organs for both normal and cancerous tissues; therefore, the parameters introduced in Table 2.1 should be updated for new applications. As mentioned earlier, tissue transport properties are often anisotropic. Geometric and physiological properties of anisotropic and heterogeneous tissues affect drug delivery. This issue can be solved with the help of diffusion tensor imaging (DTI). A good application of this method in brain tumors is discussed by Linninger *et al.* [59].

2.4 Results

Figure 2.6 shows the unidirectional interstitial fluid velocity distribution in an isolated solid tumor as a function of the dimensionless radius. This figure shows that the higher the value of α is, the steeper the velocity profiles will be.

Figure 2.7 shows the unidirectional interstitial fluid pressure distribution in an isolated solid tumor as a function of the dimensionless radius. Low values of α corresponding to flat curves show less resistance to fluid source, but high values of α corresponding to sharp

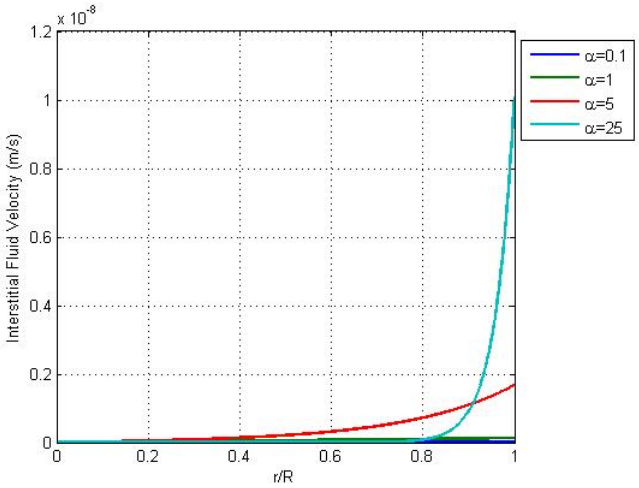

Figure 2.4: Interstitial velocity distribution in a 1 cm radius tumor, different values of α, Baxter et al. [7] and Jain et al. [45]

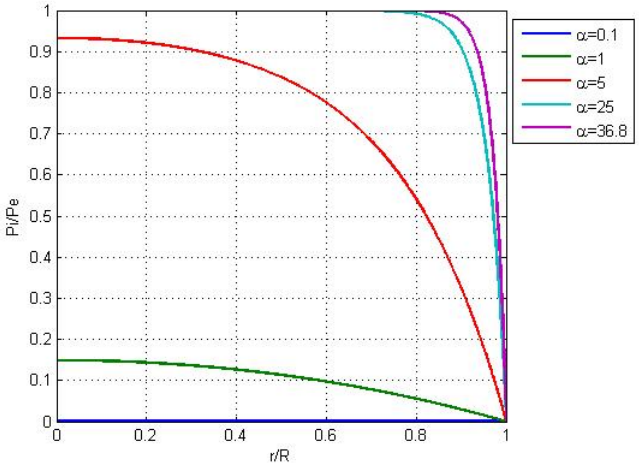

Figure 2.5: Dimensionless interstitial pressure distribution in the same tumor, different values of α, Baxter et al. [7] and Jain et al. [45]

Table 2.1: Material properties used in numerical simulations, as taken from [44]

Parameter	Tissue	Baseline value	Reference
$L_p[cm/mmHg\ \ s]$	Normal	0.36×10^{-7}	Rippe *et al.* (1978)
	Tumor	2.80×10^{-7}	Jain (1987a)
$k[cm^2/mmHg\ \ s]$	Normal	8.53×10^{-9}	Swabb *et al.* (1974)
	Tumor	4.13×10^{-8}	Jain (1987a)
$S/V[cm^{-1}]$	Normal	70	Pappenheimer *et al.* (1951)
	Tumor	200	Hilmas and Gilette (1974)
$P_B[mmHg]$	Both	15.6	Brace and Guyton (1977)
$\pi_B[mmHg]$	Both	20	Brace and Guyton (1977)
$\pi_i[mmHg]$	Normal	10	Wiederhielm (1979)
	Tumor	15	Jain (1987a)
σ_s	Normal	0.91	Ballard and perl (1978)
	Tumor	0.82	Curry (1984)

curves in the periphery of the tumor show greater resistance to fluid source, based on the definition of dimensionless parameter α.

Figure 2.8 shows IFP distribution based on the parameters' values introduced in Table 2.1, which results in $\alpha = 36.8$. Experiments done by Baxter *et al.* were based on this value of α [7].

A three-dimensional plot of Figure 2.8, dimensionless interstitial pressure distribution, is shown in Figure 2.9. All of these results agree well with experimental data [7, 38, 45].

Figure 2.10 shows the comparison of the current paper with experimental data (mammary adenocarcinoma s.c.) by Boucher *et al.* [13]. In this figure there is good agreement between model and experiment. Figures 2.11 and 2.12 show the IFV and IFP distribution for a solid tumor embedded in normal tissue as a function of the dimensionless radius, respectively. As mentioned earlier, boundary conditions for this case are different from those of an isolated tumor and are stated in Equations 2.20 and 2.21.

Figure 2.13 shows the interstitial pressure distribution in a $1cm$ radius tumor, as a function of a dimensionless radius for different values of necrotic radii. This figure shows that an increase in the necrotic radius decreases the maximum pressure inside the tumor, and obviously, when the entire tumor is necrotic, with no vasculature, the IFP is zero. On the other hand, for a necrotic radius below a certain size, IFP approaches to its maximum value, which is the effective pressure, P_e, and this limited size, which can be considered as a critical necrotic radius or R_{nc}, can be interpolated from a graph such as Figure 2.14.

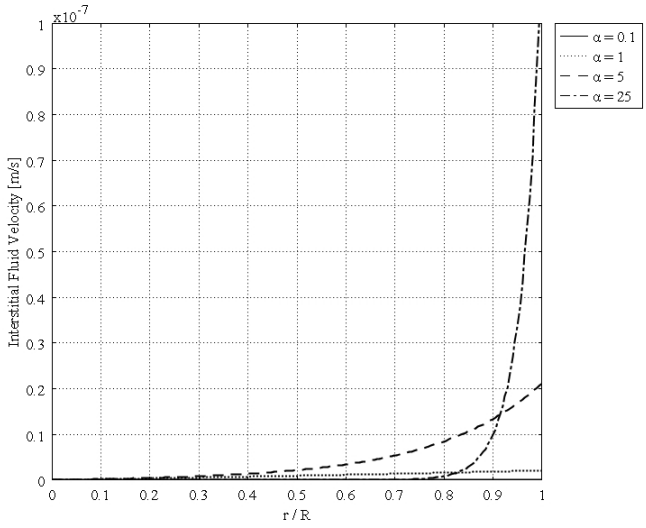

Figure 2.6: Interstitial velocity distribution in a 1 cm radius tumor, different values of α, Equation 2.16

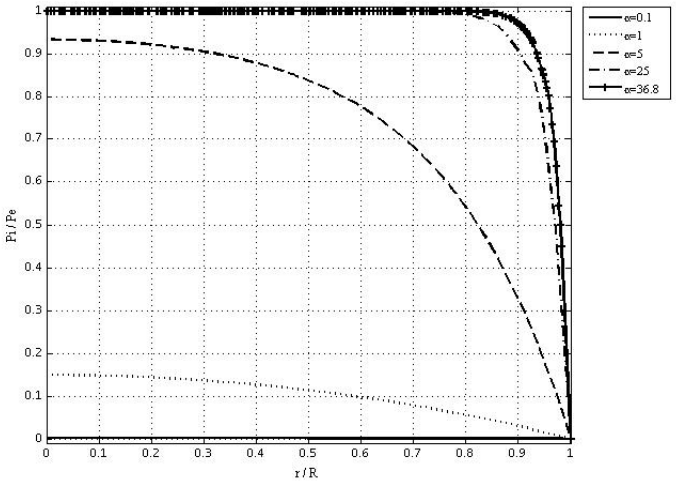

Figure 2.7: Dimensionless interstitial pressure distribution in the same tumor, different values of α

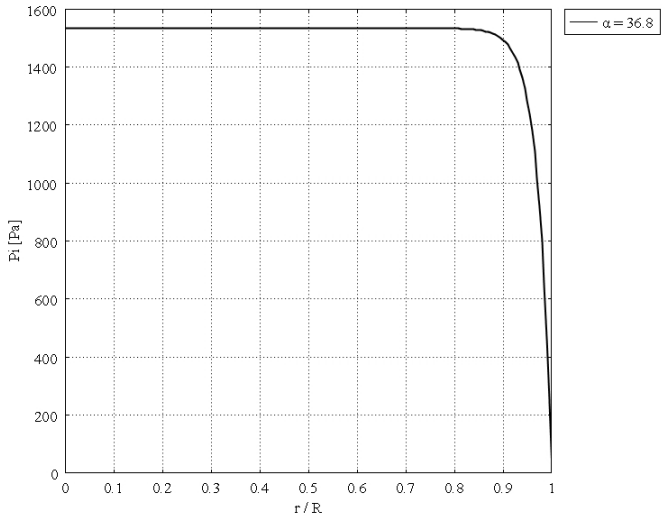

Figure 2.8: Interstitial pressure distribution in the same tumor ($\alpha = 36.8$)

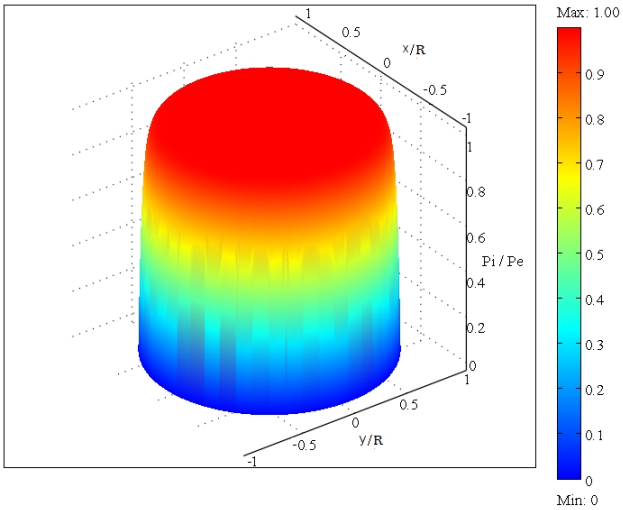

Figure 2.9: Three dimensional plot of Figure 2.8, dimensionless interstitial pressure distribution, in the same tumor ($\alpha = 36.8$)

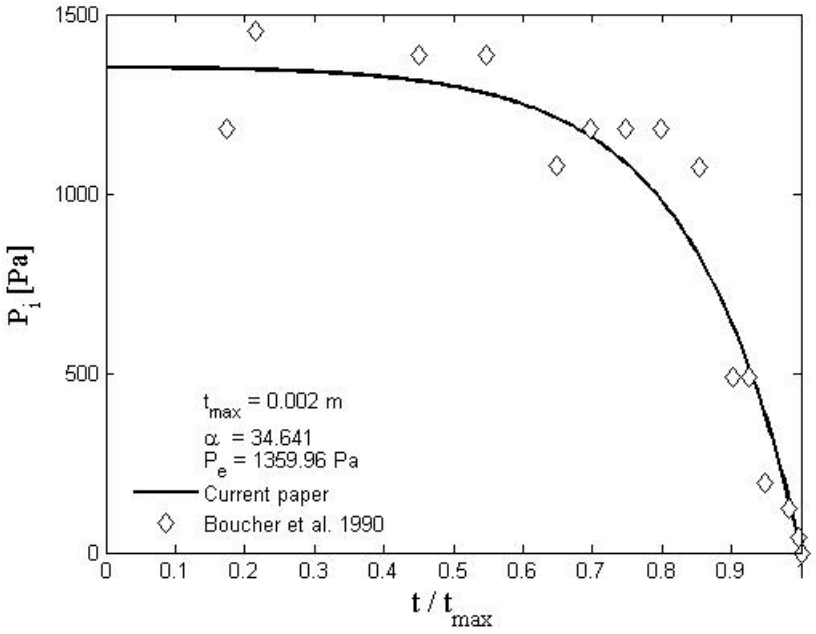

Figure 2.10: Comparison of the current study with experimental data (Mammary Adenocarcinoma s.c.) by Boucher *et al.* [13]

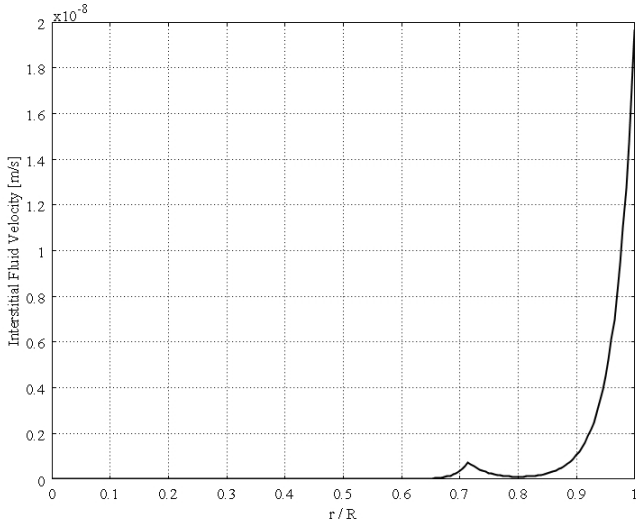

Figure 2.11: Interstitial velocity distribution in a 1.4cm radius tumor and normal tissue

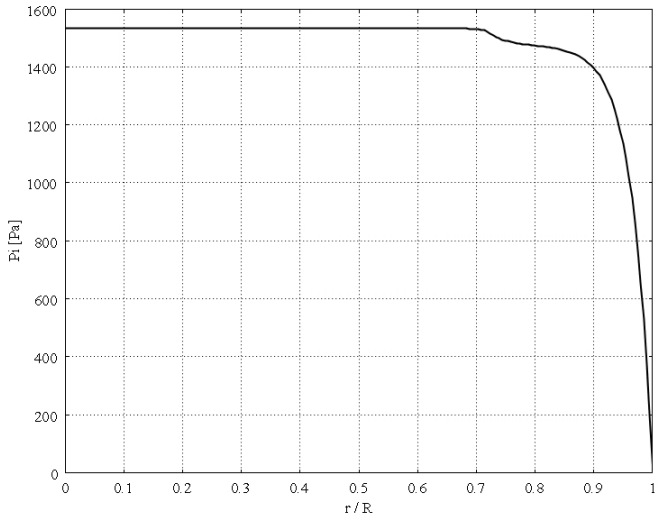

Figure 2.12: Interstitial pressure distribution in a 1.4cm radius tumor and normal tissue

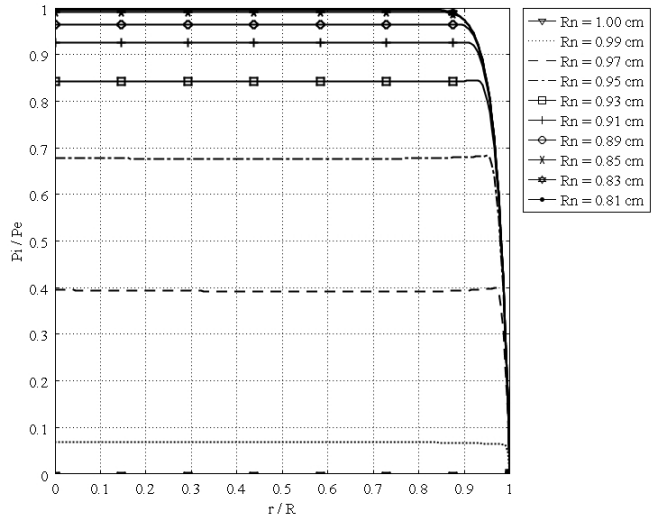

Figure 2.13: Interstitial pressure distribution in a $1cm$ radius tumor, as a function of the dimensionless radius for different necrotic radii

The same graph for all sizes of solid tumors studied in this paper is also shown in Figure 2.15. From this figure, for instance, for tumors below a certain size (in this case $0.1cm$), reaching effective pressure, even with a zero value for their necrotic radius, is not possible. Figures 2.16 to 2.18 show the same parameters as Figure 2.13 for the other three tumor sizes, which follow the same behavior as explained for Figure 2.13.

2.5 Discussion

The calculated value of IFV for the periphery of an isolated tumor, shown in Figure 2.6, is on the order of $10^{-7}m/s$, a finding that agrees well with experimental data in the literature [7, 38, 45, 14]. These results predict that the fluid filtration is negligible throughout most part of the tumor and occurs mostly from vessels in the periphery, a well vascularized region. Interstitial fluid pressure distribution for different values of α and different boundary conditions, Figures 2.7 and 2.12, shows that IFP is elevated throughout the tumor and goes down sharply in the periphery of an isolated tumor or at the normal tissue around an embedded solid tumor. The immediate result of this high IFP is decreasing blood flow and therefore insufficient delivery of drug. This general trend for IFP leads to

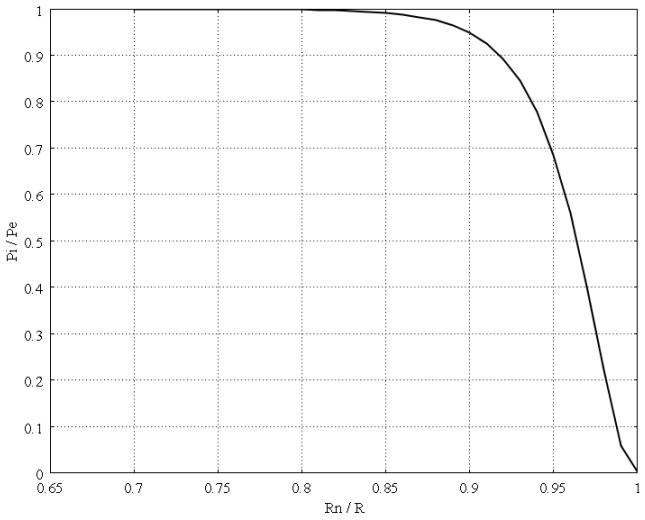

Figure 2.14: Interstitial pressure distribution at the center of a $1cm$ radius tumor, as a function of the dimensionless necrotic radius

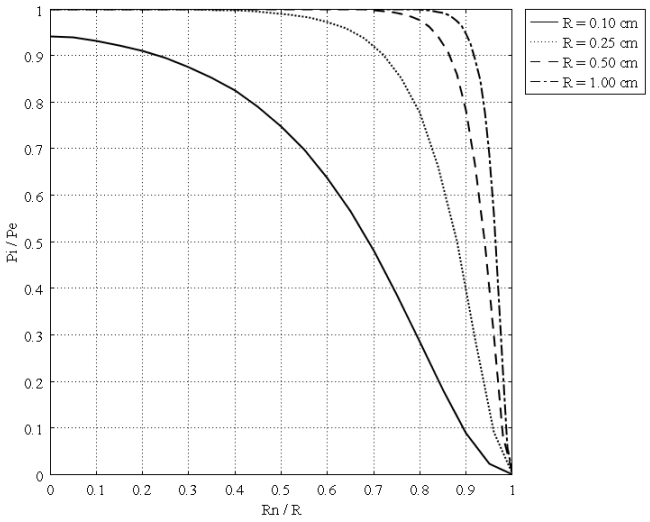

Figure 2.15: Interstitial pressure distribution at the center of different tumors, as a function of the dimensionless necrotic radius

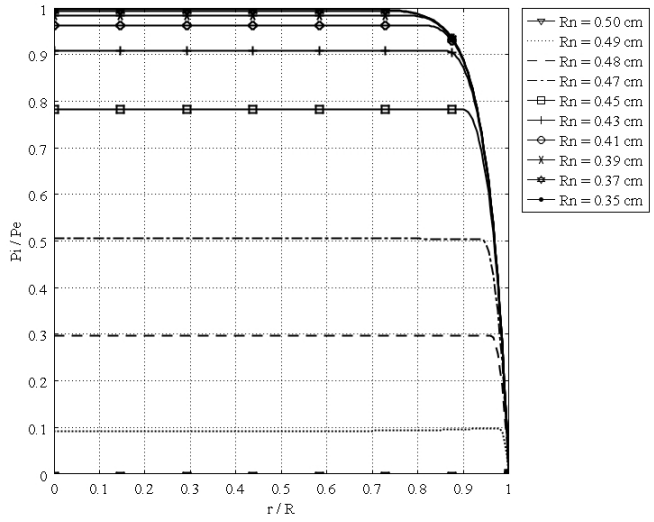

Figure 2.16: Interstitial pressure distribution in a $0.5cm$ radius tumor, as a function of the dimensionless radius for different necrotic radii

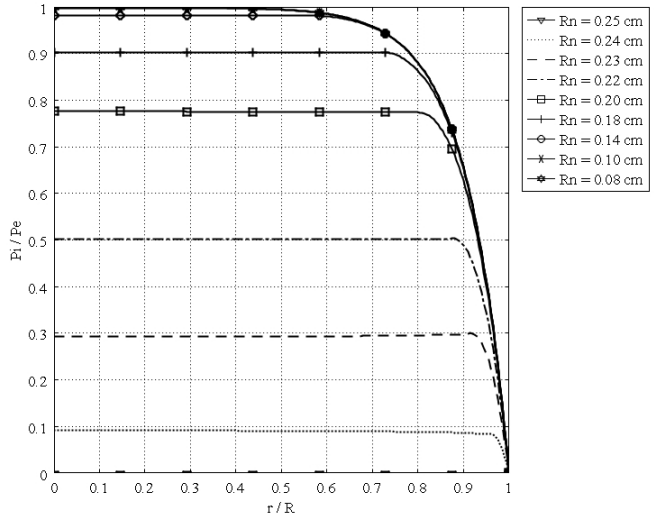

Figure 2.17: Interstitial pressure distribution in a $0.25cm$ radius tumor, as a function of the dimensionless radius for different necrotic radii

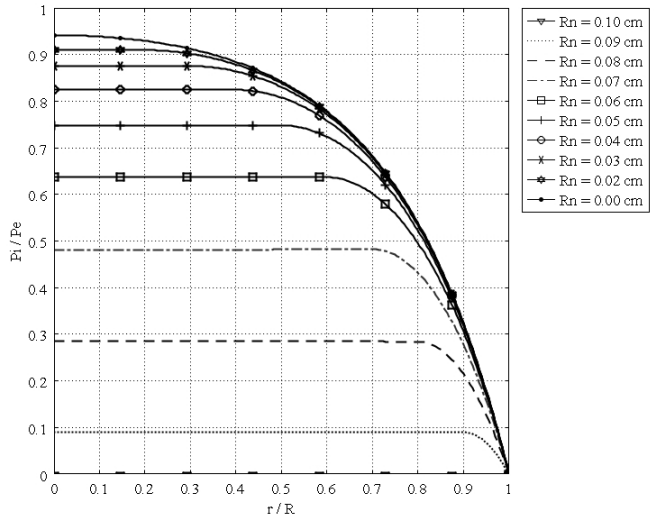

Figure 2.18: Interstitial pressure distribution in a $0.1cm$ radius tumor, as a function of the dimensionless radius for different necrotic radii

low drug filtration from blood vessels in the center of the tumor and high drug filtration in the tumor periphery, as shown in Figure 2.1. On the other hand, the large pressure gradient results in an outward convective flow that washes out the drug extravasated from blood vessels at the tumor periphery. All of these phenomena are indicated in Figure 2.1, schematically. In both cases, embedded and isolated tumor, IFP approaches P_e, effective pressure, in the center of the tumor where the fluid source is minimal, as shown in Figures 2.7 and 2.12. On the other hand, in the periphery, the opposite scenario occurs; there is minimum pressure and maximum fluid source. Based on the results of this study, drug delivery can be enhanced by decreasing IFP in the center of the tumor. This may not be easy to do, but there are some physical and enzymatic methods which can be applied. For instance, blocking the integrin links between an interstitial matrix and cells decreases IFP and enhances tissue fluid content. Also, irradiation by remodeling the extracellular matrix decreases IFP in solid tumors [68]. Comparing IFP distribution in tumors with different radii shows that IFP increases with tumor size. This study introduces two new parameters, the critical tumor radius and critical necrotic radius. For tumors below the critical tumor radius, the maximum interstitial fluid pressure is less than the effective pressure, no matter what the value of the necrotic radius is. In fact, the transport of the drug to the center of smaller tumors is much easier than transport to the center of a tumor whose radius is greater than the critical tumor radius, as the maximum IFP is much lower than effective

pressure, P_e. This study also shows that there is a critical necrotic radius, below which the interstitial fluid pressure at the center of the tumor approaches to its maximum value. If the tumor radius is greater than the critical tumor radius, this maximum pressure is equal to the effective pressure.

2.6 Conclusions

Numerical solutions for the simplest case of a homogeneous and alymphatic tumor demonstrate that, in a uniformly perfused tumor, high interstitial pressure is the main cause of heterogeneous drug distribution. The main assumption used to reach this conclusion is that drug particles flow with the interstitial fluid. The distribution of interstitial fluid pressure and velocity have been calculated by numerical solutions to the governing equations. Comparison of these numerical solutions and experimental data in the literature shows that the maximum value for the interstitial pressure occurs at the center of the tumor and decreases towards the periphery and that the numerical values of interstitial fluid velocity and the experimental results reported in the literature agree. Interstitial fluid pressure is not uniform whether the tumor vasculature is homogeneous or heterogeneous. Thus, in addition to the heterogeneous distribution of blood supply, high interstitial pressure plays a significant role in drug distribution in a solid tumor.

This study also shows that an increase in the necrotic radius decreases the maximum pressure inside the tumor; the tumor that is completely necrotic has no vasculature, and thus its interstitial fluid pressure is zero. This study introduces two new parameters, the critical tumor radius and critical necrotic radius. Simulation results show that for tumors below the critical tumor radius, the maximum interstitial fluid pressure is less than effective pressure (a parameter determined by vascular pressure, plasma osmotic pressure, and interstitial osmotic pressure); therefore, the transport of the drug to the center of smaller tumors is much easier than transport to the center of a tumor whose radius is greater than the critical tumor radius, as the maximum interstitial fluid pressure is much lower than effective pressure. This study shows that there is a critical necrotic radius, below which the interstitial fluid pressure at the center of the tumor approaches to its maximum value. If the tumor radius is greater than the critical tumor radius, this maximum pressure is equal to the effective pressure. Above this critical necrotic radius, the interstitial fluid pressure at the center of the tumor is below effective pressure.

The numerical model investigated here can be further extended to apply to anisotropic tissues in terms of properties and geometry. Capillary distribution in real tissues is heterogeneous and non-uniform. This numerical model can handle this issue as well. Microcir-

culation studies show that for some drugs the relative size of nanoparticles is comparable to the capillary diameter; therefore, flow field has to be modeled as a two-phase flow. The numerical method introduced in this study has the capability of doing such a two-phase flow model.

Chapter 3

Effect of Tumor Shape and Size on Drug Delivery to Solid Tumors

3.1 Introduction

Cancer causes one in every four deaths in North America and is the second most common cause of death worldwide [43]. Solid tumors account for 85% of human cancers [43]. Although the most important cancer treatment is surgical removal of such tumors, the key to a successful cure often involves efficient delivery of anticancer drugs to the tumor site after the surgery. Many new drugs have been developed, but lack of an efficient means of delivery makes them less effective. Moreover, some of these drugs induce biochemical reactions in the body that produce toxicity. Bioengineers are primarily concerned with both the transport of drugs within the body (which usually involves systemic delivery through the blood supply) and with biochemical reactions or conversions at tumor sites [7, 45]. All of these problems demonstrate that solutions to drug delivery limitations are urgently needed [43].

Two factors inhibit the effective delivery of drugs within tumors: non-uniform blood supply and non-uniform interstitial pressure distribution [46, 40]. Drugs concentrate most readily in areas with the best blood supply. In solid tumors, these areas are closest to the blood vessels (the vasculature) and a tumor's peripheral walls; however, 90% of a tumor receives little or no drug, meaning that treated tumors tend to regrow, as only their outer cells have been killed by the drug [51, 87, 34, 12]. Variations in the interstitial (i.e., of connective tissue in which cells are embedded) pressure, from its minimum value at the

tumor surface to its maximum value at the tumor center, reduce fluid exchange (filtration flux) and further inhibit the movement of the drug into the center of the tumor.

Previous research has shown that drugs administered systemically are not uniformly reaching tumor sites. In addition to blood flow heterogeneities and impeded interstitial transport, another mechanism effectively contributes to the non-uniform distribution of drugs: high interstitial pressure in solid tumors [38, 39, 44]. High interstitial pressure limits drug transport in two ways: 1) it reduces the driving force that is the result of the interstitial fluid pressure and vascular pressure difference; 2) it moves fluid to the outer layers of the tumor in which the interstitial pressure has its minimum. Both these effects are shown schematically in Figure 3.1. The first effect decreases the driving force for transcapillary exchange of fluid and, therefore, drugs. Low filtration (liquid source per tissue volume) occurs at the center of the tumor as a result of the high interstitial pressure or low driving force, and high filtration occurs at the periphery of the tumor as a result of the low interstitial pressure or high driving force. The second effect of the high interstitial pressure results in a radially outward convective flux in the interstitium as fluid flows towards the outer layers of the tumor. This effect is illustrated in Figure 3.1 as an outward convection due to interstitial fluid pressure gradient. The value of the radially outward fluid velocity at the tumor rim for a solid tumor (mammary adenocarcinoma s.c.) with a $1cm$ radius, $4.2g$, is $0.1 \sim 0.2\mu m/s$ [7]. Figure 3.1 demonstrates another important feature of drug delivery to tumors: an inward diffusion due to concentration gradient of the drug. Effective penetration into a solid tumor requires that the velocity of the diffusion process be more than that of the convection process [41]. On the other hand, uniformly distributed high interstitial pressure in the center of a tumor results in heterogeneous distribution of drugs [44].

Modeling drug delivery involves processes such as drug diffusion, convective transport in extracellular matrices, drug extravasation from blood vessels, tissue elimination by the lymphatic system, and intracellular internalization. In all of these processes, computational fluid dynamics (CFD) can play a crucial role in clarifying the mechanisms of drug delivery from the injection site to absorption by a solid tumor. *In-vitro* release profiles of systemically administered drugs have been combined with state of the art computational fluid dynamics simulations to predict both temporal and spatial drug delivery in many studies [103, 99, 33, 101, 100, 104]. Temporal and spatial changes in blood flow have also been studied with a focus on capillary-network or single-vessels [75, 19]. The main focus of future drug delivery modeling involves the transport of the drug in tissues after drug release by either systemic administration or implantation.

As spherical tumors are the easiest to examine analytically, they have been used in most studies. The effect of tumor shape has not been addressed in the literature except

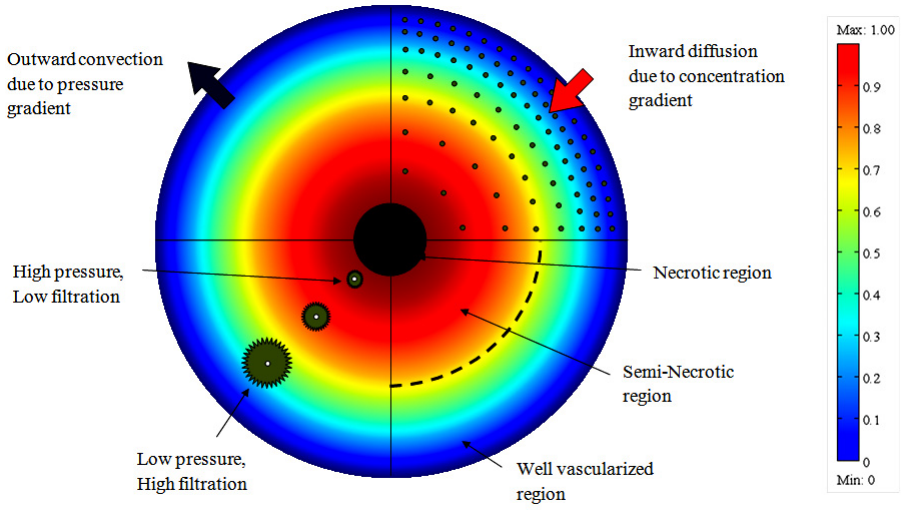

Figure 3.1: Cross sectional schematic of a solid tumor that shows the three different regions of a solid tumor, IFP distribution, drug concentration and filtration distribution from blood vessels [92]

the analytical study of by El-Kareh and Secomb [29]. The numerical method introduced here allows modeling of more complex shapes and promotes a better understanding of the complex mechanisms of interstitial fluid transport that effective drug delivery must depend on. In studying tumor modeling, the numerical method, which introduces more features of drug delivery to solid tumors, is more effective than the analytical method.

The proposed CFD model is made for both spherical and non-spherical tumors and their surrounding normal tissues. This model can be further extended to study geometries reconstructed from high resolution images. In this study the tumor and its surrounding tissue are assumed to be rigid porous media. The vasculature as a source term varies spatially. The grid generation divides the whole domain or geometry into finite volumes, called meshes. Interstitial fluid flow equations in porous media are solved using a CFD code (based on the proposed CFD model) that employs unstructured grids (tetrahedral elements) to handle non-spherical tumors.

3.2 Mathematical Model of Interstitial Fluid Transport in General Form

The tissues most relevant to this discussion are the vasculature (vessels that, with the heart, comprise the circulatory system that carries blood throughout the body), the interstitium (or interstitial space), and the cells. Also relevant is the lymphatic system, which, simply put, is responsible for tissue drainage. The vasculature system involves vessels (essentially tube-like structures) of varying sizes, from the large arteries and veins down to the much smaller arterioles, venules and capillaries [16]. The interstitium is formed of fibers such as collagen, which gives structural stability, glycosaminoglycans (GAG), and other proteins. Together, these fibers make up the gel-like region between blood vessels and cells. The cells, occupying the cellular space, include specific tissue cells (i.e., the cancer cells of a solid tumor) and others such as pericytes, macrophages, and fibroblasts not discussed in this study [7, 8, 9]. In normal physiology, fluid seeps slowly but constantly from blood vessels into the surrounding tissues. The lymphatic system then reabsorbs this lost fluid and returns it to the blood stream. All the above tissues must be considered in any discussion of drug delivery to tumors. Specifically, to be effective, drugs must cross the blood vessel wall, traverse the interstitial space containing the cancer cells, and bind to and (if the target is intracellular) penetrate the cancer cell membrane. The lymphatic system then removes excess fluid and debris. However, a lack of such lymphatic drainage in solid tumors has been reported in the literature [7, 45]. Computer simulations show that this lack of lymphatic system involvement may result in a build up of interstitial pressure, leading to cessation of the usual blood seepage from vessels. Consequently, large molecules cannot be carried out of vessels to interact with tissue. As some drug particles, including Monoclonal Antibodies (MAbs) used to fight cancer, are large and move very slowly within tissues, they cannot reach the tumor site and are thus ineffective [7].

The mathematical model used for interstitial fluid transport has been described in the previous Chapter in detail. To apply that model to different shapes of solid tumors, it is necessary to work on a more general form of the governing equation.

Rearranging Equation 2.9 for an arbitrary shape of a solid tumor results in

$$\nabla^2 P_i = \frac{L_P S + L_{PL} S_L}{kV}(P_i - P_{ss}) \tag{3.1}$$

Equation 3.1 for a spherical solid tumor with radius R is written as,

$$\nabla^2 P_i = \frac{\alpha^2}{R^2}(P_i - P_{ss}) \tag{3.2}$$

which is the same as Equation 2.10.

P_{SS} is defined later by Equation 3.6. Using the definition of the Laplace operator, Equation 3.3, in the spherical coordinate system, Equation 3.2 is written as in Equation 3.4.

$$\Delta = \nabla^2 = \frac{1}{r^2}\frac{\partial}{\partial r}\left(r^2\frac{\partial}{\partial r}\right) + \frac{1}{r^2\sin\theta}\frac{\partial}{\partial\theta}\left(\sin\theta\frac{\partial}{\partial\theta}\right) + \frac{1}{r^2\sin^2\theta}\frac{\partial^2}{\partial^2\phi} \tag{3.3}$$

$$\frac{1}{r^2}\frac{\partial}{\partial r}\left(r^2\frac{\partial P_i}{\partial r}\right) = \frac{\alpha^2}{R^2}(P_i - P_{ss}) \tag{3.4}$$

In Equations 3.2 and 3.4, the ratio of interstitial resistance to vascular resistance is introduced in terms of α, the dimensionless parameter defined by Equation 3.5.

$$\alpha = R\sqrt{(L_P S + L_{PL} S_L)/kV} \tag{3.5}$$

$$P_{SS} = (L_P S P_e + L_{PL} S_L P_L)/(L_P S + L_{PL} S_L) \tag{3.6}$$

The steady state pressure, P_{SS}, is the interstitial pressure at which the efflux from the vasculature and influx into the lymphatics are equal, and is defined by Equation 3.6. Effective pressure, P_e, in Equation 3.6, is a parameter defined by vascular pressure, plasma osmotic pressure, and interstitial osmotic pressure through Equation 3.7.

$$P_e = P_B - \sigma_s(\pi_B - \pi_i) \tag{3.7}$$

Applying the appropriate boundary conditions and also all the constants mentioned earlier, the more general form of the governing equation, Equation 3.1, can be used to calculate the interstitial fluid velocity (IFV) and interstitial fluid pressure (IFP) profiles in solid tumors. Of note, for spherical solid tumors, simpler forms of the governing equation, Equation 3.2 or 3.4, can be used. Additionally, α is a dimensionless constant used here for convenience (only in spherical tumors); in general (arbitrary shapes), more fundamental physical constants such as L_P, S, L_{PL}, S_L, k, and V, used in Equation 3.1, should be used.

No lymph vessels in a solid tumor means $S_L = 0$; thus, Equations 3.1, 3.4 and 3.5 can be simplified as follows:

$$\nabla^2 P_i = \frac{L_P S}{kV}(P_i - P_e) \tag{3.8}$$

$$\frac{1}{r^2}\frac{\partial}{\partial r}\left(r^2 \frac{\partial P_i}{\partial r}\right) = \frac{\alpha^2}{R^2}(P_i - P_e) \tag{3.9}$$

$$\alpha = R\sqrt{(L_P S)/kV} \tag{3.10}$$

in which the interstitial pressure that yields zero net volume flux out of the vasculature is called the effective pressure, P_e, Equation 3.7. The steady state pressure and effective pressure in solid tumors with no lymph vessels are the same. If $P_i = P_e$, no exchange of fluid occurs between the interstitial space and blood vessels.

Due to symmetry, there is a no flux boundary condition at the center of the tumor; i.e.,

$$\nabla P_i = 0 \quad \text{or} \quad \frac{\partial P_i}{\partial r} = 0 \qquad \text{for } r = 0 \tag{3.11}$$

At the outer edge of the solid tumor, ($r = R$ for a spherical tumor), two types of boundary conditions are possible. In the first type, where the pressure in the surrounding tissue is fixed, the tumor pressure at the outer edge is the same as the surrounding pressure, P_{sur}.

$$P_i = P_{sur} \qquad \text{for outer region, } r \in \Omega \tag{3.12}$$

This condition is applicable for an isolated tumor [36, 14]. In the second type, the solid tumor is surrounded by normal tissues. Pressure decreases smoothly over a distance; therefore, the continuity of pressure and velocity should be considered as an appropriate boundary condition for this case as the following conditions occur simultaneously:

$$-k_t \frac{dP_i}{dr}\bigg|_{\Omega^-} = -k_n \frac{dP_i}{dr}\bigg|_{\Omega^+} \tag{3.13}$$

$$P_i|_{\Omega^-} = P_i|_{\Omega^+} \tag{3.14}$$

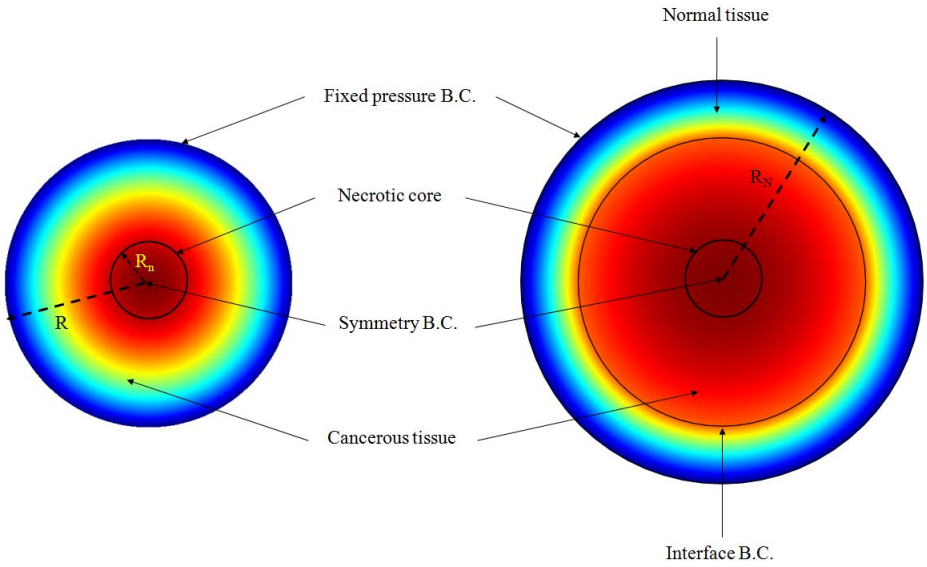

Figure 3.2: Two types of boundary conditions at the outer edge of the tissue [92]

where Ω^- and Ω^+ indicate the tumor and normal tissue at the outer edge of the solid tumor; k_t and k_n are the hydraulic conductivity of the interstitium in tumor and normal tissues, respectively. It should be noted that, in the second type, all the equations mentioned for the tumor tissue have to be solved for the normal tissue as well. For the normal tissue, far enough from the solid tumor that the pressure is constant, the first type of boundary condition, Equation 3.12, must be applied. Figure 3.2 shows these two types of boundary conditions. The solution can now be obtained analytically or numerically to find the IFV and IFP profiles for each of the two boundary conditions. In this work, the same numerical method explained in detail in Chapter 2 has been used. In order to check the grid independency of the code, the largest tumor in this study is chosen and the results for three different grids are compared, indicating the conservative property of the numerical method. The final choice of the grid in this test case includes 11904 control volumes. For other tumor geometries the same mesh parameters are applied.

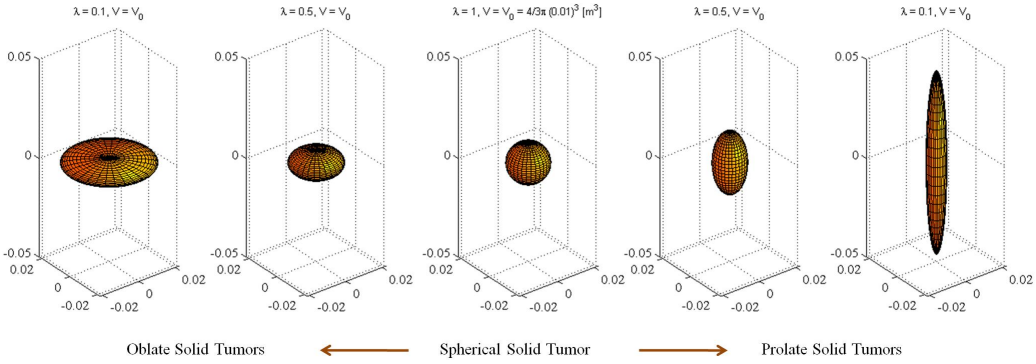

Figure 3.3: Different shapes of solid tumors: spherical, oblate, and prolate

3.3 Results

The actual tumor shape is not necessarily spherical. How to handle the patient's specific tumor and tissue dimensions in transport equations is discussed in the literature [51]. To study different shapes of solid tumors – spherical, oblate (flattened), and prolate (elongated) – shown in Figure 3.3, the governing equation is solved numerically [92]. Generally speaking, it is believed that increasing the hydraulic conductivity of tumor vessels increases the drug delivery to tumor cells. Many researchers, such as Sands et al. [87], Khawli *et al.* [53], LeBerthon *et al.* [55], and Cope *et al.* [22], have stated the abovementioned hypothesis and tried to explain their experimental results based on it.

Figure 3.4 shows the volumetric flow rate out of the vasculature per unit volume, also called liquid source per tissue volume or filtration flux, at the different tumors' centers as a function of the multiplication of hydraulic conductivity of the microvascular wall and surface area per unit volume, based on Equation 2.5, which can be rewritten as Equation 3.15:

$$\phi_B(r) = \frac{J_V}{V} = \frac{L_P S}{V}(P_e - P_i) \tag{3.15}$$

The parameters used in Equation 3.15 are $\frac{J_V}{V}[s^{-1}]$, the volumetric flow rate out of the vasculature per unit volume of tissue; $\frac{S}{V}[cm^{-1}]$, the surface area per unit volume for transport in the tumor; $L_p[\frac{cm}{mmHg\ s}]$, the hydraulic conductivity of the microvascular wall; $P_e[mmHg]$, the effective pressure; and $P_i[mmHg]$, the interstitial fluid pressure. All parameters used to solve this equation are listed in Table 2.1.

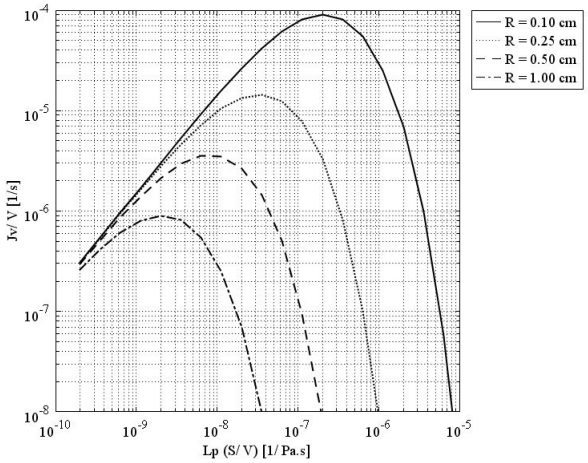

Figure 3.4: Liquid source (Volumetric flow rate out of the vasculature per unit volume of tissue or filtration flux) per tissue volume at the tumors' center, as a function of multiplication of hydraulic conductivity of the microvascular wall and surface area per unit volume

Figure 3.4, shows that in a spherical solid tumor with a certain radius, R, if hydraulic conductivity is increased, the volumetric flow rate first increases to reach an optimum value (maximum) and then decreases. This graph also indicates that an increase in the diameter of spherical solid tumors causes a decrease in the optimum value of the volumetric flow rate. Decreasing one order of magnitude of tumor radius increases the volumetric flow rate approximately two orders of magnitude. This optimum value occurs in response to a small value of hydraulic conductivity in spherical solid tumors with a relatively larger diameter. The values of hydraulic conductivity that result in optimum values of the flux are called optimum values of hydraulic conductivity. The filtration flux (or the volumetric flow rate), shown in Figure 3.4 as a function of L_pS/V, indicates that the usual values for L_p or S/V in the literature, listed in Table 2.1, are much greater than the optimum values shown in this graph. L_p^{opt}, the optimum value of hydraulic conductivity, can be found easily in a graph such as Figure 3.4 for different tumor sizes, or one can find the appropriate size for a specific tumor tissue with a known value of L_p to have the maximum drug flow rate. In Figure 3.4, L_p changes linearly from its minimum values to its maximum values. On the other hand, the pressure difference (between effective pressure and IFP) changes from P_e (when IFP is equal to zero) to zero (when IFP is equal to the effective pressure). When L_p is at its minimum, the pressure difference is at its maximum, and vice versa. This

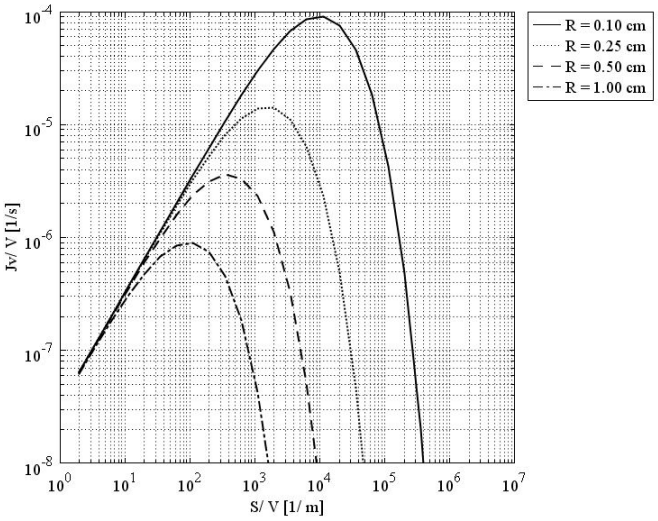

Figure 3.5: Liquid source per tissue volume at the tumors' center, as a function of surface area per unit volume

circumstance results in a peak in the volumetric flow rate curve in terms of the hydraulic conductivity of the microvascular wall, L_p, and surface area per unit volume, S/V, or a combination of these factors through Equation 3.15.

Baxter *et al.* [44] stated that, with a decrease in the surface area of the tumor vasculature, the amount of fluid filtered and therefore the amount of drug filtered decreases as well. However, Figure 3.5 shows that this statement is true for just part of the curves. The same behavior occurs for surface area per unit volume instead of hydraulic conductivity; the graph showing this similarity is shown in Figure 3.5.

For most cancerous tissues, the hydraulic conductivity of the interstitium is not reported accurately in the literature [29]. For those cases reported in the literature, such as recent work of Linninger *et al.* [59] on estimating the hydraulic conductivity in porous brain tissue, one can use inverse method and apply numerical method presented in this study to calculate the hydraulic conductivity and compare it with the estimated value in [59]. However, the change in k has been studied here, and the result, shown in Figure 3.6, indicates that k and L_p have opposite effects on filtration flux. Figure 3.6 shows the behavior of volumetric flow rate as a function of the hydraulic conductivity of the interstitium at the centers of spherical tumors of different radii. This figure demonstrates that in smaller tumors ($0.1cm$ radius in this case) the maximum value of the volumetric flow rate occurs in a smaller

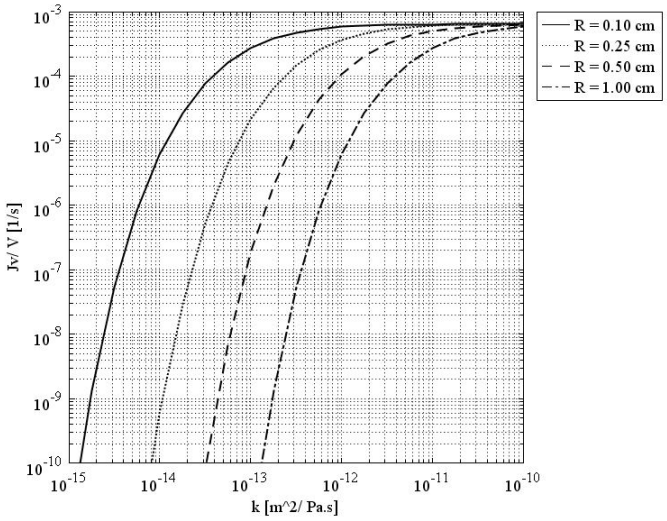

Figure 3.6: Liquid source per tissue volume at tumors' center, as a function of the hydraulic conductivity of the interstitium

value of the hydraulic conductivity of the interstitium, at least two orders of magnitude less than that of the larger tumor with a $1cm$-sized radius. In fact, increasing the value of k, decreases the amount of α. Low amounts of α result in low values of IFP. Based on Equation 3.15, the effect of low IFP values is an increase in the volumetric flow rate.

Figure 3.7 shows that in a spherical solid tumor of a certain diameter, with an increase in α, which is the dimensionless parameter defined based on Equation 3.10, the volumetric flow rate increases first, but after reaching an optimum value (maximum), it decreases. The interesting point about this graph is that the optimum values of the volumetric flow rate for different sizes of spherical solid tumors occur at the same value of α. This figure demonstrates that increasing one order of magnitude of tumor radius decreases the volumetric flow rate approximately two orders of magnitude at the same value of α^2, almost equal to 6. The simultaneous effect of effective pressure, P_e, and size is shown in Figure 3.8. The pattern for different sizes is the same; the more the effective pressure, the more the volumetric flow rate. As discussed before [92] and shown in Figure 3.8, the lower the tumor size, the lower the IFP, which results in a more volumetric flow rate.

Real tumors have unusual shapes. To show the effect of tumor shape and size on P_i distribution and also the filtration flux for different values of L_p and S/V, the study in [29] has been loosely reworked here but with a different approach in terms of formulation and

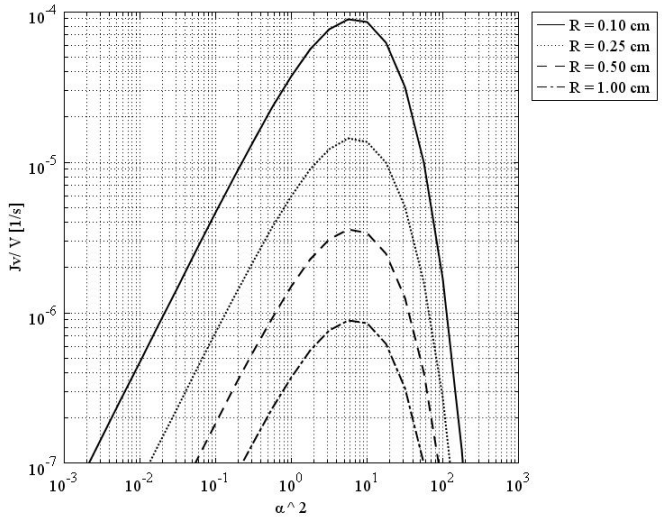

Figure 3.7: Liquid source per tissue volume at tumors' center, as a function of α, a dimensionless parameter

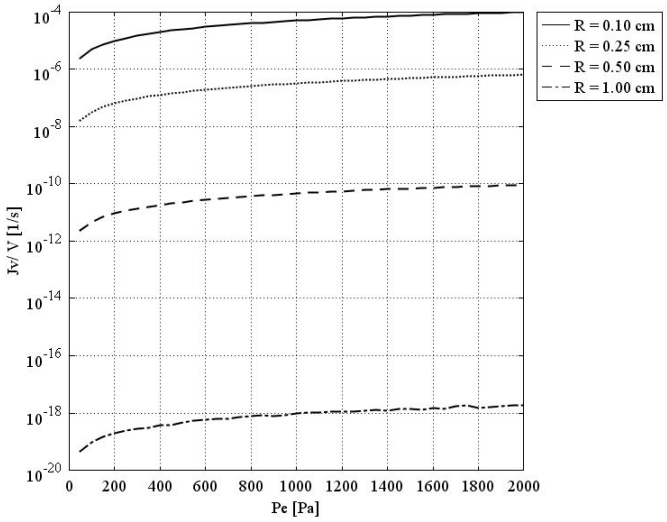

Figure 3.8: Liquid source per tissue volume at tumors' center, as a function of effective pressure

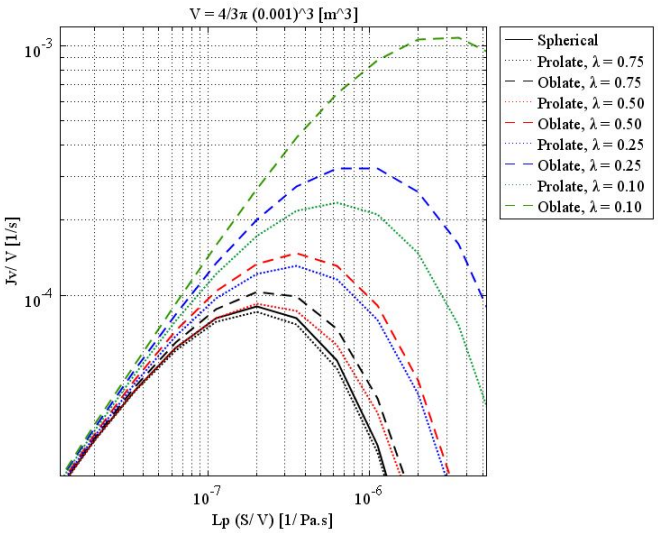

Figure 3.9: Liquid source per tissue volume at the center of different tumor shapes with the same volume as a spherical 0.1 cm radius tumor, as a function of multiplication of hydraulic conductivity of the microvascular wall and surface area per unit volume

solution method to cover a greater variety of tumor shapes and sizes. As mentioned earlier, the general form of the governing equation has been used in this Chapter to study non-spherical solid tumors, shapes not covered in the literature. Figure 3.9 shows volumetric flow rate behavior at the center of different tumor shapes that have the same volume as a spherical $0.1cm$ radius tumor, as a function of multiplication of the hydraulic conductivity of the microvascular wall and surface area per unit volume. Different colors show the different values of λ (or a/b), the ratio of minor to major axes of both prolate and oblate spheroids. Clearly, when λ is 1, all three shapes have become spherical. As is shown, the general pattern for different shapes (spherical, prolate, and oblate solid tumors) is the same. Rapid increase by the enhancement of hydraulic conductivity or surface area per unit volume to an optimum value (maximum), and then the decrease by enhancement of those parameters, is the main characteristic of Figures 3.9 to 3.12. Simultaneous effects of shape and size of the tumors on the flux (volumetric flow rate) distribution can be explained according to these four figures.

As the labels indicate, each figure is for a specific volume, which is the same for all three shapes and is based on the size of spherical shapes. These figures show that although, qualitatively, all three shapes have the same behavior, quantitatively, spherical and prolate

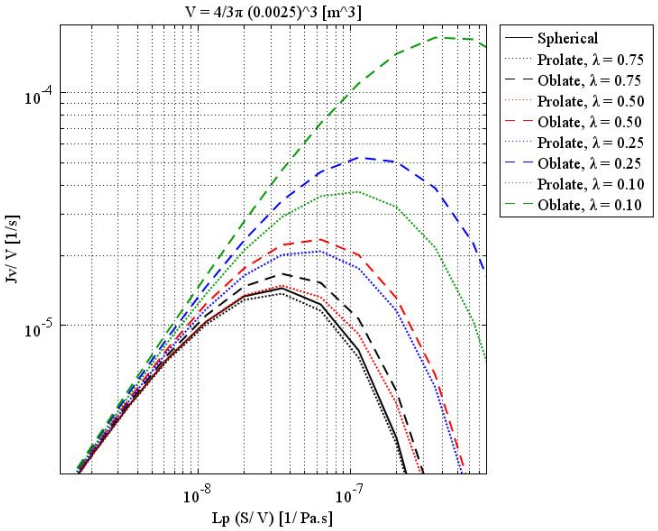

Figure 3.10: Liquid source per tissue volume at the center of different tumor shapes with the same volume as a spherical 0.25 cm radius tumor, as a function of multiplication of hydraulic conductivity of the microvascular wall and surface area per unit volume

solid tumors are very much closer to each other in behavior than they are to that of oblate solid tumors. This statement is truer for small tumors than larger ones and also for smaller values of λ. As discussed, by increasing the radius of solid tumors, the order of volumetric flow rate decreases, as through Figures 3.9 to 3.12. On the other hand, when λ approaches one, all three shapes show the same behavior. Figure 3.13 shows the interstitial pressure distribution at the tumor center for different values of λ (or a/b). It should be mentioned that for each curve, the volume is constant, and R_{eq} is the radius of a spherical tumor with the same volume as both prolate and oblate tumors. This figure indicates that, for large tumors, except for extremely low values of a/b, which occur with very thin shapes of tumors, the central pressure is independent of shape. This study also shows that there are two limits for the central pressure value: for large tumors, $R_{eq} > 0.25$ cm, $P_i \approx P_e$ (especially for prolate solid tumors), and for small tumors, $R_{eq} < 0.02$ cm, $P_i \approx P_{sur}$, no matter what the shape of the tumor. For sizes between these two limits, for example $R_{eq} = 0.1$ cm, as shown in Figure 3.13, the central pressure is a function of both tumor shape and size. Thus, for 0.02 cm $< R_{eq} <$ 0.25 cm, $P_{sur} < P_i < P_e$.

Two limiting cases (in which a prolate spheroid approaches cylindrical geometry and the oblate spheroid approaches a planar slab) are interesting to study with more detail.

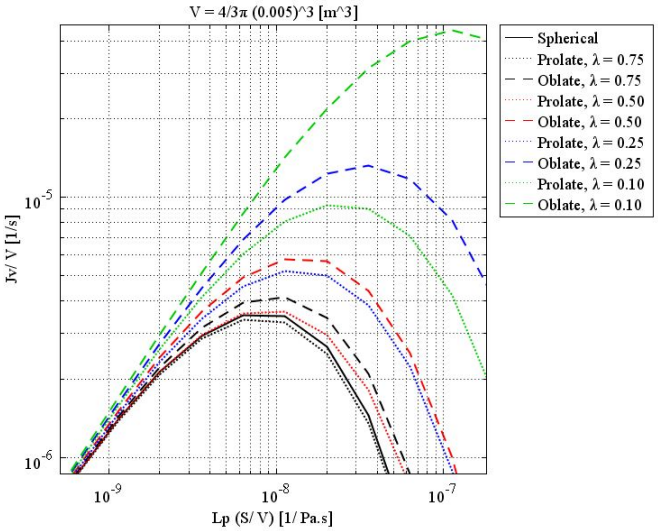

Figure 3.11: Liquid source per tissue volume at the center of different tumor shapes with the same volume as a spherical 0.5 cm radius tumor, as a function of multiplication of hydraulic conductivity of the microvascular wall and surface area per unit volume

These limiting cases can be achieved by choosing the very low values of λ (0.01 in this case). The IFP distributions throughout these geometries for $R_{eq} = 1.0$ cm are shown in Figure 3.14 to specify the effects of size and shape more carefully in these cases. This figure shows that for non-spherical tumors, everything hinges on the smallest dimension, and the other dimension is not important. When the smallest dimension of the prolate tumor is close to or in a comparable size to the spherical one, the pressure distribution is almost the same, as shown in Figure 3.14. For the oblate tumor, as the order of the smallest dimension is very different from that of the spherical one, pressure distribution is

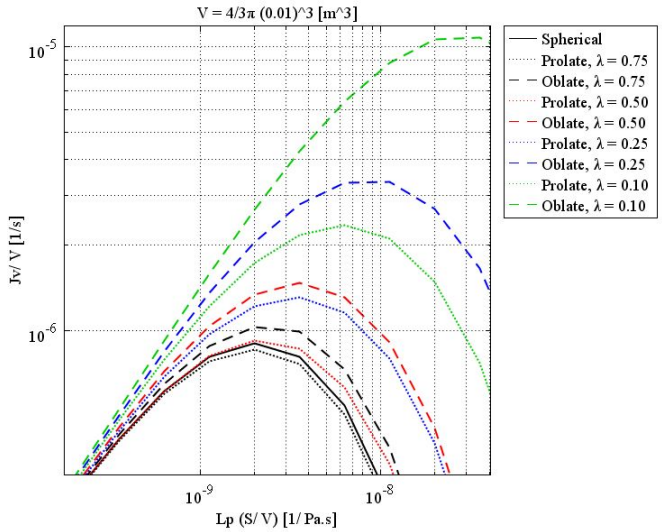

Figure 3.12: Liquid source per tissue volume at the center of different tumor shapes with the same volume as a spherical 1.0 cm radius tumor, as a function of multiplication of hydraulic conductivity of the microvascular wall and surface area per unit volume

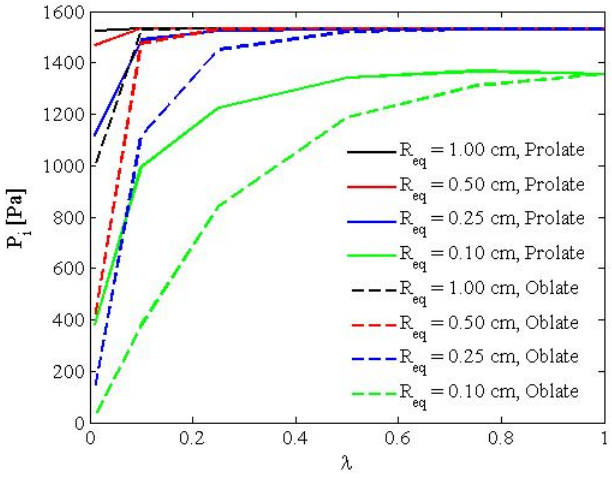

Figure 3.13: Pressure distribution at the center of different tumor shapes, as a function of minor to major axes ratio. R_{eq} is the radius of a spherical tumor with the same volume as both prolate and oblate tumors

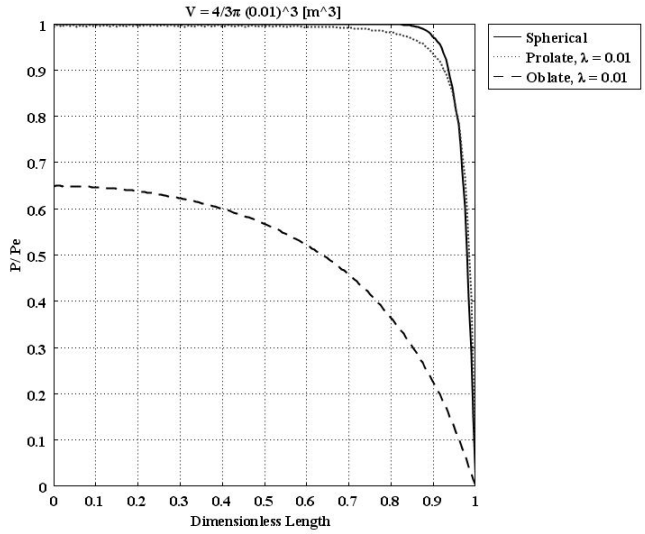

Figure 3.14: Pressure distribution of different tumor shapes with the same volume as a spherical 1.0 cm radius tumor, as a function of dimensionless length

totally different in Figure 3.14. The same figures as Figure 3.14 for other sizes of R_{eq} can be shown here.

3.4 Discussion

The effect of increasing the hydraulic conductivity of microvessels, L_p, in terms of drug delivery to solid tumors is significant to this discussion. There are two opposing phenomena: the total fluid filtration flux for the whole solid tumor and local filtration within the solid tumor; therefore, the liquid source term, the filtration flux at the center of the tumor, has its highest value for an optimum value of L_p, as shown by El-Kareh and Secomb [29]. As they have shown in their study analytically, and is indicated here numerically, this optimum value of L_p is a function of the size and shape of solid tumors. An increase in L_p has a direct effect on the total rate and an opposite effect on the local filtration flux. Increased vessel leakiness cannot result in more uniform drug distribution through tumors much larger than $0.25cm$.

Starling's law shows that, because of low diffusivity, the dominant form of drug transport through vessel walls (transvascular transport) is convection [29]. Based on Equation

3.15, both hydraulic conductivity of the vessel wall and pressure difference across the wall are effective in convective transport, again according to Starling's law. Similar behavior is true for S/V; thus, an increase in L_p and S/V does not have a positive effect, and there are optimum values for both of these parameters. However, the analysis of the work done in [29], as well as this study, shows that, except when the nodule radius is smaller than $0.1cm$, the advantage of decreasing P_i is more important than that of decreasing the surface area.

As indicated, an increase in the hydraulic conductivity results in a volumetric flow increase, but after a continued increase, volumetric flow approaches a certain value for all different tumors. This pattern for tumors of all diameters is the same; the only difference is that the smaller the tumor diameter, the sooner the leveling in volumetric flow.

The parameter α does not apply exactly in a non-spherical tumor; therefore, the general form of the governing equation, different from the more specific form of that applied in spherical solid tumors, has to be used here. This parameter, α, is a combination of other fundamental variables such as hydraulic conductivity, which turns out to have a clean short definition when solved for a sphere. This study shows that for a distinctly non-spherical tumor (such as a prolate or oblate), everything hinges on the shortest dimension, and the longer dimension is irrelevant, as any fluid or material flows to reach the closest surface.

Because El-Kareh *et al.* [29] used an analytical approach to solve the governing equations in prolate and oblate spheroidal shapes, they had to change the coordinate system from a spherical one to a more complicated coordinate system, with oblate and prolate spheroidal coordinates. In this coordinate system, the governing equation, the Helmholtz equation, has a much more complicated form than the original equation. The solution for this new form of equation is a Fourier series. In the work proposed here, the numerical method is applied and, obviously the solution is not limited to any specific shape, offering a freedom that is one of the main advantages of the numerical method over the previous one.

3.5 Conclusions

The parameter α/R is independent of tumor geometry. It is a function of hydraulic conductivity (an interstitial property) and vessel permeability. The main problem is defining a characteristic length instead of R in non-spherical tumors. The pressure profile, however, is a function of tumor geometry. Using a solution for IFP that was calculated assuming a spherical profile will give a solution as a function of α, r, and R. Not surprisingly, equations tailored to the different tumor shapes will yield different IFPs, as these pressures are the

outcomes of the equations, and thus reflect the discrepancies. What will happen, whether a tumor is a sphere or not, is that IFP will be approximately equal to the vascular pressure, P_B, throughout most of the interior. Only near the boundary, whether that boundary is for a sphere or spheroid, will there be a steep pressure gradient as IFP falls to the pressure of the surrounding tissue. For a very small radius, the differences will be significant. Above the critical radius, shape is almost irrelevant.

This study shows that, as a rule, it is not true that the leakier the vessels, the higher the value of convective transport of drugs to solid tumors. The results do show that only in spherical solid tumors with a radius of less than $0.25cm$, or in spheroidal ones with the same volume, can drug convection be increased by making vessels more leaky. For spheroidal shapes, the convection of drugs inside is higher than it is in spherical ones, and it seems that for more irregular shapes, which are generally found in the body due to limitations imposed by neighboring tissues and organs such as the brain, this effect is more marked.

For shapes studied in this paper, results show that the dependency of the maximized flux (as a function of L_p and S/V or their multiplication) on size is much stronger than its dependency on shape. It should be mentioned that due to very low diffusivity, the high permeability of vessels cannot support homogeneous distribution inside tumors because this high value results in more diffusive transport only in a narrow area around the vessels.

Chapter 4

Effect of Matrix Density and Matrix Degrading Enzymes in Continuous and Discrete Mathematical Models of Angiogenesis

4.1 Introduction

More than 85% of human cancers are in the form of solid tumors. The beginning of tumor development is avascular, which means that the tumor obtains its required nutrients and oxygen from the surrounding vasculature by diffusion. As the tumor gets larger, diffusion alone cannot provide enough oxygen and nutrients. Consequently, the tumor stops its growth and becomes dormant. The tumor is benign at this stage, and a complete cure could be achieved by surgery. However, as a result of hypoxia, the tumor may be activated again and start to secrete certain factors that induce nearby vessels to migrate toward the tumor. This stage, which has a pivotal role in tumor growth, is called angiogenesis.

Angiogenesis, the formation of new capillaries from existing blood vessels, is the bridge between the avascular and the fatal vascular tumor growth phases. Each cell in a multicellular organism has mechanisms to control its growth, proliferation, and death [62]. When these mechanisms are disrupted, the cell may undergo uncontrolled growth, leading to cancer. After angiogenesis, the tumor has its own blood supply, which provides enough oxygen and nutrients for further growth. In this stage, the tumor has vascular growth, and its growth rate is much higher than that of the avascular phase.

Angiogenesis is not limited to tumor development and is also observed in normal physiological processes like embryogenesis and fetal development. The difference is that, in the normal processes, it stops after accomplishing a general task such as wound healing, or formation of an organ in embryogenesis. In contrast, in solid tumor development, the process never stops.

Angiogenesis involves a cascade of events and many complicated processes. A comprehensive review and explanation of these process details are presented by Pawaletz and Knierim [72] and Carmeliet and Jain [17].

Generally, the following steps take place during angiogenesis [72]

1. Formation of a hypoxic region in a tumor and secretion of angiogenic factors
2. Activation of endothelial cells (ECs)
3. Degradation of basement membrane
4. Formation of vessel sprouts
5. EC proliferation and migration
6. Vessel lumen formation
7. Fusing of the neighboring sprouts to form loops (anastomosis)
8. Blood circulation through the new vessels
9. Stabilization of vessels

In angiogenesis, ECs are activated by substances, called growth factors, secreted by the tumor as a result of hypoxia, triggering a series of events:

1. Production of enzymes for degradation of the extracellular matrix (ECM)
2. Start of migration
3. Start of proliferation

Once the angiogenic factors such as vascular endothelial growth factor (VEGF) and basic fibroblast growth factor (bFGF) reach the ECs and bind to cell-surface receptors, numerous changes start to happen in the internal machinery of the ECs, and they are converted from a quiescent cell type to an active cell type that is able to migrate and proliferate.

The finger-like protrusions of ECs created due to these changes degrade the basal lamina adjacent to ECs and open the path for migration. In the initial steps of sprout formation, the cells are recruited from parent vessels, but after some advancement of sprouts in the ECM, the cells behind the tip cell start to proliferate. Matrix degrading enzymes (MDEs) are produced by the ECs to degrade the ECM and open the path for sprout migration.

MDE is a general term representing numerous proteases that degrade different proteins in the ECM. Two such proteases are the matrix metalloproteases (MMPs) and serine proteases. MMPs are a group of MDEs that are able to degrade all ECM proteins. There are more than 20 members in the MMP family, and they are identified by numbers and classified according to their preferential substrate or similar structural domain. As instances, collagenases, including MMP1, MMP8, and MMP13, are active against fibrillar collagen; gelatinases, including MMP2 and MMP9, have high activity against denatured collagens; and stromelysins, including MMP3, MMP10, and MMP11, act on non-collagen components of the ECM.

Serine proteases are another family of proteases. One of the most important serine proteases is the plasminogen activator-plasmin system. Plasmin is an activated form of the plasminogen and is active against various ECM components like fibrin, collagen, laminin, fibronectin, and proteoglycan.

The duty of proteases in the ECM is to facilitate EC movement. Two main mechanisms for EC movement have been considered: chemotaxis and haptotaxis [18]. Chemotaxis and haptotaxis are mainly responsible for EC migration toward tumors. Chemotaxis is the EC movement due to gradients of tumor angiogenic factors (TAFs), and haptotaxis is directed movement of EC toward adhesion gradients to components of the ECM like fibronectin. It should be mentioned that for the purpose of modeling, a third mechanism, random movement may be considered; however, it is not a physical movement mechanism and is introduced only to facilitate EC movement in models.

Any interruption in these consecutive events may lead to unsuccessful angiogenesis. This was the key idea presented by Folkman [30]. Prevention of angiogenesis can be accomplished in any possible state of its development, from production of tumor angiogenic factors to prevention of their binding to the cell-surface receptors of ECs. Today, antiangiogenic therapy is an accepted cancer therapy, although not used as the main method; it

can benefit patients by supplementing chemotherapy or radiotherapy [52].

Mathematical Modeling is a developing tool in biological simulations like angiogenesis modeling. *In vivo* and *in vitro* studies of angiogenesis are performed to observe tumor development stages and also tumor and EC behavior during angiogenesis. The limited number of assay systems and also difficulty in observing the details of successive angiogenesis events are drawbacks of *in vivo* studies; on the other hand, *in vitro* studies also have problems. ECs *in vivo* experience shear stress and hemodynamic forces that affect their behavior. ECs *in vitro* are cultured in mediums that are hyperoxic in comparison to *in vivo* conditions. Moreover, interaction of ECs with other cell types in ECM such as smooth muscle cells, perycites, etc., cannot easily be simulated *in vitro* [1]. In addition to these two main methods of angiogenesis study, mathematical modeling, dating to the 1970s and earlier, aims to help researchers in this field as a complementary method of investigation. The complex nature of the process makes mathematical models difficult to apply. The huge complexity of the process means that researchers must use complicated stochastic models to predict the behavior of capillaries during network formation [71, 63, 113, 106, 6].

From a mathematical point of view, angiogenesis is a multiscale problem [83]. Intracellular signal transduction leads to secretion of different factors and proteolytic enzymes. On a cellular scale, the interaction between ECs and the ECM is of primary importance, and on an extracellular scale, diffusion and distribution of angiogenic factors in the ECM should be considered. Mathematical modeling on each of the above scales has been performed with different approaches and levels of complexities. Mathematical modeling of angiogenesis, if mature enough to consider essential requirements of the process, could help researchers to predict the behavior of ECs and tumors under various conditions. Moreover, it could provide significant help in the antiangiogenic therapy and drug delivery studies that are among the main cancer research areas.

Mathematical models of angiogenesis can be categorized by three main modeling techniques: continuous, discrete and hybrid [83], each involving several models and methods. This work focuses on two specific continuous and discrete models. The continuous model uses differential equations and is based on the mass conservation equation and chemical kinetics. Cells are represented as continuous aggregates, without the necessity to consider cells alone. This model gives overall good qualitative results but is not able to model the morphological details of the sprouts during migration [4, 70].

The discrete method of angiogenesis modeling uses the same kind of equations as does the continuous method but with different interpretation of the quantities [113, 4]. This method is able to model the growth and motility of ECs. Morphological details of a capillary network can be observed clearly in this model, and it can model branching and

anastomosis during formation of the capillary network [98]. The advantages of this model make it suitable for use in more-detailed models that consider flow and its effects on the angiogenesis process [96, 97, 64].

The assumptions used in the continuous and discrete models of angiogenesis in previous works need more investigation to exhibit the real physics of the problem. Moreover, the effect of matrix density and its interaction with the MDE has not been observed in the continuous and discrete models. Although MDE has been considered in some earlier studies [97], its effect has not been shown separately to assess its importance and role in the models. This current work does study the effect of MDE and matrix density on the continuous and discrete models of angiogenesis. As well, using modifications to the equations for continuous and discrete models, a model that implements real physical conditions is attempted.

This work, based on the model presented by Anderson and Chaplain [4] and used in some subsequent works [96, 63, 15, 107], presents a model that includes the effect of matrix density on capillary network formation. This effect was imposed on the model by including a function in the movement potential term in the equations. The chemotaxis function was also modified to make the capillaries accelerate as they get closer to the tumor. To capture the real physics of the problem, we replaced the initial and boundary conditions of the model presented by Anderson and Chaplain with certain real physical conditions, including the initial distribution of TAF and fibronectin in the domain. Because of the above modifications on the base model, our model predicts capillary network formation based on real initial conditions, and the effect of matrix density is regulated by imposing a function. This work also implements the MDE on the continuous model of angiogenesis. Since the continuous model is the basis of the discrete model, the modifications of the model make a better connection between the continuous and discrete models and change the effect of the MDE from a local effect to a more extensive one. Our results do not refute the results of Anderson and Chaplain, but, being based on real initial and boundary conditions with some modifications, our results include the effect of matrix density and capillary movement acceleration.

4.2 Continuous Mathematical Model of Angiogenesis

Once the ECs are activated by the VEGF, they start to migrate toward the VEGF gradients. Migration of ECs in the continuous model is modeled as the movement of aggregates that represent the ECs. The aim of this model is to capture the EC motion in the ECM. This model cannot give quantitative results and morphological details of EC motion; instead, its importance is in its basic equations, which construct the discrete model.

Three major mechanisms of motion have been considered in this model: random motility, chemotaxis and haptotaxis. Other mechanism for inhibition of angiogenesis such as the effect of endostatin and andostatin could also be included in the model [107]. Each of the motion terms can be described by the corresponding gradient of the motion stimuli and suitable coefficients.

The first motion mechanism is random motility of the cell. For random motility, which is modeled like the diffusion of mass due to the concentration gradient, the gradients of EC density make a flux of ECs [4]

$$J_{random} = -D_n \nabla n \tag{4.1}$$

where D_n is the random motility coefficient of EC, and n is the EC density.

The second motion mechanism is chemotaxis, which is related to the gradient of TAF concentration. TAF is secreted by tumors in response to hypoxia. It diffuses through the ECM and activates the ECs. In previous works [4, 63, 113], chemotactic effect has been considered to decrease as ECs move toward the tumor. This effect has been introduced by a function whose value is reversely proportional to the TAF gradient [4]. The chemotactic function has been modified in this present work to capture more realistic behavior in the growing capillaries. According to observations [31], the tip of a growing capillary should accelerate as it approaches a tumor. There are also mathematical models that are in agreement with the observation about acceleration of tip cells [57]. To implement this behavior in the model, the effect of chemotaxis has been considered to increase during its migration toward the tumor. The flux of ECs due to the TAF gradient is proportional to the TAF gradient and EC density [4].

$$J_{chemotaxis} = \tau(c) n \nabla c \tag{4.2}$$

where c is TAF concentration, and $\tau(c)$ is the chemotactic function, which is considered to increase linearly with increasing TAF concentration.

$$\tau(c) = \tau_0(1 + \kappa c) \tag{4.3}$$

where τ_0 is a chemotactic coefficient and κ is a positive constant.

The ECM contains various components, including interstitial tissue, collagen fibers and fibronectin. Fibronectin is a macromolecule in the matrix and enhances the adhesion of ECs to matrix components through integrin. Fibronectin is produced by both ECs and matrix molecules such as fibroblast; however, the contribution of matrix molecules is much

greater than that of ECs [57]. This phenomenon suggests an almost uniform distribution of fibronectin in the domain. It should be noted that, in the case of non-uniformity in the domain components, non-uniformity in the fibronectin production is expectable. In the presence of a fibronectin gradient, an adhesive gradient is established in the ECM, which directs the migration of ECs. During the migration, ECs search for stronger adhesion to promote their adhesive bonds. Directional migration of ECs up an adhesive gradient in the ECM is called haptotaxis, which is the third mechanism of EC migration in this model.

Haptotaxis flux is considered to have the following form [4]:

$$J_{haptotaxis} = \psi n \nabla f \tag{4.4}$$

where f is the fibronectin concentration and ψ is the haptotactic coefficient.

In previous works [4, 96, 63, 15, 107], the effect of matrix density has not been observed. Matrix density controls the migration speed of ECs and also their behavior. It has been shown both numerically [6] and experimentally [90] that in low matrix densities, ECs cannot establish a connection with matrix fibers, and so migration will not occur. In this case, a kind of discontinuity is observed in the ECs, and they cannot form capillaries. Moreover, at high matrix density, the dense medium of the ECM acts as a barrier and reduces migration speed. Thus, the EC density flux due to the gradient of fibronectin and TAF is multiplied by a function representing matrix density:

$$J_{chem-hapto} = J_{chemotaxis} + J_{haptotaxis} = R(\rho)[\tau(c) n \nabla c + \psi n \nabla f] \tag{4.5}$$

where $R(\rho)$ is the function-regulating effect of matrix density in the model. The total flux of ECs is given by the following equation:

$$J_n = J_{random} + J_{chem-hapto} \tag{4.6}$$

These three motion mechanisms together form a conservation equation for cell density. The final conservation equation for EC density is given by the standard form of the conservation equation [4].

$$\frac{\partial n}{\partial t} + \nabla . J_n = 0 \tag{4.7}$$

Inserting the corresponding J for each term results in a partial differential equation for EC concentration.

$$\frac{\partial n}{\partial t} = D_n \nabla^2 n - R(\rho) \nabla . [\tau(c) n \nabla c + \psi n \nabla f] \tag{4.8}$$

There are three dependent parameters in Equation 4.8, i.e., n, c and f, which should be identified and updated during solution. EC density is updated from the above equation. Two equations, for TAF and fibronectin concentration, are needed in the domain to update the above expression for EC density in each time step. It can be assumed that TAF diffuses through the ECM with a common diffusion equation.

$$\frac{\partial c}{\partial t} = D_c \nabla^2 c - \theta c - B \tag{4.9}$$

In Equation 4.9, D_c is the diffusion coefficient of TAF, θ represents its decay rate, and B is the amount of TAF bound to the EC receptors. This equation gives the TAF concentration; however, as the scale of time in this equation differs considerably from the scale of time in the angiogenesis process, TAF concentration should be assumed to be independent of time during solution, i.e., TAF diffuses much more rapidly in the ECM than in the angiogenesis process, so its profile can be assumed to be steady. Despite the previous assumptions about the profile of TAF in the domain [4], dimensional analysis of the TAF dynamics shows that the profile of TAF in the domain is almost linear [5], so a linear profile has been assumed for the TAF concentration distribution in the domain. This distribution has its maximum value near the tumor and decreases to its minimum value near the parent vessel.

During migration of ECs in the ECM, there is some uptake and binding of TAF by cells, and these activities are modeled by a simple uptake equation as below [4]

$$\frac{\partial c}{\partial t} = -\lambda n c \tag{4.10}$$

where λ is a positive constant showing the uptake of TAF by ECs.

Regarding the background fibronectin production of ECM molecules, which is much more than the ECs production, a constant fibronectin profile is assumed in the domain.

The model for fibronectin production and uptake is given by the following formula [4]

$$\frac{\partial f}{\partial t} = \omega n - \mu n f \tag{4.11}$$

where ω represents the production of fibronectin by ECs, and μ represents its uptake.

The complete system of equations, containing an equation for EC density and two equations, one for TAF and one for fibronectin, is summarized below:

$$\frac{\partial n}{\partial t} = \underbrace{D_n \nabla^2 n}_{\text{random motility}} - \underbrace{R(\rho)\nabla.[\tau(c) n \nabla c + \psi n \nabla f]}_{\text{chemotaxis and haptotaxis}}$$

$$\frac{\partial c}{\partial t} = \underbrace{-\lambda n c}_{\text{uptake}} \tag{4.12}$$

$$\frac{\partial f}{\partial t} = \underbrace{\omega n}_{\text{production}} - \underbrace{\mu n f}_{\text{uptake}}$$

The solution domain in this problem is ECM, which has the parent vessel on one side and the tumor on the opposite side. The ECs start to migrate from the parent vessel to the tumor in the ECM. The solution domain is considered to be a square area with the dimensions $[0, L] \times [0, L]$, with the parent vessel on the left side and tumor on its right side.

The above set of equations is nondimensionalized to obtain a suitable form of the governing equations in a $[0, 1] \times [0, 1]$ domain.

$$\frac{\partial \acute{n}}{\partial t} = D\nabla^2 \acute{n} - Z(\rho)\nabla.[\chi_0(1 + \delta \acute{c})\acute{n}\nabla \acute{c} + \phi \acute{n} \nabla \acute{f}]$$

$$\frac{\partial \acute{c}}{\partial t} = -\eta \acute{n} \acute{c} \tag{4.13}$$

$$\frac{\partial \acute{f}}{\partial t} = \beta \acute{n} - \gamma \acute{n} \acute{f}$$

where $Z(\rho)$ is the nondimensionalized form of the matrix density function.

Dropping the primes for simplicity, the final form of the nondimensionalized equations is

$$\frac{\partial n}{\partial t} = D\nabla^2 n - Z(\rho)\nabla.[\chi_0(1 + \delta c) n \nabla c + \phi n \nabla f]$$

$$\frac{\partial c}{\partial t} = -\eta n c \tag{4.14}$$

$$\frac{\partial f}{\partial t} = \beta n - \gamma n f$$

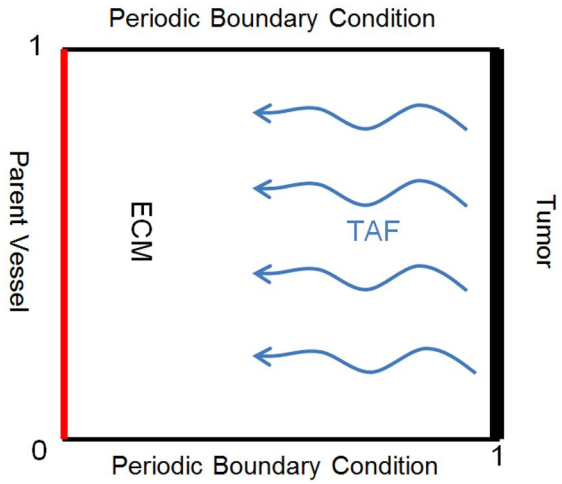

Figure 4.1: A schematic of the solution domain

The following nondimensionalized function is proposed for the effect of matrix density:

$$Z(\rho) = exp[-\frac{(\rho - \rho_0)^2}{2\sigma^2}] \tag{4.15}$$

It should be mentioned that the non-dimensional values of n, c and f used in nondimensional equations differ from their corresponding dimensional values.

A schematic of the solution domain is depicted in Figure 4.1. A periodic boundary condition is assumed for the top and bottom sides of the solution domain, and no flux boundary condition is assumed for the parent vessel and tumor.

$$\xi.\{D\nabla n - Z(\rho)[\chi_0(1+\delta c)n\nabla c + \phi n\nabla f]\} = 0 \tag{4.16}$$

where ξ is the normal outward unit vector.

An initial distribution should be considered for the EC density, the TAF, and the fibronectin concentrations. For the EC density, an initial distribution has been considered near the parent vessel with the profile in Equation 4.17 [4]

$$n(x, y, 0) = e^{-\frac{x^2}{\epsilon_3}} \tag{4.17}$$

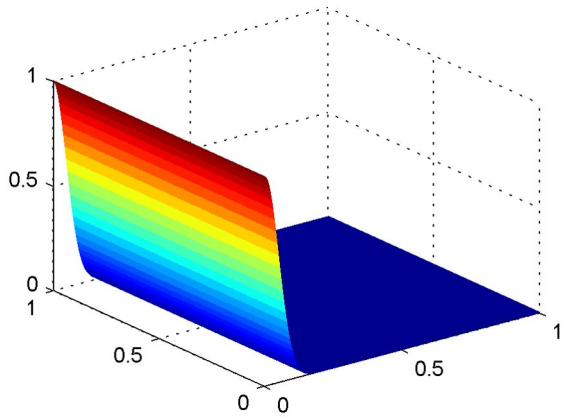

Figure 4.2: Initial endothelial cell density distribution in the domain

This profile, shown in Figure 4.2, provides an initial distribution of ECs near the parent vessel. For TAF, as shown in Figure 4.3, a linear profile has been assumed in the ECM. For fibronectin, as mentioned, a constant distribution has been assumed, as is shown in Figure 4.4.

Table 4.1 shows the set of parameters used in the solution. The parameters with an asterisk have been adapted based on the initial and boundary conditions for this model.

The governing equations are discretized by a finite difference scheme to a set of algebraic equations, shown below.

$$\begin{aligned} n_{i,j}^{q+1} &= n_{i,j}^{q} P_0 + n_{i+1,j}^{q} P_1 + n_{i-1,j}^{q} P_2 + n_{i,j+1}^{q} P_3 + n_{i,j-1}^{q} P_4 \\ f_{i,j}^{q+1} &= f_{i,j}^{q}[1 - \Delta t \gamma n_{i,j}^{q}] + \Delta t \beta n_{i,j}^{q} \\ c_{i,j}^{q+1} &= c_{i,j}^{q}[1 - \Delta t \eta n_{i,j}^{q}] \end{aligned} \tag{4.18}$$

where

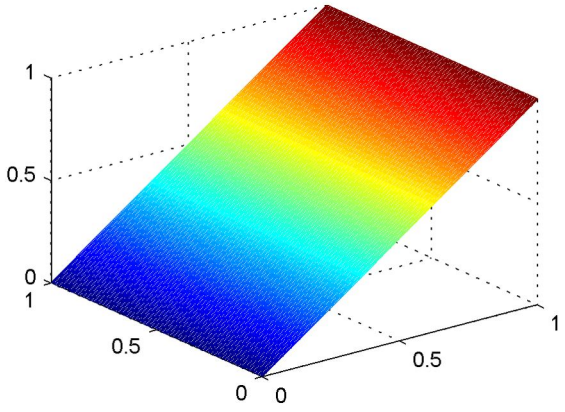

Figure 4.3: Initial TAF concentration in the domain

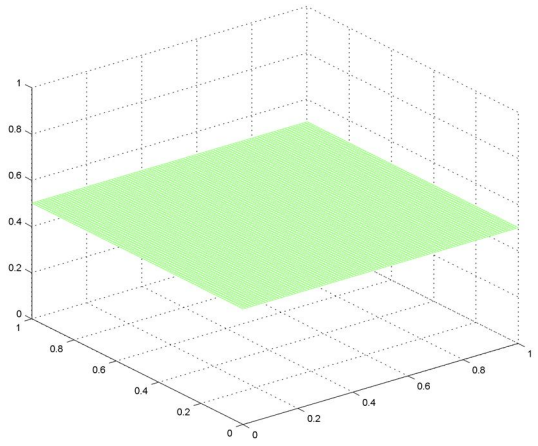

Figure 4.4: Initial fibronectin concentration in the domain

Table 4.1: Parameter values used in the simulation

Parameter description	Symbol	Value	Reference
Random motility coefficient of EC in nondimensionalized equation	D	0.00035	[4]
Chemotactic coefficient in nondimensionalized equation	χ_0	0.16*	[4]
Coefficient in the chemotactic function	δ	0.6	[97]
Haptotactic coefficient in nondimensionalized equation	ϕ	0.34	[4]
Coefficient for uptake of TAF in nondimensionalized equation	η	0.1	[4]
Coefficient for production of fibronectin in nondimensionalized equation	β	0.01*	[4]
Coefficient for uptake of fibronectin in nondimensionalized equation	γ	0.1	[4]
Matrix density reference value	ρ_0	0.35	[6]
Constant in the matrix density function	σ	0.2	
Constant in initial EC density distribution	ϵ_3	0.0025	

* Parameters with an asterisk have been adapted for this model.

$$
\begin{aligned}
P_0 &= 1 - \tfrac{4\Delta tD}{h^2} - Z(\rho)[\tfrac{\Delta t\chi_0(1+\delta c^q_{i,j})}{h^2}(c^q_{i+1,j} + c^q_{i-1,j} - 4c^q_{i,j} + c^q_{i,j+1} + c^q_{i,j-1}) \\
&- \tfrac{\Delta t\phi}{h^2}(f^q_{i+1,j} + f^q_{i-1,j} - 4f^q_{i,j} + f^q_{i,j+1} + f^q_{i,j-1})] \\
P_1 &= \tfrac{\Delta tD}{h^2} - \tfrac{Z(\rho)\Delta t}{4h^2}[\chi_0(1+\delta c^q_{i+1,j})(c^q_{i+1,j} - c^q_{i-1,j}) + \phi(f^q_{i+1,j} - f^q_{i-1,j})] \\
P_2 &= \tfrac{\Delta tD}{h^2} + \tfrac{Z(\rho)\Delta t}{4h^2}[\chi_0(1+\delta c^q_{i-1,j})(c^q_{i+1,j} - c^q_{i-1,j}) + \phi(f^q_{i+1,j} - f^q_{i-1,j})] \\
P_3 &= \tfrac{\Delta tD}{h^2} - \tfrac{Z(\rho)\Delta t}{4h^2}[\chi_0(1+\delta c^q_{i,j+1})(c^q_{i,j+1} - c^q_{i,j-1}) + \phi(f^q_{i,j+1} - f^q_{i,j-1})] \\
P_4 &= \tfrac{\Delta tD}{h^2} + \tfrac{Z(\rho)\Delta t}{4h^2}[\chi_0(1+\delta c^q_{i,j-1})(c^q_{i,j+1} - c^q_{i,j-1}) + \phi(f^q_{i,j+1} - f^q_{i,j-1})]
\end{aligned}
\tag{4.19}
$$

h is the grid size, which is considered to be equal in both x and y directions, and q specifies the time step.

The solution of the discretized equations is performed in an iterative process. Starting with the initial values for EC density, TAF and fibronectin concentrations, a new value is

obtained in each time step. This value is used as an updated value for the next time step, and the solution continues until the specified time.

4.3 Implementation of MDE Model in the Continuous Model of Angiogenesis

The above model was a development on the model presented by Anderson and Chaplain [4] and used as the base of capillary network generation in some subsequent works [96, 63, 15, 107]. In this model, a general equation was considered for EC density, and two equations were assumed for TAF and fibronectin concentration. Another important parameter, which was not assumed in the previous continuous models, is the secretion of MDE by ECs and which degrades the ECM locally to open the path for EC migration. Although in a more recent work [63] another equation has been assumed for the MDE in the discrete model and coupled with other equations, no attention has been paid to the continuous model. Since the continuous model of angiogenesis is the basis of the discrete model, consideration of its mathematical behavior is important in the quality of the capillary network generated by the discrete model. Here, the MDE has been applied on the continuous model to see its effect on the continuous model and also the effect of different model parameters on the solution and results.

The governing set of equations for the continuous model of angiogenesis was presented before in this chapter. This section introduces a new parameter, m, which is a concentration of MDE.

MDE is representative of many proteases secreted by ECs. MDE is considered to be a chemical agent produced by ECs, diffused through the ECM, and subject to a constant decay rate. The governing equation for MDE concentration should involve appropriate terms corresponding to its production, diffusion, and decay. An equation for the discrete model presented by McDougall *et al.* has been changed here for the continuous model [63]:

$$\frac{\partial m}{\partial t} = \alpha n + \epsilon \nabla^2 m - \nu m \tag{4.20}$$

where m is MDE concentration, α is the production rate of MDE, ν is the decay rate, and ϵ is the diffusion coefficient of MDE.

It should be mentioned that the role of MDE is to degrade ECM locally and open a corridor for EC transport. This effect is modeled by the action of MDE on the fibronectin.

As MDE molecules act on the fibronectin, the fibronectin molecules are degraded, and a gradient of fibronectin is established in the domain. In the case of MDE action, degradation of fibronectin enhances the gradient in the fibronectin domain and acts as an additional stimulus for haptotactic movement of the ECs.

In the continuous model of angiogenesis without MDE action, both a constant production rate and a constant decay rate have been considered for fibronectin. These rates are proportional to the EC density. To include the effect of MDE in the equations, a constant production rate of β is assumed for fibronectin, a rate proportional to the EC density; however, here, the degradation of fibronectin is assumed to be proportional to the MDE concentration. To include this effect, the equation for fibronectin concentration is modified to show its reduction in the presence of MDE [63, 97].

$$\frac{\partial f}{\partial t} = \beta n - \zeta m f \tag{4.21}$$

The final set of equations can now be written:

$$\begin{aligned}
\frac{\partial n}{\partial t} &= D\nabla^2 n - Z(\rho)\nabla.[\chi_0(1+\delta c)n\nabla c + \phi n \nabla f] \\
\frac{\partial c}{\partial t} &= -\eta n c \\
\frac{\partial f}{\partial t} &= \beta n - \zeta m f \\
\frac{\partial m}{\partial t} &= \alpha n + \epsilon \nabla^2 m - \nu m
\end{aligned} \tag{4.22}$$

The additional values used in this model are also obtained from the previous work in this context [97] and shown in Table 4.2. The parameters with an asterisk have been adapted based on the initial and boundary conditions for this model.

An initial profile should be considered for the MDE in the domain as shown in Figure 4.5. The profile used in this work is in accordance with the initial EC density distribution.

The discretization of the above equations with MDE is like that in the previous model except for a slight difference in the equation for fibronectin concentration and also the additional equation for MDE density. Using a central difference discretization scheme of

Table 4.2: Additional parameter values in the model with MDE

Parameter description	Symbol	Value	Reference
Production rate of MDE	α	1^*	[97]
Diffusion coefficient of MDE	ϵ	0.001^*	[97]
Decay rate of MDE	ν	3	[97]
Decay rate of fibronectin due to MDE	ζ	0.25^*	[97]

* Parameters with an asterisk have been adapted for this model.

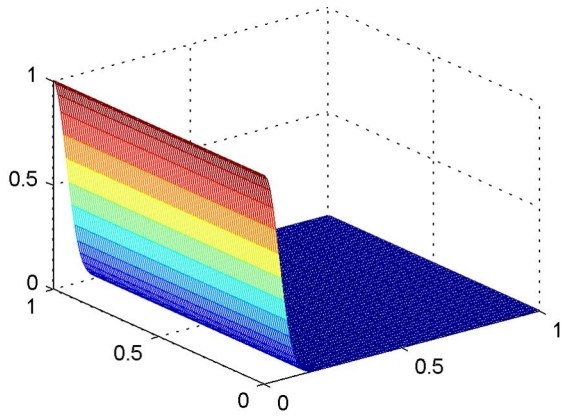

Figure 4.5: Initial distribution of MDE in the domain

finite difference for the fibronectin concentration equation and also for additional equation for MDE produces

$$\begin{aligned} f_{i,j}^{q+1} &= f_{i,j}^{q}(1-\Delta t\zeta m_{i,j}^{q}) + \beta n_{i,j}^{q} \\ m_{i,j}^{q+1} &= m_{i,j}^{q}(1-\tfrac{4\epsilon\Delta t}{h^2}-\nu\Delta t) + \tfrac{\Delta t\epsilon}{h^2}(m_{i+1,j}^{q}+m_{i-1,j}^{q}+m_{i,j+1}^{q}+m_{i,j-1}^{q}) + \alpha\Delta t n_{i,j}^{q} \end{aligned} \tag{4.23}$$

The above equations are solved by a method similar to the previously described iterative method.

4.4 Discrete Mathematical Model of Angiogenesis

The following equation represents the EC density distribution in the continuous model:

$$n_{i,j}^{q+1} = n_{i,j}^{q} P_0 + n_{i+1,j}^{q} P_1 + n_{i-1,j}^{q} P_2 + n_{i,j+1}^{q} P_3 + n_{i,j-1}^{q} P_4$$

In a discrete model of angiogenesis, the governing equations are the same except that the values of P_0, P_1 , P_2 , P_3 and P_4 are interpreted as the probability of an EC staying on its current location, moving left, right, up or down, respectively. Each of the P_0 to P_4 coefficients in the above equation is composed of three parts. As a case in point, for P_2,

$$P_2 = \frac{\Delta t D}{h^2} + \frac{Z(\rho)\Delta t}{4h^2}[\chi_0(1 + \delta c_{i-1,j}^{q})(c_{i+1,j}^{q} - c_{i-1,j}^{q}) + \phi(f_{i+1,j}^{q} - f_{i-1,j}^{q})]$$

P_2 is an estimation of the probability of an individual EC to move to the right, i.e., toward the tumor. The first term is the random motility contribution to this movement. As can be seen in the equations for other Ps, this term is identical in all of them. The coefficient D is representative of the diffusion that is a random movement mechanism of ECs. The second term, which contains the local gradient of the TAF concentration, is representative of the chemotaxis contribution, and the third term, which contains the local gradient of fibronectin, states the haptotactic contribution to the final movement probability.

To start the solution in a discrete model, we assume some individual ECs to be located on the parent vessel (instead of the initial distribution of EC density in the continuous model), and occupying certain grid points. The discrete model is based on the assumption that the movement of the EC at the tip of the sprout coordinates the path along which the capillary moves in the domain.

When an EC is in grid position (*i, j*), and the probability-based movement algorithm makes it move to right, it will occupy the grid point (*i+1, j*) too. This kind of discrete approach, coupled to our interpretation of the P values as some probabilities, makes this method a promising tool for investigating and visualizing the movement of ECs toward the tumor.

This approach has considerable complexity and also requires consideration of natural behaviors of ECs like branching and anastomosis during their migration. These assumptions also add complexity to the coding procedure. The overall algorithm of a discrete model may be stated as below:

1. Set initial parameters of the problem.

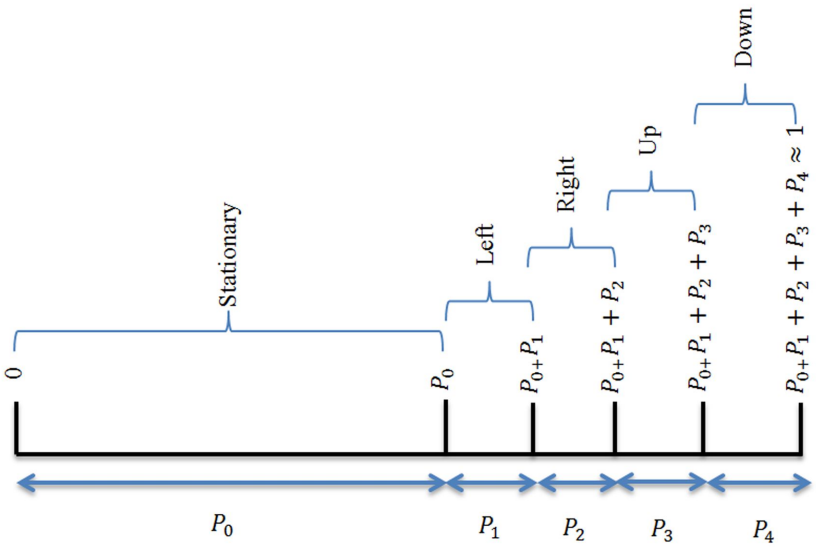

Figure 4.6: The spectrum of probability distribution in discrete model of angiogenesis

2. Calculate the probability of movement of each individual EC.
3. Keep each EC in its location or move it right, left, up or down according to the value of probabilities.
4. Check for anastomosis (tip to sprout or tip to tip).
5. If anastomosis is present, just one of the two ECs continues its movement.
6. Check for branching.
7. If branching is present, a new EC is added to the list of ECs for the next step.
8. Go to step 2.

The calculation of probability for each time step involves the solution of the equation for governing five coefficients: P_0, P_1 , P_2 , P_3 and P_4. As explained, these coefficients are treated as the probability to remain stationary, move left, right, up and down, respectively. These values are used in a spectrum of probability to determine the final movement direction. This spectrum type interpretation of the probabilities is shown in Figure 4.6.

To calculate the probability of movement, a random number between $[0, 1]$ is generated. Depending on its value, it falls in a range in the above spectrum, and EC movement is determined according to the corresponding range.

As mentioned, these values are not probabilities in nature, but here are interpreted as values related to movement probabilities. The summation of movement probabilities of ECs in all directions in a time step should be equal to unity and none of the probability values should be negative; however, in some time steps, the values of some Ps are negative, and their summation is a value near unity. This issue occurs because, as stated, these values are not probabilities but are interpreted values proportional to probabilities. It should be mentioned that no specific problem arises from this issue.

The movement of an EC in any direction is possible; however, this study ignores backward movement of ECs, i.e., setting P_1 equal to zero. Since the probability values have been normalized to the range of $[0, 1]$, the absolute value of P_1 is divided among other movement probabilities.

The branching probability is determined according to a qualitative distribution that gives the value of zero for the regions near the parent vessel ($x < 0.25$). As the distance from the parent vessel increases, and capillaries get closer to the tumor, this value increases to 0.2 for $0.25 < x < 0.45$, 0.3 for $0.45 < x < 0.6$, 0.4 for $0.6 < x < 0.68$, and the value of 1 for $x > 0.68$ [4].

4.5 Implementation of MDE Model in the Discrete Model of Angiogenesis

The system of equations for the case with MDE considerations in a continuous framework was presented before. Similarly, in the discrete model, MDE is included in the model by adding an equation for MDE production, diffusion and uptake.

$$\begin{aligned}
\frac{\partial n}{\partial t} &= D\nabla^2 n - Z(\rho)\nabla.[\chi_0(1+\delta c)n\nabla c + \phi n \nabla f] \\
\frac{\partial c}{\partial t} &= -\eta n c \\
\frac{\partial f}{\partial t} &= \beta n - \zeta m f \\
\frac{\partial m}{\partial t} &= \alpha n + \epsilon \nabla^2 m - \nu m
\end{aligned} \tag{4.24}$$

The role of the additional equation is just to exhibit the role of MDE in the probability values in the discretized form of the first equation.

The main difference between the MDE effect in the discrete model developed in this study and that in the previous models [63, 97] is in local behavior. In the previous models, a local production and diffusion of MDE is considered for ECs, i.e., a Boolean value has been considered in the equations to show the presence of ECs at specific grid points. In the model developed in this work, the production of MDE has not been modeled locally; that is, production of MDE and degradation of fibronectin are not in specific grid points determined by Boolean values, rather they take place in the region determined by the EC aggregate. In fact, the physical effects of the continuous model are used directly in the discrete model. This approach establishes a better relationship between the continuous and discrete models, and the behavior of the discrete model can easily be predicted from the continuous model.

4.6 Results

Results are presented in four distinct sections corresponding to the four modeling frameworks for continuous and discrete models mentioned in this work. Each section presents two sets of results. First, variation of the solution parameters is shown during the solution for a matrix density of 0.15. Second, results of the solution in the final time step are shown for matrix densities of 0.25, 0.35, 0.45 and 0.55. The overall trend of the solution parameters in all matrix densities is similar, so no solution details for matrix densities greater than 0.15 are shown. It should be noted that $T = 1$ is equal to 1.5 days, $T = 2$ is equal to 3 days, and so on.

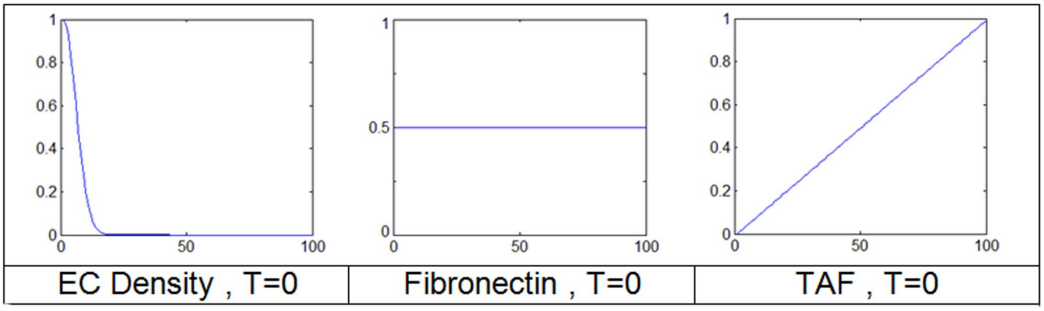

Figure 4.7: Cross sections from initial distribution of EC density, fibronectin and TAF in the domain

4.6.1 Continuous Model of Angiogenesis without MDE Consideration

Results for the continuous model without MDE consideration are presented in this section. The initial condition of the EC density, fibronectin and TAF has been introduced before and is plotted in the cross section again in Figure 4.7. The variations of these profiles during the iterations have been plotted in Figure 4.8 for the matrix density of 0.15. The distance between parent vessel and tumor has been divided into 100 intervals.

Two main stimuli for EC movement and their corresponding gradients are seen clearly in Figure 4.8. The curvature created in the fibronectin profile is due to production and decay of this agent. As can be seen, a very low gradient of fibronectin reduces the haptotaxis effect. The reduction in the apex of EC density during the solution is due to the propensity of ECs to diffuse in the domain. The change in the distribution of the TAF is so small that it cannot be observed at this scale. It should be noted that for fibronectin, the change is so small that the limits of the diagram have been reduced to capture this change.

EC density distribution is shown for some other values of matrix densities in Figure 4.9. In these cases, evolution of the EC density profile during the solution is shown.

As observable in Figure 4.9, the function of matrix density is imposed on the model to get the maximum migration speed in a matrix density of around 0.35.

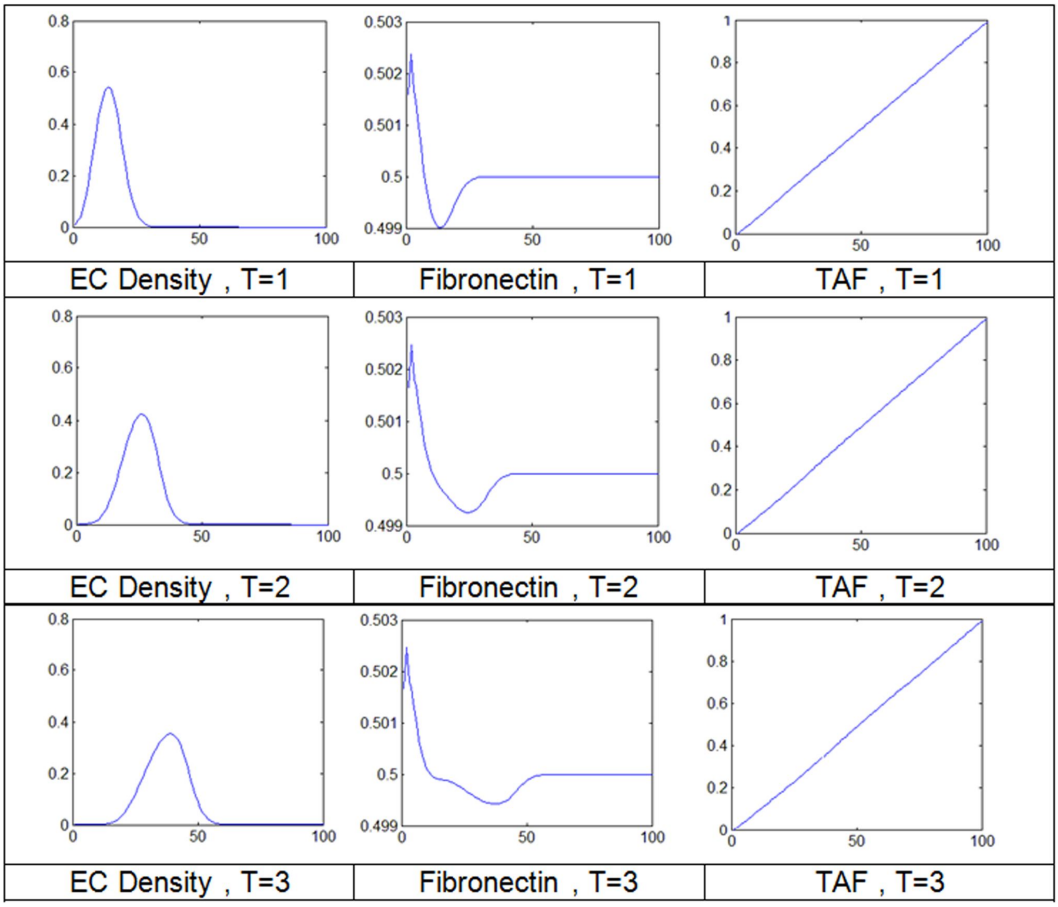

Figure 4.8: Cross sections from distribution of EC density, fibronectin and TAF in the domain during the solution

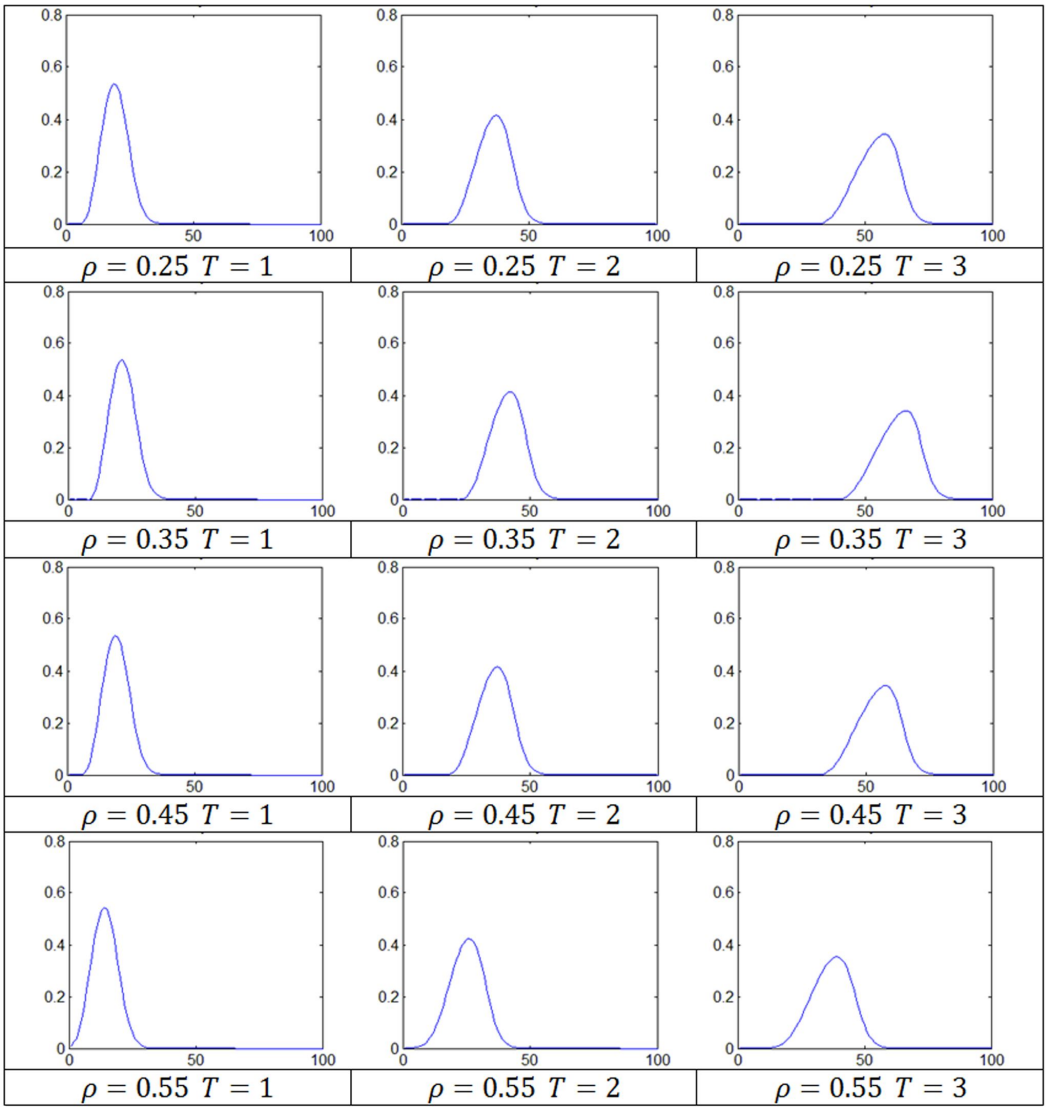

Figure 4.9: Distribution of EC density for matrix density values of 0.25, 0.35, 0.45 and 0.55 for the case without MDE consideration

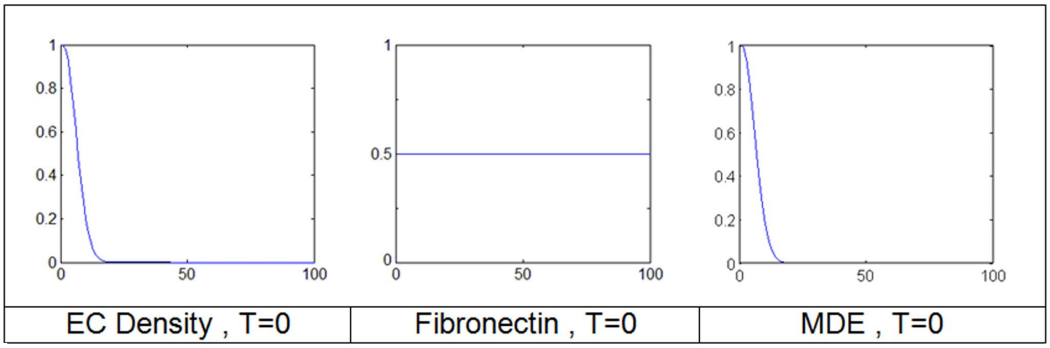

Figure 4.10: Cross sections from initial distribution of EC density, fibronectin and MDE in the domain

4.6.2 Continuous Model of Angiogenesis with MDE Consideration

Results for the continuous model with MDE consideration are presented in this section. Since the TAF profile does not change notably during the solution, in the case of the continuous model with MDE, the initial condition of the EC density, fibronectin and MDE has been plotted in the cross section in Figure 4.10. The variations of these profiles during the iterations have been plotted in Figure 4.11 for the matrix density of 0.15. The distance between parent vessel and tumor has been divided into 100 intervals.

MDE action on fibronectin provides a gradient of fibronectin that makes the ECs move faster. MDE is produced by ECs, so its distribution moves with the EC aggregate. In the case of fibronectin degradation, haptotaxis has a notable role in the EC movement.

EC density distribution is shown for other values of matrix densities in Figure 4.12. In these cases, evolution of the EC density profile during the solution is shown.

As observable in Figure 4.12, as in the case without MDE action in the model, the function of matrix density is imposed on the model to get the maximum migration speed in a matrix density of around 0.35.

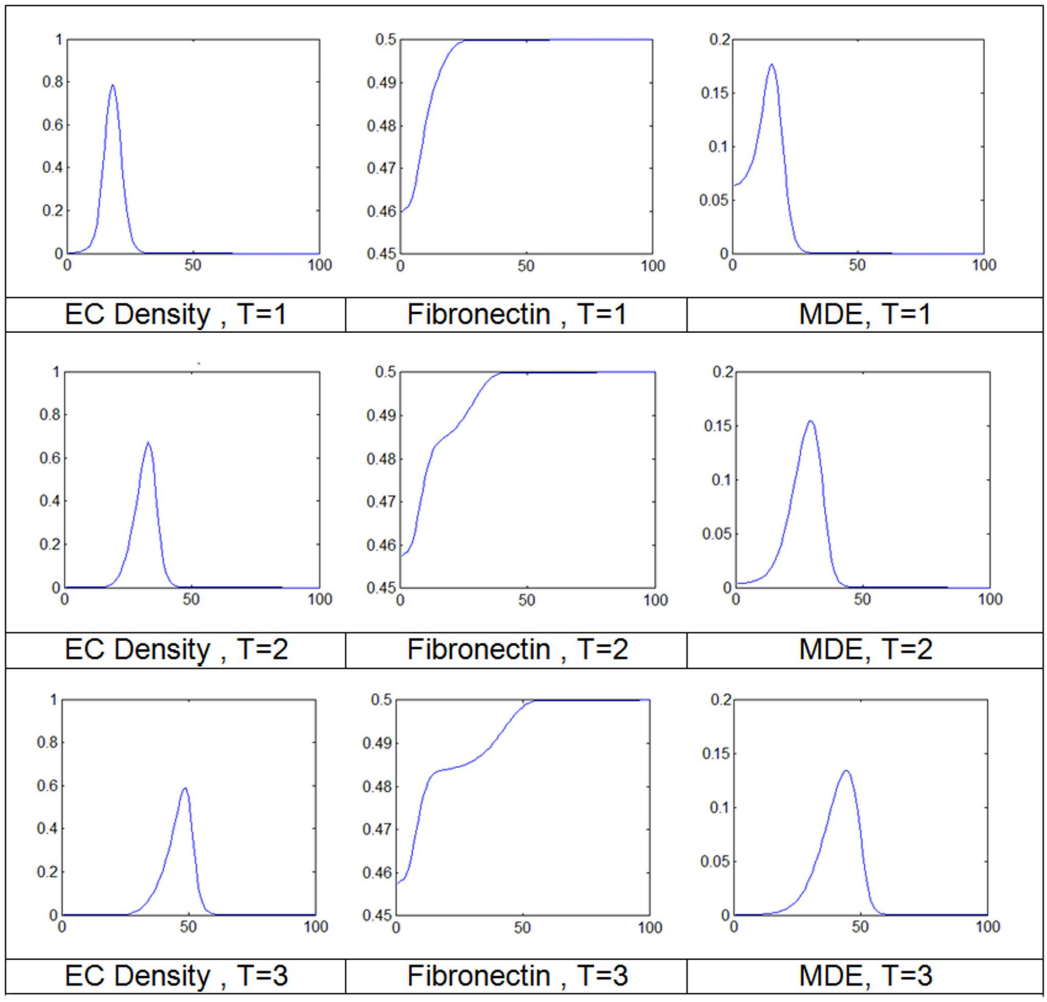

Figure 4.11: Cross sections from distribution of EC density, fibronectin and MDE in the domain during the solution

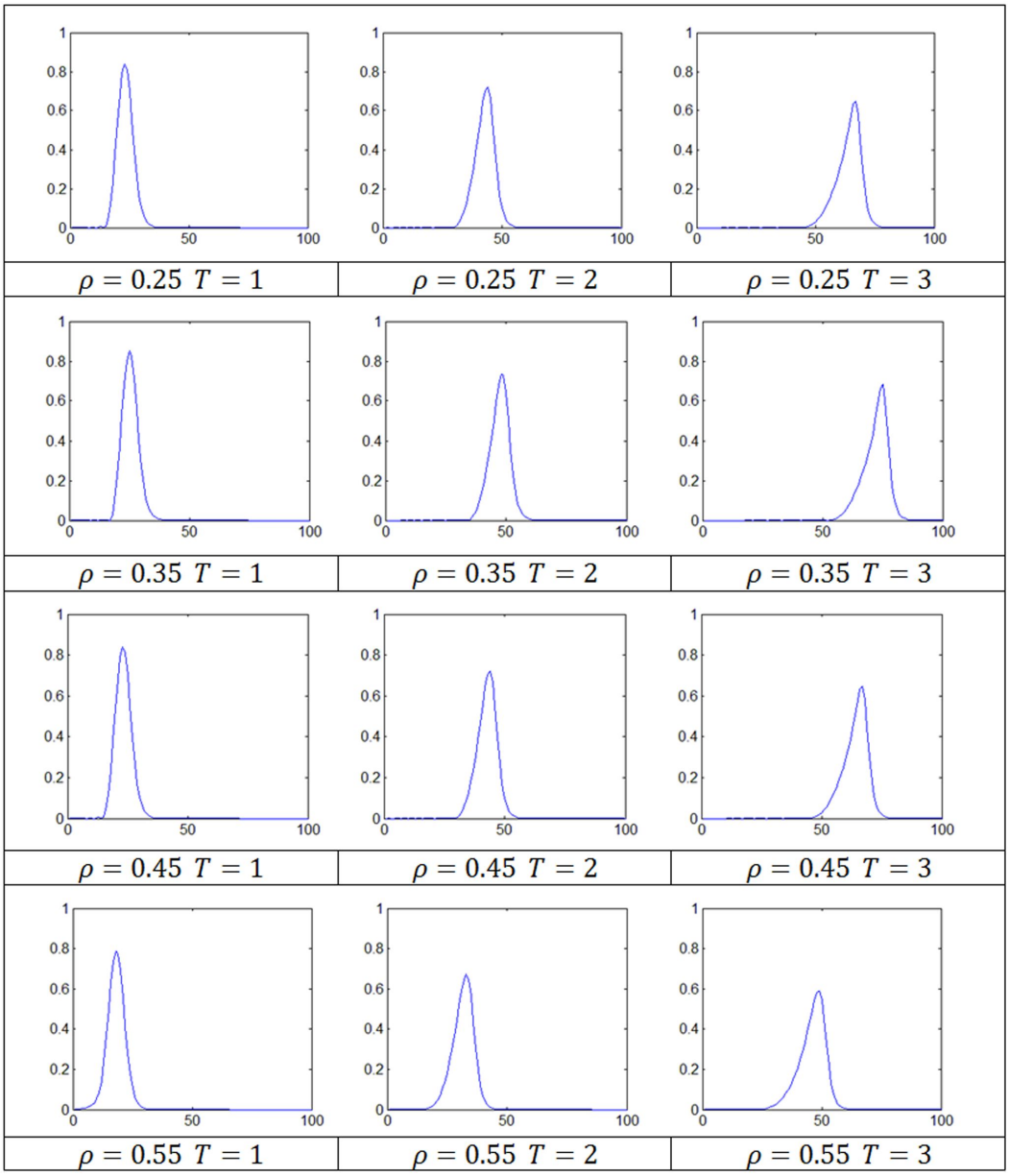

Figure 4.12: Distribution of EC density for matrix density values of 0.25, 0.35, 0.45 and 0.55 for the case with MDE consideration

4.6.3 Discrete Model of Angiogenesis without MDE Consideration

The continuous model of angiogenesis is the basis for the discrete model. The output in the discrete model is a capillary network, based on the values of Ps, which are interpreted as the probability of movement in different directions. In results presented for the discrete model, the main focus is on the capillary network and probabilities. Other parameters such as EC density distribution, fibronectin degradation and distribution, and TAF distribution are similar to those in the counterpart continuous model. Results for the discrete model without MDE are presented in this section. Initial conditions of EC density, fibronectin and TAF are also similar to those in the continuous model. The capillary network and the probabilities to move right (toward the tumor) and remain stationary for a matrix density of 0.15 are shown in Figure 4.13.

As can be observed in Figure 4.13, the probability that ECs will remain stationary decreases as capillaries move toward the tumor, and the probability of that moving right (toward the tumor) increases. The bump-like shapes in the probabilities represent the effect of fibronectin decay and production, which locally increases the probability of moving to the right and decreases the probability of ECs remaining stationary. The movement probabilities and generated capillary networks without MDE effect consideration for other matrix densities are shown for $T = 4$ in Figure 4.14.

In the results presented in Figure 4.14, the probability of ECs remaining stationary decreases as capillaries move toward the tumor, and the probability of them moving toward the tumor increases. Increasing the matrix density up to 0.35 increases migration speed. This can be concluded from the range of probabilities in each matrix density and the resulting capillary network. After a matrix density of 0.35, increasing matrix density decreases migration speed. The value of the probability of ECs moving back is set to zero, and the values to move up and down are similar and change slightly during EC movement.

4.6.4 Discrete Model of Angiogenesis with MDE Consideration

Results for a discrete model with MDE are presented in this section. Initial conditions of EC density, fibronectin, TAF, and MDE are similar to those in the continuous model with MDE assumption. A capillary network and movement probabilities for a matrix density of 0.15 are shown in Figure 4.15.

As can be seen in Figure 4.15, the probability that ECs will remain stationary decreases as capillaries move toward the tumor, and the probability of that moving right (toward the

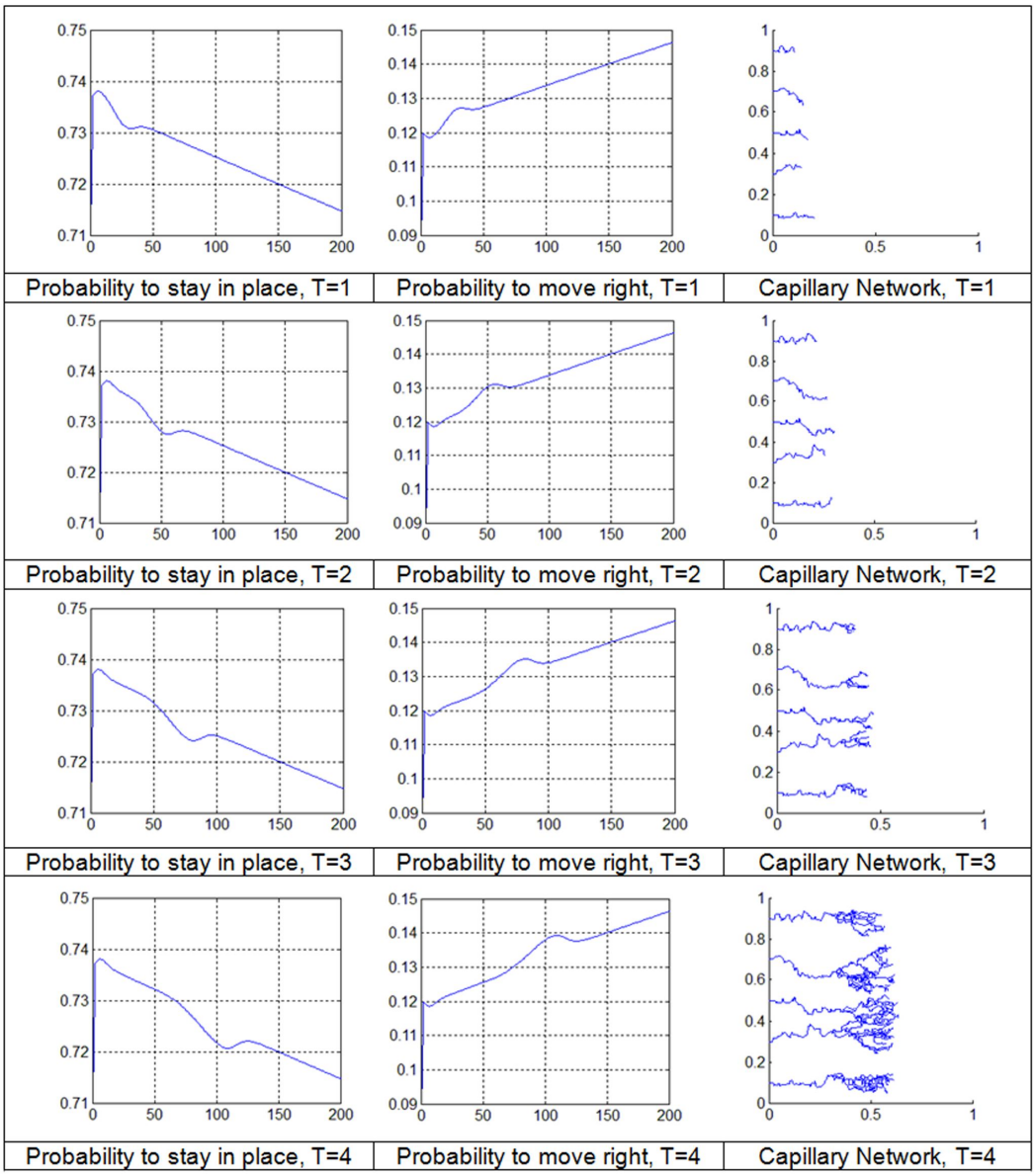

Figure 4.13: Movement probabilities and resulting capillary network for matrix density of 0.15 without MDE effect

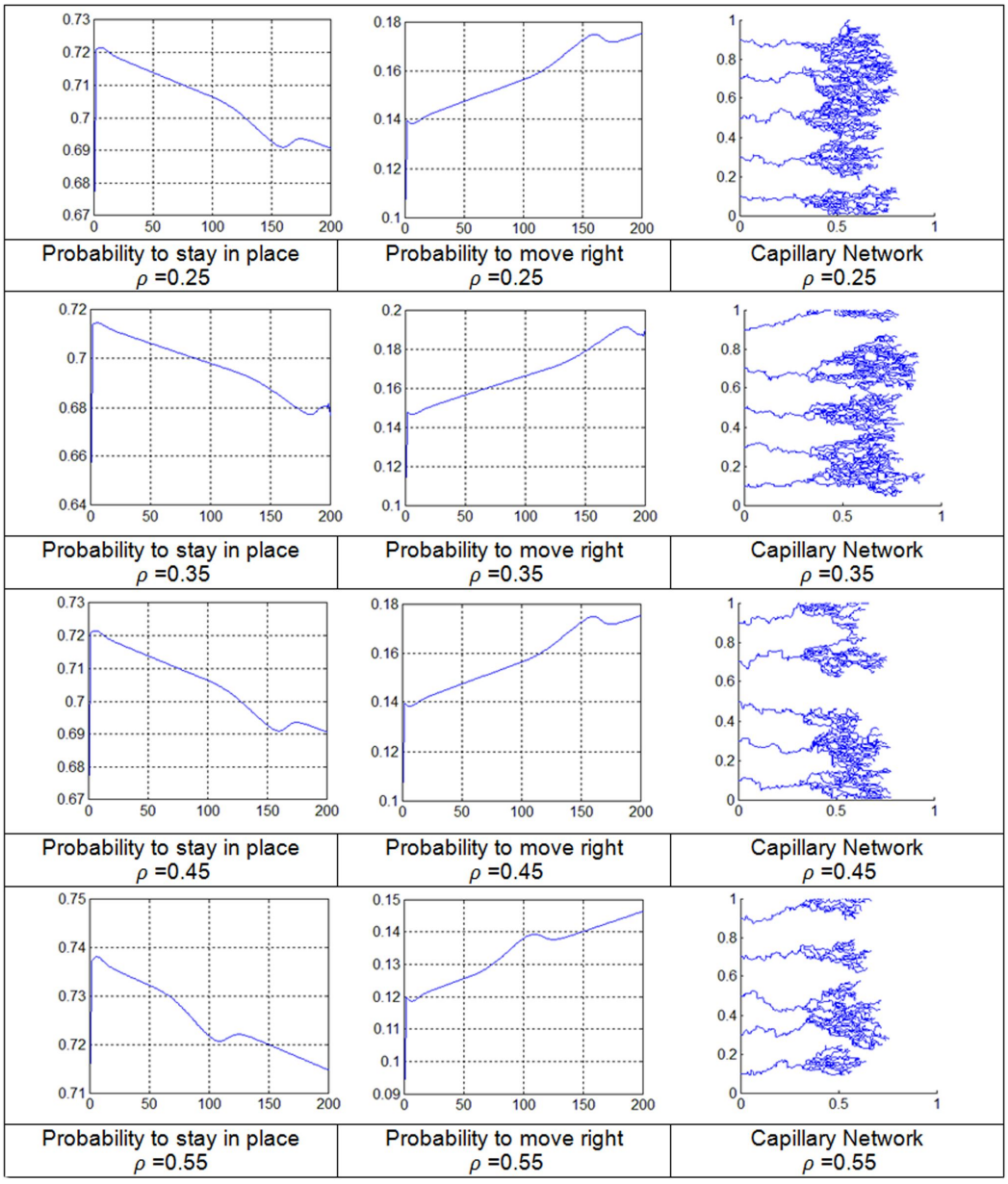

Figure 4.14: Movement probabilities and resulting capillary network for matrix densities of 0.25, 0.35, 0.45 and 0.55 in T=4

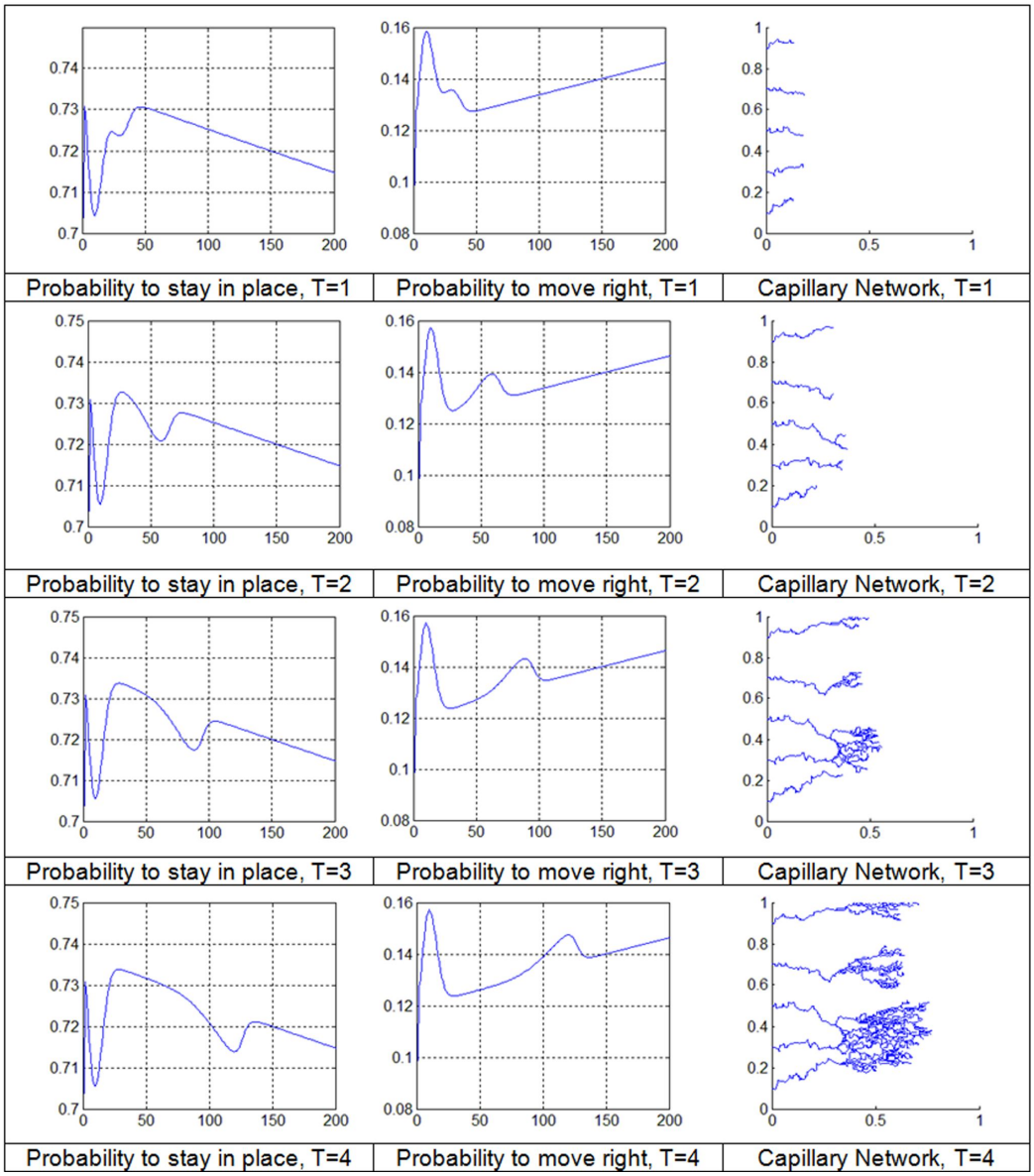

Figure 4.15: Movement probabilities and resulting capillary network for matrix density of 0.15 with MDE effect

tumor) increases. The bump-like shapes in the probabilities represent the degradation of fibronectin and its production, which locally increases the probability to move right and decreases the probability to remain stationary.

The movement probabilities and generated capillary networks with MDE effect consideration for other matrix densities are shown in $T = 4$ in Figure 4.16.

In the results presented in Figure 4.16, the probability of ECs remaining stationary decreases as capillaries move toward the tumor, and the probability of moving toward the tumor increases. Increasing the matrix density up to 0.35 increases migration speed, which can be concluded from the range of probabilities in each matrix density and the resulting capillary network. The value of probability to move back is set to zero, and the values to move up and down are similar and change slightly during EC movement. The values of moving up and down can be estimated by subtracting the sum of probability values to remain stationary and to the right from unity.

4.7 Discussion

In the continuous model of angiogenesis without consideration of MDE, the movement of the EC aggregate is mainly due to random movement and chemotaxis. In this case, due to very low gradients in the fibronectin profile, it is impossible to establish a movement stimulus for the ECs. As can be seen in Figure 4.8, the curves in the fibronectin profiles are produced as a result of fibronectin production and uptake, which do not provide strong movement potential. The profile of TAF is not changed notably during solution, and an almost constant TAF gradient is assumed throughout the domain. During the solution, the EC distribution peak is lowered and decreases from the value of unity at the beginning of the solution to a value of less than 0.4 in $T = 3$ (600 iterations). The EC density cannot be changed during the solution since the total amount of ECs must be conserved. As shown in Figure 4.8, the bell shape distribution of ECs in $T = 2$ and $T = 3$ is expanded at its base, and this conserves the number of ECs, i.e., the total area under this curve remains constant.

For the other values of matrix density in Figure 4.9, the results show that increasing the matrix density from 0.15 to 0.25 makes ECs move faster. Faster movement is also observed in a matrix density of 0.35; however, increasing the matrix density to 0.45 and 0.55 decreases migration speed. This issue occurs due to the function introduced before as $Z(\rho)$ to implement the effect of matrix density in migration speed.

The effect of MDE in the model is observed in the fibronectin profile in Figure 4.11.

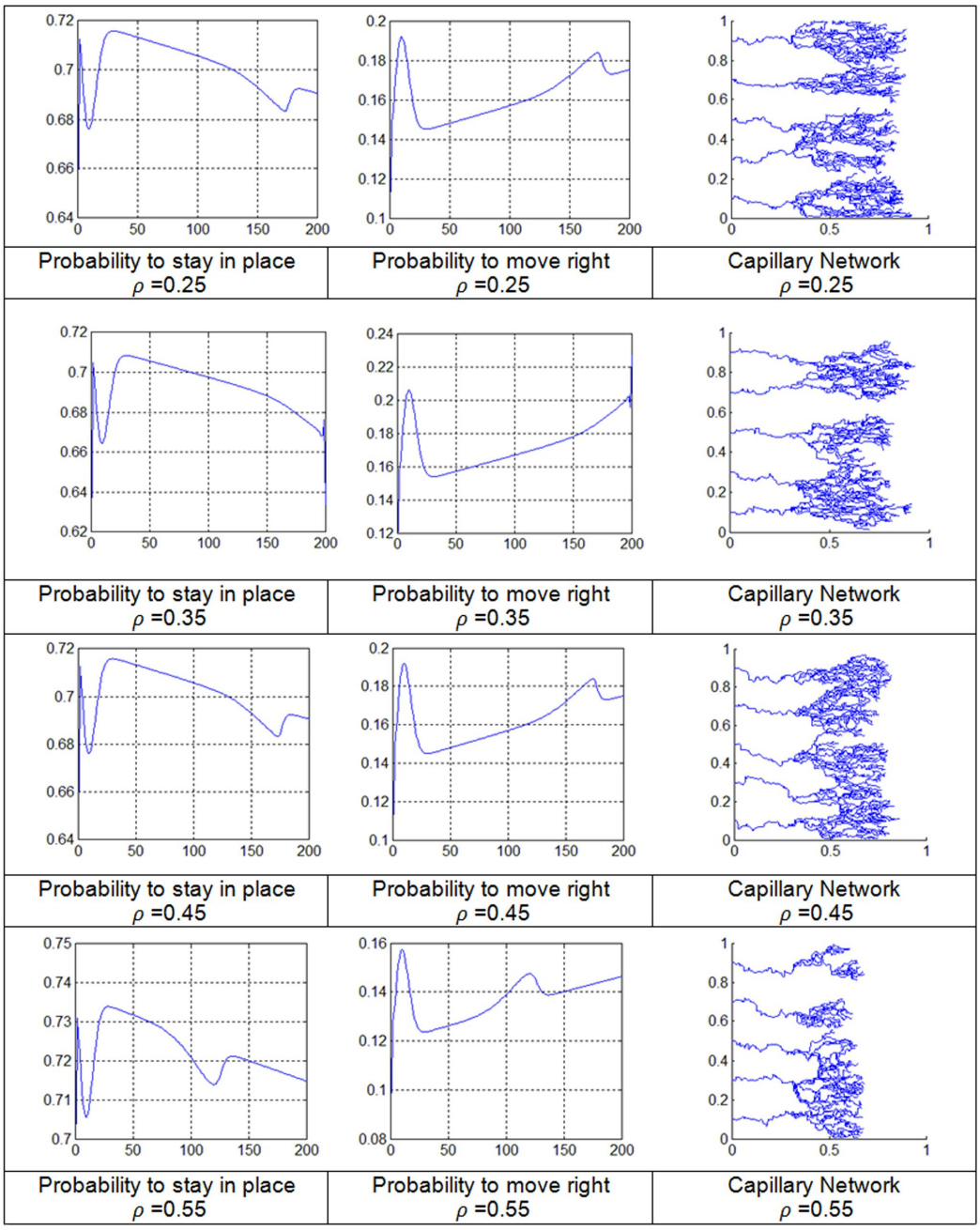

Figure 4.16: Movement probabilities and resulting capillary network for matrix densities of 0.25, 0.35, 0.45 and 0.55 in T=4 with consideration of MDE

MDE degrades the fibronectin, creating a gradient in the fibronectin profile. This gradient enhances the haptotactic movement potential and accelerates the ECs' movement. Since the fibronectin gradient is stronger as the ECs aggregate downwards, the EC density is squeezed, creating higher peaks during the solution.

EC movement in the other matrix densities shown in Figure 4.12 is like the case without MDE consideration but with a slight change in migration speed. ECs move faster with MDE consideration than without it because the established gradient in the fibronectin profile gives the ECs a higher migration speed. The highest migration speed is observed in matrix densities of around 0.35, a finding similar to the case without MDE. In all cases, assumption of MDE provides a higher peak in EC distribution, which, as mentioned before, is due to the fibronectin gradient.

In the discrete model of angiogenesis, the values of Ps are interpreted as the probability of movement. The portion of each P value in the total movement probability determines the capillary network configuration. Since the continuous model is the basis for the discrete model, without MDE, haptotaxis is not expected to exhibit a notable effect. The formation of a capillary network for a matrix density of 0.15 is shown in Figure 4.13. The probability of ECs remaining stationary or moving right is also shown each time.

One of the main advantages of the current model is its physical probability distribution, seen in Figure 4.13. In the previous discrete models, the probability to move toward a tumor is decreased as a consequence of unrealistic assumptions about fibronectin and TAF distribution.

In contrast, this work has modified the initial distribution of fibronectin and TAF in the domain according to physiological observations about fibronectin and mathematical analysis of TAF distribution, respectively. This study also assumes that the role of chemotaxis increases linearly as capillaries move toward the tumor. These assumptions have helped to establish a physical distribution of probabilities in the domain. As can be seen in Figure 4.13, when ECs move toward the tumor, the probability of their moving right increases, and the probability of their remaining stationary decreases. There is a small bump in the probability distribution profile that moves in the direction of the tumor. This bump is almost coincident with the tip cells of the capillary network. The bump shows the effect of fibronectin degradation in the domain. As discussed, the effect of fibronectin degradation in the continuous model was slight. Here, a small increase in the probability to move right is produced due to this effect. In Figure 4.13, in $T = 4$, the ECs are almost half way to the tumor. The capillaries were not allowed to continue their motion to provide a means of comparing migration speed, so this study presents the resulting capillary network in $T = 4$ for matrix densities of 0.25, 0.35, 0.45 and 0.55 in Figure 4.14.

Certain points should be noted about Figure 4.14. First, increasing the matrix density to 0.25 increases the range of probabilities, thereby providing faster migration of ECs in the domain. At the same time, the probability of remaining stationary decreases, which is in agreement with the increase probability of moving right. At a matrix density of 0.35, the probability to move right increases further and is at maximum. At matrix densities of 0.45 and 0.55, the probability of moving right lessens. This issue corresponds to migration speed, and, as seen in Figure 4.14, the maximum range of probability of movement right is at a matrix density of 0.35. The capillary network also propagates more at this matrix density. As discussed, we expected that at low matrix densities, capillaries would not establish good connections with matrix elements. Moreover, by increasing matrix density, it was expected that the high density of the matrix would inhibit angiogenesis. This issue has been implemented by the function $Z(\rho)$ in the main equation. This function regulates the effect of haptotaxis and chemotaxis as a function of matrix density. The second point worth noting is the small bump still seen in these results in Figure 4.14. It is again the effect of fibronectin decay and moves with ECs in the solution domain.

The most interesting part of this study is the case of the discrete model when MDE is considered. The growing capillaries for the matrix density of 0.15 are shown in Figure 4.15 four times. This figure again shows the increasing trend of probability to move right and the decreasing trend of probability to remain stationary. In comparison to the probability distribution for the case without MDE in a matrix density of 0.15, considering of MDE does not change the overall range of probabilities; however, MDE consideration affects the probability distributions. Two bumps are seen in the probability distribution profiles: the bump near the parent vessel, due to the initial concentration of MDE, and the bump due to fibronectin degradation, caused by the movement of ECs in the domain. It should be noted that in this case, the bump is bigger than in the case without MDE, meaning that fibronectin degradation has a more pronounced effect in this case. Moreover, compared to the similar case without MDE, the more ECs developed and migrated faster. The higher migration speed in this case is the result of the two bumps seen in Figure 4.15. The bumps locally increase the probability of tip cells moving right, and this will lead to higher migration speed.

For other values of matrix density shown in Figure 4.16, we have made observations similar to those in the case without MDE. The two bumps help the probabilities to push the ECs more toward the tumor. Also the maximum migration speed is observed in the matrix density of 0.35 and is imposed in the equations by the function $Z(\rho)$.

4.8 Conclusion

This chapter presents modifications of some features of the previously presented continuous and discrete models of angiogenesis. These modifications are on the initial distribution of fibronectin and TAF in the domain and also in the interpretation of the effect of MDE in the continuous and discrete model. MDE was implemented on the continuous model for the first time in this study. Additionally a function for matrix density effect allowed the effect to be implemented in the equations and solution. One of the main advantages of this work is the realistic probability distribution in the domain. The capillaries should accelerate as they move toward the tumor, meaning that probability to move right should increase as the capillaries move toward the tumor. Changing the function of the chemotactic coefficient and also real initial conditions leads to realistic probability distribution in the domain, which shows an increased probability to move right as capillaries migrate toward the tumor. Fibronectin degradation is clearly shown to establish haptotactic movement, and in the absence of MDE, the expected haptotactic movement decreases.

Chapter 5

Capillary Network Flow in Solid Tumor Microvasculature

5.1 Introduction

Although heart and blood vessel diseases were the main causes of death for many years, more than 12 million new cancer diagnoses were reported in 2011, making it the new leading cause of death. More than 85% of cancers involve solid tumors; therefore, better understanding of tumor formation is very important in cancer therapy [43]. In terms of modeling, solid tumor growth can be characterized in two different phases: the avascular and vascular. Relying only on diffusion from nearby vessels to supply oxygen and nutrients, the first phase usually continues until a tumor reaches the diameter of a few millimeters [30]. To grow further, a solid tumor needs its own blood supply, in the form of, and supplied by, a capillary network.

The main barrier to successful drug delivery to solid tumors is their abnormal and complicated vasculature [102]. The high interstitial pressure and low intravascular pressure near the tumor affect drug transport, causing slow flow through the tissue and low filtration of drugs from vessels. Solid tumor simulation results are used to predict how therapeutic drugs are transported to tumor cells by blood flow through capillaries and tissues and to identify better methods for delivering targeted anticancer therapies [74, 42].

Solid tumor growth modeling involves many complicated processes on a wide range of spatial and temporal scales. This multi-scale nature of tumor formation makes the governing equations involved in the mathematical modeling highly complex to solve. Multi-scale

modeling involves: the convection and diffusion of fluid flow in normal and tumor tissues at the largest scale, blood flow distribution through a network generated by tumor-induced angiogenesis at the middle scale and blood flow convection in capillary by considering non-continuous behavior of blood and adaption of capillary diameter at the smallest scale (Figure 5.1).

Modeling of diffusion and convection of flow in solid tumor tissue while considering the domain to be a porous medium with a uniform source and sink of blood flow is often undertaken. Jain *et al.* [44, 8, 45] used a model of a spherical tumor that had continuously distributed vasculature in the presence of the lymphatic system. The main assumption used to calculate pressure distribution in their model is that the net flow into the interstitial space from the vasculature is balanced by the efflux to the lymphatic system through Starling law.

In the modeling of Netti *et al.* [69], tumor vasculature was treated as an equivalent permeable vessel embedded in a uniform-pressure medium. Simulations were used to examine the effects of vessel leakiness and compliance, and interstitial fluid pressure. Soltani *et al.* [92], using a numerical element-based finite volume method for modeling a continuum equation in the porous media of spherical tumors, developed a mathematical model of interstitial fluid flow that introduced two new parameters: the critical tumor radius and critical necrotic radius. They have also applied their numerical model to different shapes of tumors to study the effects of tumor shape and size in drug delivery [93]. None of these works consider the effects of a tumor-induced network generated by tumor angiogenesis on fluid flow in normal and tumor tissues.

McDougall *et al.* [64] and Stephanou *et al.* [96] have examined flow modeling in a tumor-induced capillary network. They use continuous and discrete mathematical models of angiogenesis, described by Anderson and Chaplain [4], for generating a capillary network. The continuous model uses differential equations and is based on the mass conservation equation and chemical kinetics [4]. The discrete method of angiogenesis modeling uses the same kind of equations as the continuous model but with different interpretation of the probability quantities [4]. This method is able to model the growth and motility of endothelial cells. The advantages of this method make it suitable for use in more detailed models that consider flow and its effects on angiogenesis [64, 96]. Anderson and coworkers [64, 96] performed a Newtonian fluid flow simulation through 2D and 3D rigid capillary networks in order to investigate chemotherapy treatment efficiency. Zhao *et al.* [114] presented a numerical model that combines intravascular, transvascular, and interstitial fluid movements in 2D capillary networks originating from tumor-induced angiogenesis. They later extended their work to 3D [108]. None of the above works consider the non-Newtonian rheological properties of blood in capillaries and remodeling of microvessels in

tumor-induced networks.

The non-continuous behavior of blood in capillaries and vascular adaptation has also been incorporated into models including capillary networks [71, 63, 97, 2, 3]. The non-continuous behavior of blood includes variation of blood viscosity, with tube diameter and hematocrit (the fraction of the total volume of blood occupied by red blood cells), and an unequal fraction of hematocrit between the branches of capillary bifurcation. The capillaries adapt their diameter based on signals received from hemodynamic stimuli such as wall shear stress, pressure, and metabolic stimuli. Alarcon and co-workers developed a multi-scale model of vascular tumor growth linking vascular adaptation, blood flow, oxygen, and growth factor transport at the tissue scale to the subcellular and cellular dynamics of normal and cancerous cells [2, 3]. In their most recent work [71] the topology of the vasculature modeled by 2D regular hexagonal networks is changed from a static to a dynamic network in which new vessels and connections between existing vessels are considered.

Stephanou *et al.* [97] modeled an adaptable vasculature associated with tumor-induced angiogenesis and considered phase separation of blood flow in bifurcation and non-Newtonian behavior of blood. They investigated the effects of this remodeling on the supply of drugs to tumor cells. McDougall *et al.* [63] introduced several improvements in a model presented in [97], by examining the flow of a non-Newtonian fluid in a dynamic adaptive network. A mathematical model is presented that simultaneously combines vessel growth with blood flow through a microvessel. In the modeling of Alarcon and co-workers and McDougall and coworkers, only intravascular blood flow is considered, and the independency of transvascular flow from the interstitial flow surrounding the microvessels instead of coupling is supposed. No transvascular flow is taken into account.

Wu *et al.* [109] developed a mathematical model of tumor microcirculation, which couples microvasculature and interstitial space perfusion, and combines the intravascular and interstitial flow permitted by vascular permeability. In their work, only the vessels located in the tumor region are considered to adapt their diameter based on the compliance method presented by Netti *et al.* [69]. They used a model of angiogenesis presented in a previous paper [114], considering two distinct parent vessels to be the arteriole and venule. However, as known, the structure of the tumor-induced capillary network is extremely disorganized, and differentiating the venules from the arterioles is often problematic [74]; therefore, assuming separate arteriole and venule vessels does not seem realistic. In the adaptation method used by Wu *et al.* [109], the effects of hemodynamic and metabolic stimuli are not considered, and their compliance method is implemented only in vessels in tumor tissue. Vessels in normal tissue are assumed to have a constant diameter.

In spite of valuable work in the simulation of fluid flow in normal and tumor tissues, previous studies have not considered a model that explores the effect of capillary network adaptation by hemodynamic and metabolic stimuli on interstitial pressure. To address this omission, this thesis introduces a mathematical model that simultaneously couples interstitial fluid flow with convection non-continuous blood flow through vessels by considering a remodeling network based on hemodynamic and metabolic stimuli.

This thesis formulates a non-continuous blood flow model through a capillary network induced by a tumor combined with interstitial flow in normal and tumor tissues, taking into account the extravasation flux of fluid across the vasculature. First, the governing equations of sprouting angiogenesis are implemented to specify a capillary network in the interstitium domain. A discrete method first presented by Anderson and Chaplain [4] is used to create the vascular network in both normal and tumor tissues. Then, governing equations are introduced for blood flow through the capillary network and fluid flow in the interstitium. Finally, the effects of the capillary network on interstitial fluid flow are studied, considering three approaches for simulation of blood flow in the network. First, the governing equation for the interstitium is solved without considering a capillary network, as in [45, 92, 93]. Second, similar to the approach used in [64, 96, 114], the tumor-induced network is presumed to have rigid capillaries, and blood flow is calculated in the network by mass conservation at each junction. In the third approach, the capillaries are assumed to adapt their diameters in response to signals received from metabolic and hemodynamic stimuli. The remodeling method presented by Pries *et al.* [78] is used. For this reason, phase separation, based on the method presented by Fung, is involved in the third approach [32] and also the non-Newtonian behavior of blood, based on the formula presented by Pries *et al.* [77], is implemented. Results show that fluid flow modeling in normal and tumor tissues with a rigid vascular network can predict higher pressure than the method studied in the previous research on interstitial flow [92]. The approach considering adaptable capillaries, which is more accurate, shows even higher pressure than the second approach does.

5.2 Mathematical Model of Angiogenesis

The mathematical model used for generation of the network has been described in Chapter 4. A schematic of the solution domain in this chapter is shown in Figure 5.2

To generate the networks, two initial conditions for the number of ECs in a parent vessel are considered: 5 ECs and 10 ECs. Results of capillary network formation are shown in Figures 5.3 and 5.4. These networks are used for further studies in section 5.3.

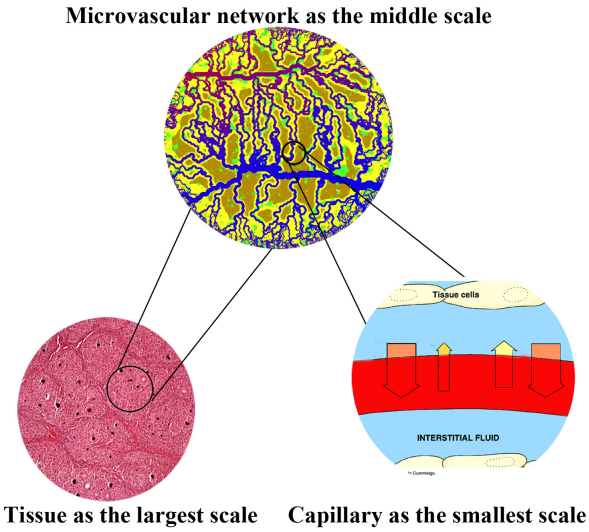

Figure 5.1: Schematic representing different scales in a solid tumor

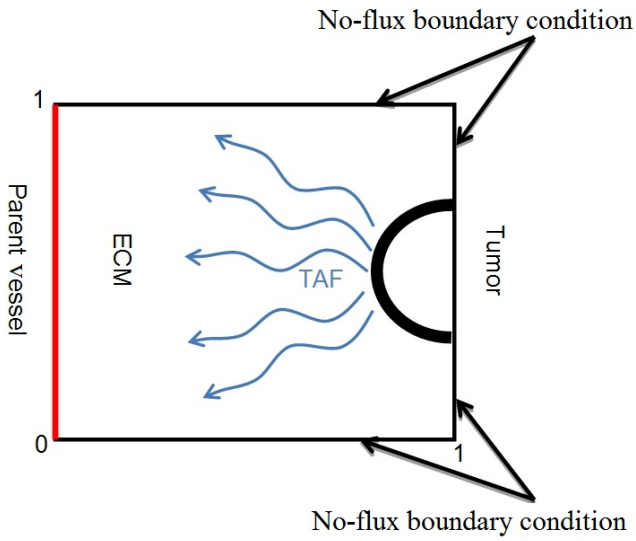

Figure 5.2: Schematic of the solution domain

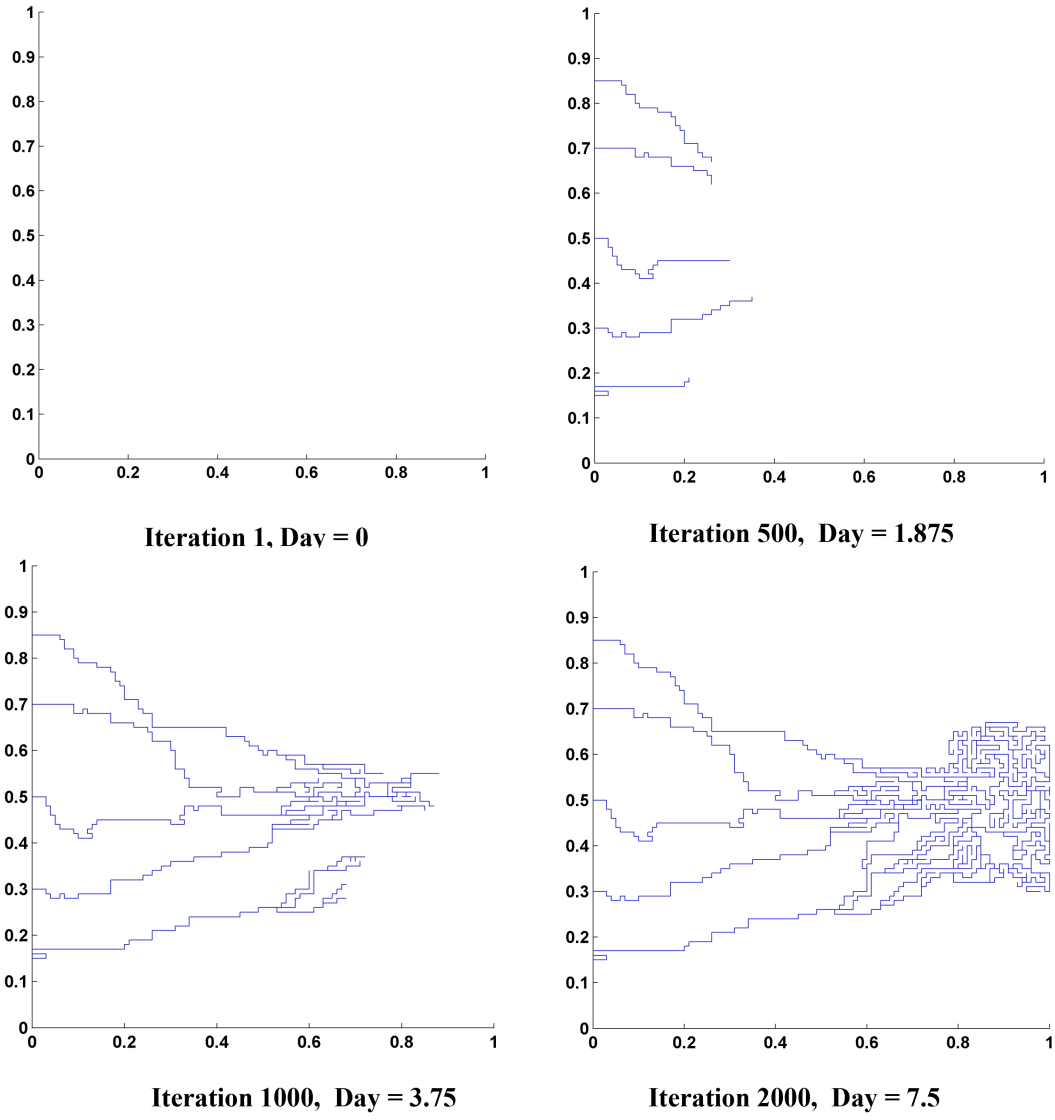

Figure 5.3: Results of discrete model. Five initial sprouts move toward the tumor on the right side of the domain

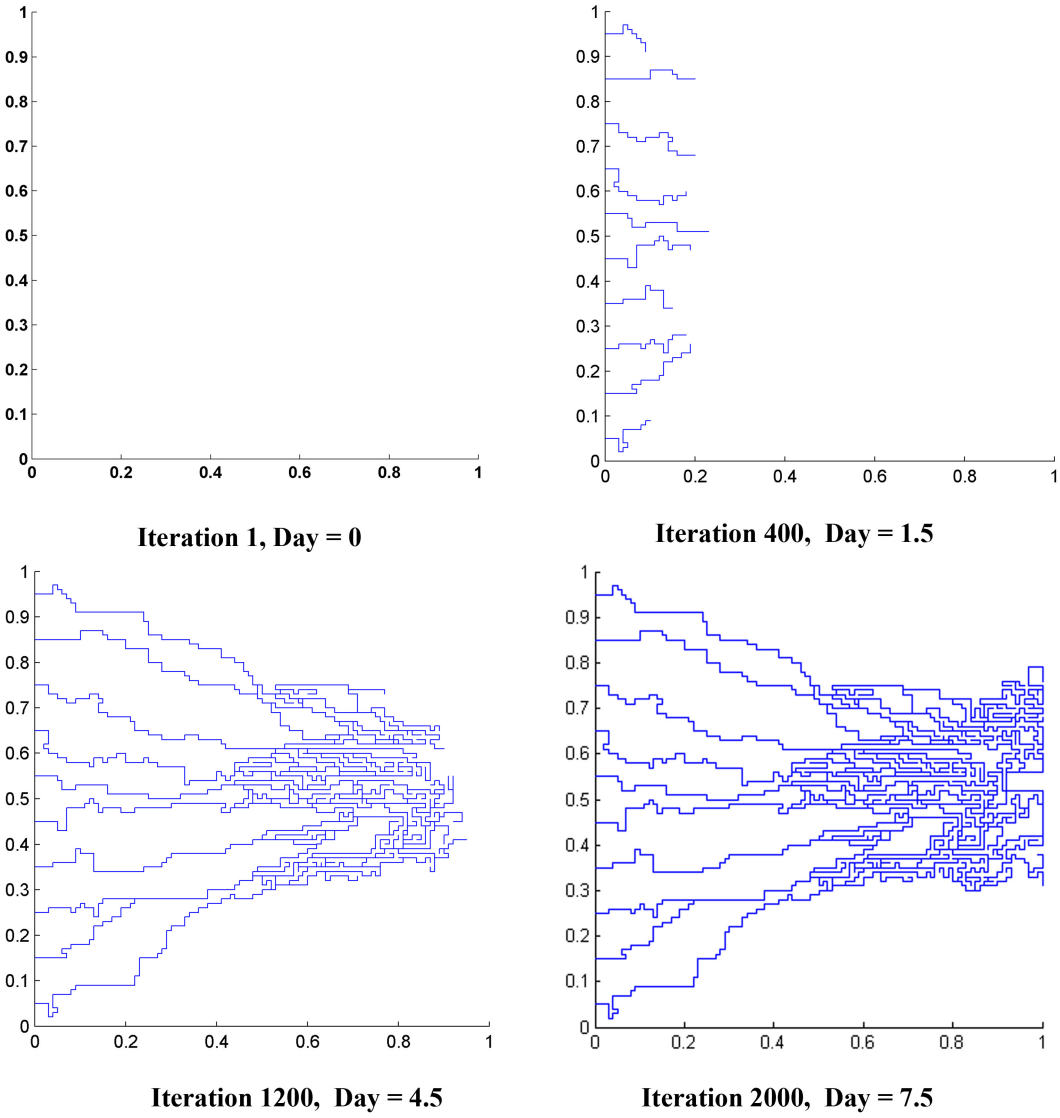

Figure 5.4: Results of discrete model. Ten initial sprouts move toward the tumor on the right side of the domain

5.3 Flow Simulation in Capillary Networks

Calculation of fluid flow in networks is used in many fields of physics, such as the water and petroleum industries. The analysis of blood flow in microvascular networks is generally the same as the analysis of other networks, but with a few significant differences. These differences are due to the permeability of vessels, changeable diameters of vessels, non-continuous behavior of blood in micro-scale vessels, and the porous nature of the medium surrounding vessels. In this section, the governing equations for a network and porous media are presented. Then the models used for the non-continuous behavior of blood and vessel adaptation are introduced.

To study incompressible flow through a network of vessels, the flow rate in each vessel is calculated by applying mass (or volumetric flow rate) conservation at each junction of the network. The equation representing the volumetric flow rate for an interconnecting point like c (Figure 5.5) in the network can be written as

$$\sum_{k=1}^{N} Q_c^k \beta_k = 0 \tag{5.1}$$

where the index k refers to adjacent nodes, and N is the number of adjacent nodes. In 2D simulation for a fully connected network, N is 4, and β_k is a positive integer '1' or '0', which describes whether nodes c and k are connected ($\beta_k = 1$) or not connected ($\beta_k = 0$).

Q_c^k is the net flow rate for each capillary and includes the flow through the capillary and transvascular flow from each capillary, or mathematically (Figure 5.6),

$$Q_c^k = Q_{B,c}^k - Q_{t,c}^k \tag{5.2}$$

where $Q_{B,c}^k$ is blood flow through each capillary and $Q_{t,c}^k$ is the extravasation flux of fluid across the vascular or transvascular flow.

Blood flow in capillary tubes has a low Reynolds number, much less than 1. For such a low Reynolds number, Poiseuille's law can be applied. Poiseuille's experiment shows the relationship between the flow rate $Q_{B,c}^k$ and the driving pressure ΔP in a tube of diameter D and length L. Theoretical analysis leads to the following equation:

$$Q_{B,c}^k = \frac{\pi}{128} \frac{\Delta P D^4}{L\mu} \tag{5.3}$$

where ΔP is calculated by $P_B^c - P_B^k$.

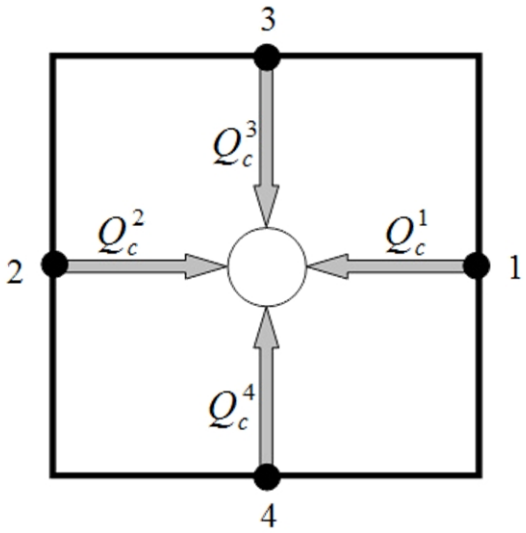

Figure 5.5: Schematic representation of blood flux at each vascular node

The transvascular flow rate is calculated by Starling's law, which represents the role of hydrostatic and oncotic pressures in the movement of fluid across capillary membranes. Starling's law [32, 84] is calculated by

$$Q_{t,c}^k = \pi D L L_p [\bar{P_B} - \bar{P_i} - \sigma_s(\pi_B - \pi_i)] \tag{5.4}$$

where

$\bar{P_B}$ is the average blood pressure in vessels, calculated by $\frac{(P_B^c + P_B^k)}{2}$

$\bar{P_i}$ is the average interstitial fluid pressure outside of the vascular element, calculated by $\frac{(P_i^c + P_i^k)}{2}$

π_B is the osmotic pressure of the plasma

π_i is the osmotic pressure of the interstitial fluid

L_p is the hydraulic conductivity of the microvascular wall

σ_s is the average osmotic reflection coefficient for the plasma proteins.

Calculation of transvascular flow rate depends on the intravascular pressure in vessels and interstitial pressure in normal and tumor tissues. The intravascular pressure is found by solving the mass conservation equation in the network by applying Poiseuille's equation

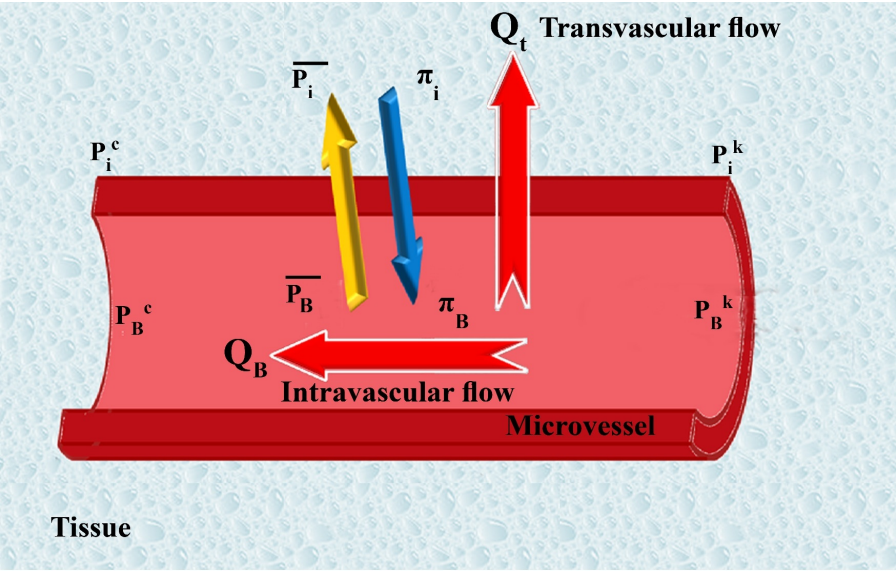

Figure 5.6: Schematic representation of blood flux through microvessel or transformation from microvessel and related parameters

for flow in vessels as mentioned. The interstitial pressure for the peripheral tissue of a vascular network is found by solving the governing equation for fluid flow through a porous medium. In fact, Equation 5.4 couples blood flow in the network and fluid transport in the tissue around the network.

The tissues, such as normal and tumor, have properties like those of a porous medium. One of the earliest formulations for flow transport in porous media is Darcy's law. Darcy's empirical observations show that the fluid velocity in porous media is proportional to the pressure gradient; therefore, fluid transport in the porous media can be described by the following equation [32, 11, 25]:

$$V_i = -k\nabla P_i \tag{5.5}$$

where

P_i is the interstitial pressure as defined before

k is the hydraulic conductivity of the interstitium

V_i is the interstitial fluid velocity.

The mass balance equation for a steady state incompressible fluid shows that the divergence of the velocity is zero, or mathematically,

$$\nabla.V_i = 0 \tag{5.6}$$

This equation is acceptable for porous media when there is no fluid source or sink in the medium, but biological tissues have sources and sinks. For instance, between the interstitial space and the blood or lymph vessels, fluid is exchanged; therefore, the steady state incompressible form of the continuity equation must be modified as in [92].

$$\nabla.V_i = \phi_B - \phi_L \tag{5.7}$$

where

ϕ_B is the rate of fluid flow per unit volume from blood vessels into the interstitial space, and

ϕ_L is the rate of fluid flow per unit volume from the interstitial space into lymph vessels.

It should be noted that Equation 5.7 in its general form is applicable to any kind of biological tissue, whether normal or cancerous. In this simulation, the value for lymph vessels is neglected. The blood vessel terms (or fluid source terms) can be evaluated through Starling's law as follows:

$$\phi_B = \frac{L_p S}{V}[\bar{P_B} - \bar{P_i} - \sigma_s(\pi_B - \pi_i)] \tag{5.8}$$

where $\frac{S}{V}$ is the surface area per unit volume of tissue for transport in the interstitium. Other terms in Equation 5.8 were introduced previously in this section.

The mass conservation equation is obtained for normal and tumor tissues with a capillary network by adding a source term for mass flow to the right-hand side of the continuity equation wherever there is a capillary; otherwise, the right-hand side of the continuity equation is simply zero, or mathematically

$$\nabla.V_i = \begin{cases} \frac{L_p S}{V}(\bar{P_B} - \bar{P_i} - \sigma_s(\pi_B - \pi_i)), & \text{for existence of blood source;} \\ 0, & \text{otherwise.} \end{cases} \tag{5.9}$$

Combination of the continuity equation and Darcy's law results in

$$-\nabla.k\nabla P_i = \begin{cases} \frac{L_p S}{V}(\bar{P_B} - \bar{P_i} - \sigma_s(\pi_B - \pi_i)), & \text{for existence of blood source;} \\ 0, & \text{otherwise.} \end{cases} \tag{5.10}$$

when k is constant

$$-k\nabla^2 P_i = \begin{cases} \frac{L_p S}{V}(\bar{P_B} - \bar{P_i} - \sigma_s(\pi_B - \pi_i)), & \text{for existence of blood source;} \\ 0, & \text{otherwise.} \end{cases} \tag{5.11}$$

Applying the appropriate boundary conditions and also using all the constants mentioned earlier, the governing equation, Equation 5.11, can be used to calculate interstitial fluid pressure in both normal and tumor tissues. As shown in Figure 5.7, a no-flux boundary condition is considered for the right-hand side of the domain and upper and lower limits of the domain, *i.e.*,

$$\nabla P_i = 0 \tag{5.12}$$

For the left-hand side of the domain near the parent vessel, the constant value of pressure is considered.

Equation 5.1, by considering Equations 5.2 to 5.4 and Equation 5.11, should be solved simultaneously to find the intravascular, P_B, and interstitial, P_i, pressures. The solution can be obtained numerically to find both P_B and P_i, and other related parameters such as velocity and flow rate. The iterative numerical method, Gauss-Seidel [76], is applied to solve the system of equations for intravascular pressure. A finite difference method is applied to discretize Equation 5.11. The discretized form of the governing equations, in their general form, is then linearized and solved explicitly by an iterative procedure. This iterative method can be called semi-implicit, as during the solution, the most updated values of pressures are used. The algorithm for the procedure and discretized form of the equations is described in Section 5.4.

5.3.1 Blood Viscosity in Capillaries

As mentioned, Poiseuille's law can be used for Newtonian flow, but blood has significant non-Newtonian properties at low Reynolds numbers. Blood viscosity in capillaries depends on the vessel diameter and hematocrit. To take advantage of Poiseuille's law's simplicity

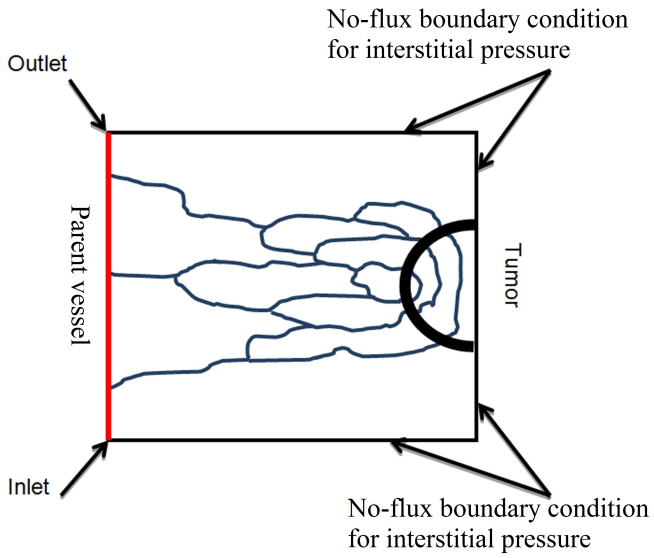

Figure 5.7: A schematic of calculated domain for fluid flow simulation

and use it to show the behavior of blood, it is helpful to define the apparent or effective viscosity of blood, according to Equation 5.3, by

$$\mu_{app} = \frac{\pi}{128}\frac{\Delta P D^4}{L Q_B} \tag{5.13}$$

Pries *et al.* [77, 81] used data obtained from the results of 18 studies of human blood and combined the data with a parametric description of apparent blood viscosity relative to the viscosity of plasma to define apparent viscosity. They introduced this parameter as the relative apparent viscosity. A description of relative apparent viscosity as a function of the tube diameter and hematocrit is as follows [77]:

$$\mu_{rel} = [1 + (\mu_{45} - 1)\frac{(1 - H_D)^C}{(1 - 0.45)^C - 1}(\frac{D}{D - 1.1})^2](\frac{D}{D - 1.1})^2 \tag{5.14}$$

μ_{45}, the relative apparent blood viscosity for a fixed hematocrit of 0.45, is given by

$$\mu_{45} = 6e^{-0.085} + 3.2 - 2.44e^{-0.06D^{0.645}} \tag{5.15}$$

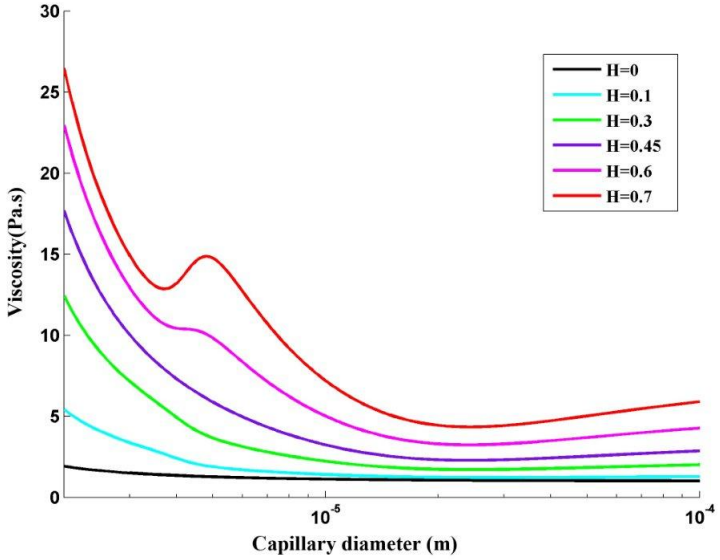

Figure 5.8: Apparent viscosity profiles as a function of vessel radius for different hematocrit values

where D is the vessel diameter (in μm), and C describes the shape of viscosity dependency on the hematocrit, defined as

$$C = (0.8 + e^{-0.075D})(-1 + \frac{1}{1 + 10^{-11}D^{12}}) + \frac{1}{1 + 10^{-11}D^{12}} \tag{5.16}$$

and

$$\mu_{app} = \mu_{plasma}.\mu_{rel} \tag{5.17}$$

The apparent viscosity corresponding to Equation 5.14 in a range of typical capillary radii for different hematocrit values and considering $\mu_{plasma} = 1.2$ is plotted in Figure 5.8. It can be seen that the apparent blood viscosity generally increases with a decrease in capillary diameters (Fahraeus-Lindquist effect), although the precise relationship is actually hematocrit-dependent. The two parameters, hematocrit and vessel diameter, affecting blood viscosity are dependent on blood flow characteristics such as velocity, wall shear stress, pressure in vessels. These dependencies are described in the next sections.

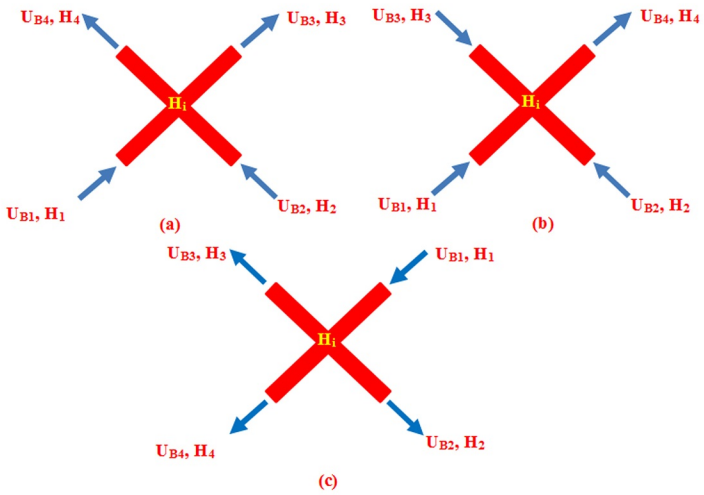

Figure 5.9: Schematic of different patterns of blood flow in networks: a) Blood flow from one (two) node(s) into one (two) node(s). b) Blood flow from three nodes into one node. c) Blood flow from one node into three nodes.

5.3.2 Phase Separation at Capillary Bifurcations

Since μ_{rel} depends on H, the hematocrit distribution has a significant role in simulating the hemodynamic characteristic of the vessel network. In general, H distribution at a vessel bifurcation depends on the flow velocity in each branch. The total red blood cell fraction in the feeding vessel of a bifurcation that goes into one of the daughter branches is not essentially the same as the fractional blood flow going into that branch. It has been shown that all the hematocrit goes into the branch with the faster velocity at bifurcations if the velocity at that branch goes beyond a certain limit. Extending Fung's conclusions [32] results in the distribution rules of H, as follows (see Figure 5.9 for definitions, assuming $U_{B2} \geq U_{B3} \geq U_{B4}$) [2]:

a)Blood flow from one (two) node(s) into one (two) node(s) (Figure 5.9a)

$$H_i = max(H_1, H_2) \qquad H_i = H_3 + H_4$$

$$\begin{cases} \dfrac{U_{B3}}{U_{B4}} \geq U_{cr}, & H_3 = H_i; \\ \dfrac{U_{B3}}{U_{B4}} < U_{cr}, & \frac{H_3}{H_4} = \zeta^{\frac{U_{B3}}{U_{B4}}}. \end{cases} \tag{5.18}$$

b)Blood flow from three nodes into one node (Figure 5.9b)

$$H_i = max(H_1, H_2, H_3) \qquad H_i = H_4 \tag{5.19}$$

c)Blood flow from one node into three nodes (Figure 5.9c)

$$H_i = H_1 \qquad H_i = H_2 + H_3 + H_4$$

$$\begin{cases} \dfrac{U_{B2}}{U_{B4}} \geq U_{cr} \ : & \begin{cases} \dfrac{U_{B2}}{U_{B3}} \geq U_{cr} \ : & H_2 = H_i \\ \dfrac{U_{B2}}{U_{B3}} < U_{cr} \ : & \frac{H_2}{H_3} = \zeta^{\frac{U_{B2}}{U_{B3}}} \end{cases} \\ \dfrac{U_{B2}}{U_{B4}} < U_{cr} \ : & \begin{cases} \dfrac{H_2}{H_3} = \zeta \dfrac{U_{B2}}{U_{B3}} \\ \dfrac{H_2}{H_4} = \zeta^2 \dfrac{U_{B2}}{U_{B4}} \end{cases} \end{cases} \tag{5.20}$$

where H_i denotes H at node i, ζ is a phenomenological parameter that accounts for the strength of the non-symmetry of the hematocrit distribution at bifurcations [2], and U_{cr} is the critical ratio of the velocities of the branches, above which, the total hematocrit goes to the faster branch [2]. Here, the hematocrit in the parent vessels and their joint nodes with the connected induced network is assumed to be a constant 0.45.

5.3.3 Vessel Diameter Adaptation

Capillaries are able to continuously adapt their diameter in response to the functional requirements of the tissues that capillaries supply [78, 82]. Each vessel responds locally

to physical and biochemical stimuli. In fact, wall shear stress and intravascular pressure created by blood flow lead to remodeling of the vascular diameter. The biochemical stimuli such as the metabolic are also able to remodel the capillary network generally. For each vessel in the network, the change of its diameter (ΔD) for a time step (Δt) is assumed to be proportional to the stimulus term, its initial diameter, and the time step:

$$\Delta D = S_{tot}.D.\Delta t \tag{5.21}$$

S_{tot} includes the influences of the wall shear stress (S_{wss}), the intravascular pressure (S_p), and a metabolic mechanism depending on the blood hematocrit (S_m). Each stimulus is next briefly discussed.

5.3.4 Wall Shear Stress

Experimental observations show that to maintain a specific level of wall shear stress, the vessels adapt their diameter. Murray [65] showed that when the volumetric blood flow rate in each vessel is proportional to the cube of the vessel diameter, the energy consumption for pumping the blood to the circulatory system is minimal. The wall shear stress in a capillary vessel is given by

$$\tau_w = \frac{32 Q_B \mu}{\pi D^3} \tag{5.22}$$

Based on Equation 5.22, to satisfy Murray's law, wall shear stress needs to be approximately constant in vessels. Therefore, when each vessel senses wall shear stress, it adjusts its diameter to achieve a uniform level of stress. Experimental observation [80] shows that vessel diameter increases when wall shear stress increases. This stimulus is described by the following logarithmic law:

$$S_{wss} = \log_{10}(\tau_w + \tau_{ref}) \tag{5.23}$$

where τ_w is the actual wall shear stress in a vessel segment calculated by Equation 5.22, and τ_{ref} is a small constant included to avoid singular behavior at low wall shear stress rates.

Considering only wall shear stress for vessel adaptation tends to give unstable remodeling. The instability causes the diameter of one vessel in a parallel connection to approach

zero and the other one to carry the entire flow. Another problem of considering only wall shear stress is that the vessel diameters must be equal on both the arterial and venous sides.

5.3.5 Intravascular Pressure

Shear stress values differ significantly between arterial and venous vessels. The values in the arterial system are always greater than those in a venous one [80]. Studying structural adaptation, Pries *et al.*, suggested a preset relationship between local intravascular pressure and wall shear stress [79]. They showed that increasing intravascular pressure decreases vessel diameter. To consider the corresponding stimulus of intravascular pressure, they suggested a negative sensitivity represented by the following equation:

$$S_P = \log_{10} \tau_e(P_B) \tag{5.24}$$

in which $\tau_e(P_B)$ is the wall shear stress resulting from the blood pressure ,P_B, based on the experimental data on rat mesenteries [79]. As shown in Figure 5.10, this wall shear stress increases, in a sigmoidal shape, as pressure increases.

$$\tau_e(P_B) = 10 - 8.6 \exp\left[-5000\left[\log_{10}(\log_{10} P_B)\right]^{5.4}\right] \tag{5.25}$$

In this equation, pressure and stress are obtained in $mmHg$ and Pa, respectively. As shown in Figure 5.10, for pressure less than $10mmHg$, Equation 5.25 is not applicable. Instead, the value of $1.4Pa$ is considered.

5.3.6 Metabolic Hematocrit-related Stimulus

The metabolic requirement of tissue can affect and control vascular diameter. A drop in oxygen supply or other metabolic material stimulates the vessel to increase its diameter to enhance perfusion. Pries *et al.* [78, 82] suggested adding a stimulus dependency to the volume flux of red blood cells passing through a vessel (represented by $Q_B H$), thus, increasing this volume flux decreases the stimulus effect. This stimulus is once again described by a logarithmic law, given by

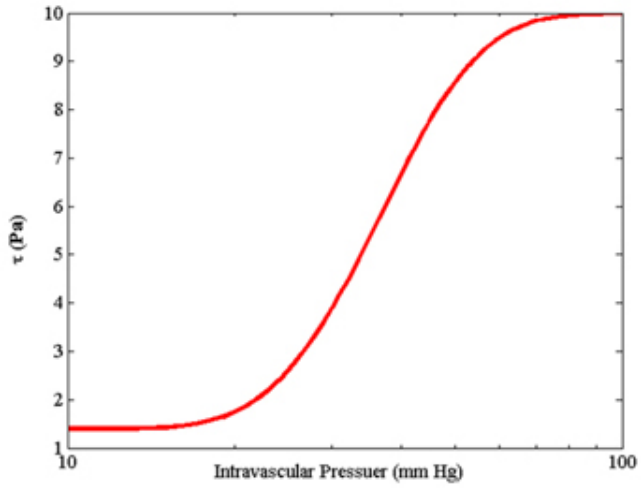

Figure 5.10: Shear stress induced by intravascular pressure in a range of pressure in a circulatory system. Equation is derived by Pries *et al.* [79] using curve fitting from experimental results obtained on rat mesentery vessels.

$$S_m = \log_{10}\left(\frac{Q_{ref}}{Q_B H} + 1\right) \tag{5.26}$$

where Q_{ref} is the largest value of Q_B in the network. In this simulation, the flow rate of parent vessels corresponds to Q_{ref}.

5.3.7 Vascular Adaptation

The total signal for diameter adaptation is represented in the model by the following equation, which remodels the structure of the capillary network.

$$S_{tot} = S_{wss} - k_p S_p + k_m S_m - k_s \tag{5.27}$$

Here, the parameter k_p is introduced to indicate the adaptive response sensitivity of vessel diameters to changes in intravascular pressure [78]. k_m is the sensitivity of the adaptive response of the vessel diameter to changes in metabolic state [82].

The vessel has a tendency to reduce in size in the absence of positive growth stimuli. The shrinking tendency, k_s, is applied to show this tendency [82]. Finally, the model for vessel adaptation is given by the following equation:

$$\Delta D = \left[\log_{10}(\tau_w + \tau_{ref}) - k_p \log_{10} \tau_e(P_B) + k_m \log_{10}\left(\frac{Q_{ref}}{Q_B H} + 1\right) - k_s\right] D\Delta t \tag{5.28}$$

5.4 Numerical Simulation

Intravascular pressure is numerically calculated at each node by integrating Equations 5.1, 5.2, 5.3, 5.4, and then P_B in each node (c) is given by

$$P_{B,c}^{q+1} = \frac{\sum_{k=1}^{4}\left[\left(\frac{D_{k-c}^4}{128\mu_{k-c}L} - D_{k-c}LL_P\right)P_{B,k}^q + D_{k-c}LL_P\left(\frac{P_{i,c}^q + P_{i,k}^q}{2} - \sigma_s(\pi_B - \pi_i)\right)\right].\beta_c^k}{\sum_{k=1}^{4}\left(\frac{D_{k-c}^4}{128\mu_{k-c}L} + D_{k-c}LL_P\right).\beta_c^k} \tag{5.29}$$

where q is the number of iterations. This procedure leads to a set of linear equations for the nodal pressures. These equations can be solved numerically using the Successive Over-Relaxation (SOR) algorithm. Once nodal pressures are known, Equation 5.3 can be used to calculate the flow in each capillary element in turn.

The interstitial pressure is found by solving Equation 5.11. The iterative numerical method is used to solve the discretized form of Equation 5.11, given as

$$P_{i,c}^{q+1} = \frac{\sum_{k=1}^{4}\left[P_{i,k}^q + L^2\frac{L_p S}{kV}A_{c,k}\left(P_B^q - \sigma_s(\pi_B - \pi_i)\right)\right]}{\sum_{k=1}^{4}\left(4 + L^2\frac{L_p S}{kV}A_{c,k}\right)} \tag{5.30}$$

where q again is the number of iterations, and $A_{c,k}$ is 1 or 0, describing the existence of a blood source. To solve this equation, the SOR algorithm is used.

5.4.1 Algorithm for Calculating Fluid Flow in Capillaries with Remodeling

The fluid flow calculation in capillary vessels includes a set of non-linear equations. For this reason, an iterative procedure is applied to solve the fluid flow and remodeling in a capillary network. The procedure is as follows:

1. Considering initial guesses for $P_B^0, P_i^0, \mu_{app}^0, H^0$ and D^0,
2. Calculating P_B^N, P_i^N iteratively based on Equations 5.29 and 5.30 as described,
3. Calculating the total adaptive stimuli using Equations 5.23, 5.24 and 5.26,
4. Updating vessel diameter D using Equation 5.28,
5. Calculating Q_B by Equation 5.3,
6. Calculating the velocity in each vessel by $U_B = \frac{4Q_B}{\pi D^2}$,
7. Finding H by a procedure described in Section Phase Separation at Capillary Bifurcations,
8. Updating the apparent viscosity by Equation 5.14,
9. Calculating the relative error for P_B ,P_i and D by $max(\frac{X^N - X^0}{X^0})$, where X can be each of P_B ,P_i and D,
10. Checking the maximum relative error of P_B, P_i and D with a criteria solution which is considered to be $1e-6$,
11. If the error is greater than the solution threshold, the iterative procedure returns to step 2, and the new solutions of P_B, P_i, μ_{app}, H and D are substituted for the previous values. Otherwise, the iteration procedure is considered to be finished.

5.5 Model Parametrization and Simulation Details

5.5.1 Initial Conditions

The $2D$ domain (shown in Figure 5.7) considered for the computational simulation studies is a square of length $L_x = L_y = 2mm$, and the parent vessel from which the vascular

network grows is located at the left edge of the domain. The tumor is located along the right edge of the domain boundary. The equations for tumor-induced capillary growth are solved numerically on a $100 \times 100(x, y)$ square grid. P_i^0 is initialized to be zero, and P_B^0 is considered to be $1330Pa$, based on boundary condition [8].

5.5.2 Intravascular Flow Model Parameters

In order to simulate the fluid flow in capillaries, several important physical and biological parameters must first be estimated.

5.5.3 Vessel Properties

The initial diameter of each capillary segment is assumed to be $12\mu m$, and for the parent vessel it is $28\mu m$, a value that stays constant during the remodeling procedure. During the remodeling process, allowable diameter changes are in the range of $4\mu m$ to $24\mu m$ [20].

5.5.4 Adaptation Parameters and Phase Separation

Parameters used for the adaptation model and phase separation presented in Equations 5.18 to 5.20 and 5.28 are listed in Table 5.1.

Table 5.1: Parameter values used in the adaptation

Parameter	Value	Reference
$\tau_{ref}[Pa]$	0.0103	[78]
$Q_{ref}[\frac{mm^3}{s}]$	4.87×10^{-3}	Calculated
$k_p[\frac{1}{s}]$	0.1	[71]
$k_m[\frac{1}{s}]$	0.07	[71]
$k_s[\frac{1}{s}]$	035	[71]
U_{cr}	2.5	[2]
ζ	0.5	[2]

in which Q_{ref} is the flow rate in the parent vessel, calculated by Equation 5.3 assuming $D = 28\mu m$, $L = 2mm$ and $\Delta P = 1950\,Pa\,(15\,mmHg)$ (the pressure drop across the parent vessel), and $\mu_{app} = 0.0031[Pa.s]$ calculated by Equation 5.14. The plasma viscosity, μ_{plasma}, is assumed to be $1.2 \times 10^{-3}\,Pa.s$. The discharge hematocrit $H = 0.45$ is assumed to stay constant in the parent vessel [78]. The intravascular pressure, P_B, is an important factor in the vascular remodeling process. In this simulation, inlet and outlet pressures are chosen in the hope of guaranteeing that the average intravascular pressure is about $2660\,Pa\,(20\,mmHg)$, based on the physiological values reported in the literature [97]. Taking into account the physiological condition at microvascular scale results in considering $3325\,Pa\,(25\,mmHg)$ for the inlet and $1330\,Pa\,(10\,mmHg)$ for outlet pressures.

5.5.5 Interstitial Flow Model Parameters

The material properties for tumor and normal tissue used for interstitial flow calculation are taken from the simulation study in Chapter 2 and are shown in Table 5.2.

Table 5.2: Material properties used in numerical simulations, as taken from [44]

Parameter	Normal Tissue	Tumor Tissue
$L_p[cm/mmHgs]$	0.36×10^{-7}	2.80×10^{-7}
$K[cm^2/mmHgs]$	8.53×10^{-9}	4.13×10^{-8}
$S/V[cm^{-1}]$	70	200
$\pi_B[mmHg]$	20	20
$\pi_i[mmHg]$	10	15
σ	0.91	0.82

5.6 Results

Three approaches are used for calculating interstitial pressure in a cancerous tissue. First, the results of the initial approach are presented by solving the governing equations for normal and tumor tissues without a network, as in work done in Soltani *et al.* [93, 92]. Then the results of the second approach are obtained by simulating fluid flow in a network induced by tumor angiogenesis with constant values for blood rheology and vessel diameters. Finally, results obtained using the proposed realistic approach, in which the

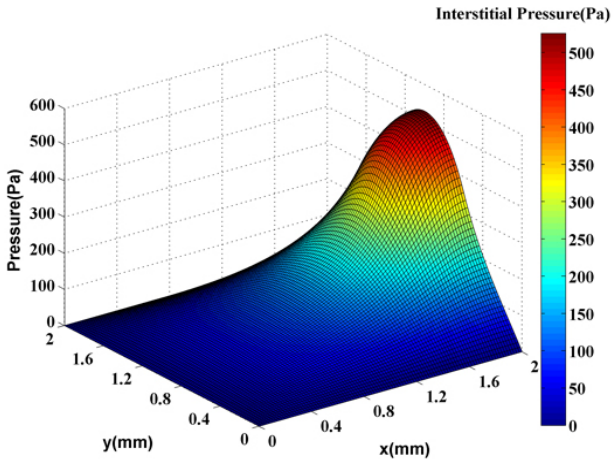

Figure 5.11: 3D graph of interstitial pressure in the computational domain for both normal and tumor tissues in which uniform distribution and constant values for intravascular pressure are assumed.

non-continuous behavior of blood and adaptability of capillary diameters are assumed, are investigated.

As mentioned, to show how a capillary network affects the fluid flow in normal and tumor tissues, the tumor's interstitial fluid flow is simulated without considering such a network. For this simulation, it is supposed that intravascular pressure, P_B, has uniform distribution in the domain and is constant throughout the simulation. A 3D plot of this interstitial pressure distribution is shown in Figure 5.11. Figure 5.12 shows a 2D contour of interstitial pressure.

Now, results of fluid flow in normal and tumor tissues are presented by considering the capillary network induced by the tumor. The data on vessels' connection of networks shown in Figures 5.3 and 5.4 are used for the simulation of blood flow. Before solving the fluid flow, the network must be pruned. As the network has some segments that do not make a loop, these are removed. That is, each segment should have at least two neighbors, so if a segment has less than two (0 or 1), it is killed. The pruned networks are illustrated in Figures 5.13 and 5.14 for different values of ECs.

As mentioned, for the illustrated pruned networks, first the simulation of blood flow through capillaries and fluid flow in tissue are solved based on governing equations presented in section 5.3, without the assumption of non-continuous properties of blood in

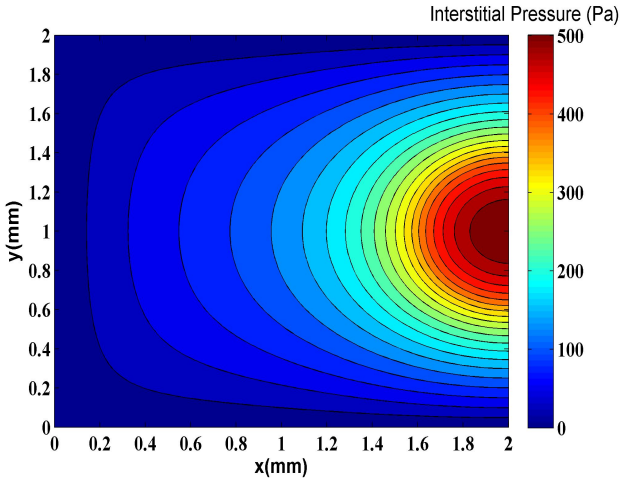

Figure 5.12: Contour of interstitial pressure in the computational domain for both normal and tumor tissues, assuming uniform distribution and constant values for intravascular pressure. The maximum pressure is around $500Pa$ in the tumor region.

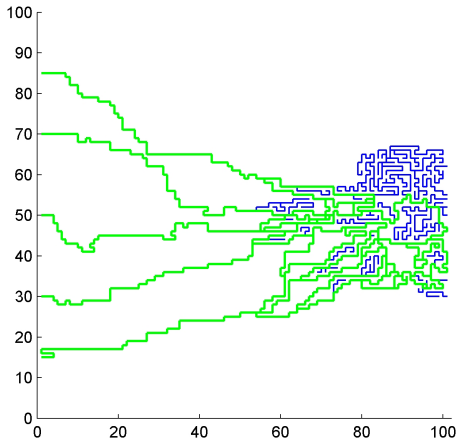

Figure 5.13: Vascular network after pruning for a network with 5 ECs in the parent vessel. The green lines show the pruned network. The blue lines are killed segments that do not make a loop.

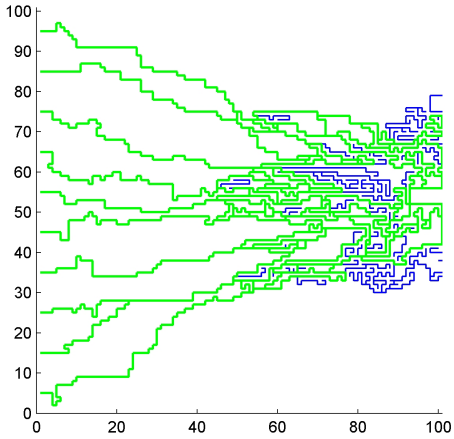

Figure 5.14: Vascular network after pruning for a network with 10 ECs in the parent vessel. The green lines show the pruned network. The blue lines are killed segments that do not make a loop.

capillaries and changes of capillary diameter due to metabolic and hemodynamic stimuli. In this simulation, the capillary diameter is prescribed using a method presented by Wu *et al.* [108], the hematocrit in the vessels is assumed to be constant and equal to 45% [64]. The viscosity for each segment is calculated based on Equation 5.14. The algorithm introduced before is used, except that the D, H and μ are assumed to have constant values that do not change in the iteration procedure. The 3D graph of interstitial pressure is shown in Figures 5.15 and 5.16 for different numbers of ECs. The 2D contour is also illustrated in Figures 5.17 and 5.18. This method results in higher pressure in the solid tumor region for both networks.

For more-realistic simulation of the problem, the effects of non-Newtonian blood rheology, non-uniform distribution of hematocrit in bifurcation due to non-continuous behavior of blood and remodeling of the network due to adaptability of capillary are coupled to the previous approach. Figures 5.19 and 5.20 show the fluid flow for a network with both adaptable and rigid capillary. Results show uniform distribution of flow in the adaptable capillary network. Results for intravascular pressure in the two cases are presented in Figures 5.21 and 5.22. The pressure at the right side of domain, the solid tumor region, is higher than that of the rigid network. In fact, based on Starling law, the higher intravascular pressure can increase the transvascular flow and slightly affect interstitial flow.

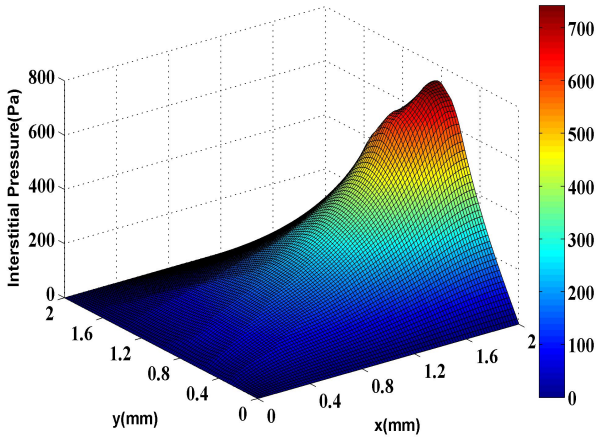

Figure 5.15: 3D graph of interstitial pressure in the computational domain for both normal and tumor tissues for a network with 5 ECs in the parent vessel

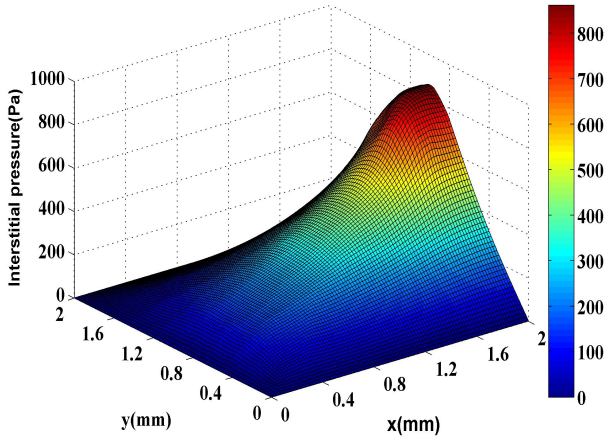

Figure 5.16: 3D graph of interstitial pressure in the computational domain for both normal and tumor tissues for a network with 10 ECs in the parent vessel

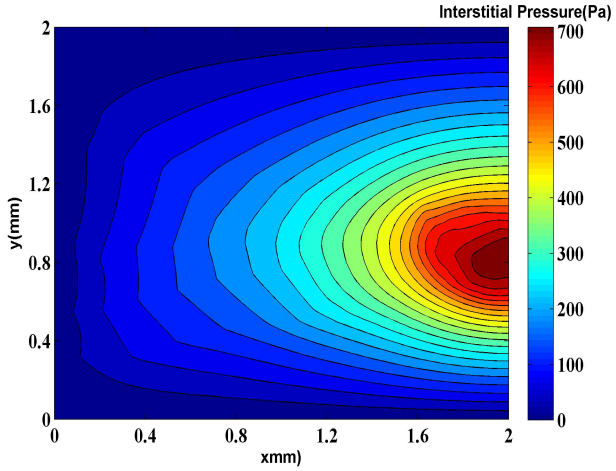

Figure 5.17: Contour of interstitial pressure in the computational domain for both normal and tumor tissues for a network with 5 ECs in the parent vessel. The maximum pressure is about $700Pa$ in the tumor region.

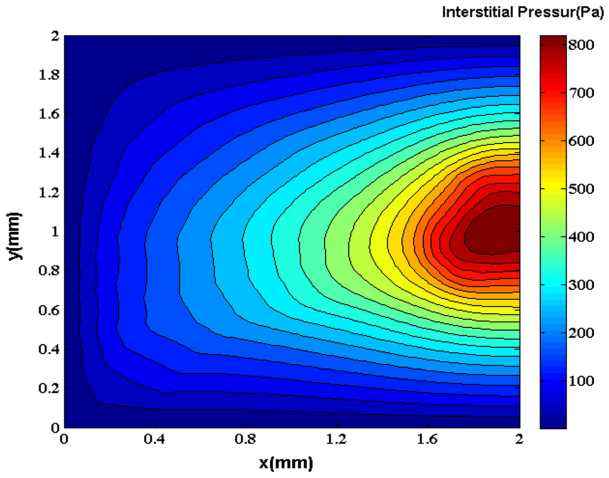

Figure 5.18: Contour of interstitial pressure in the computational domain for both normal and tumor tissues for a network with 10 ECs in the parent vessel. The maximum pressure is about $800Pa$ in the tumor region.

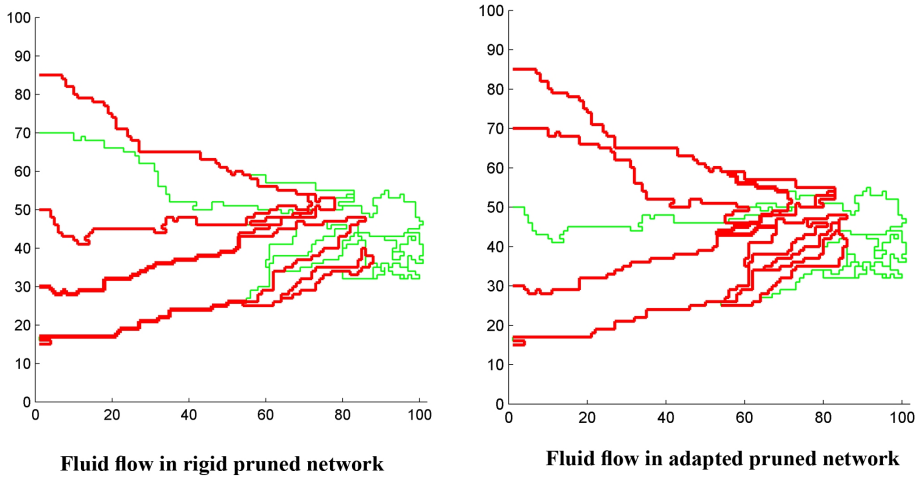

Figure 5.19: Fluid flow in rigid and adaptable capillary network for network with 5 ECs

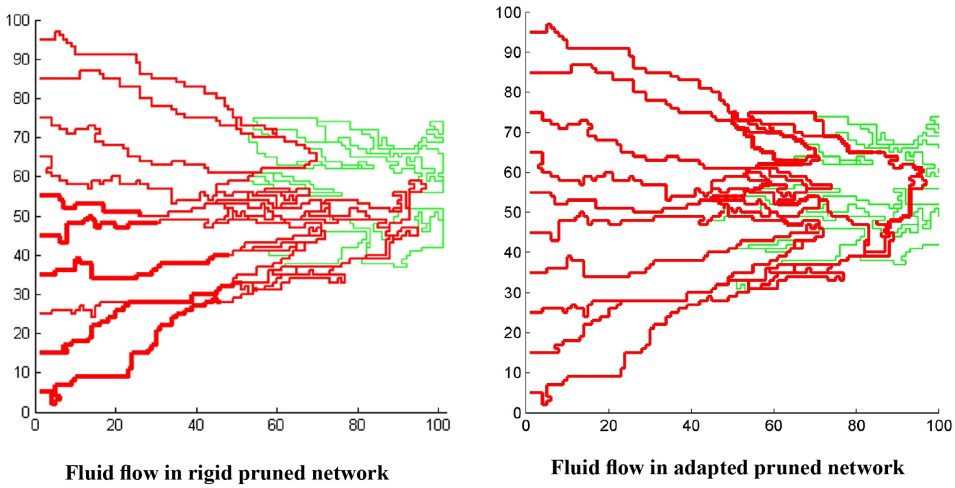

Figure 5.20: Fluid flow in rigid and adaptable capillary network for network with 10 ECs

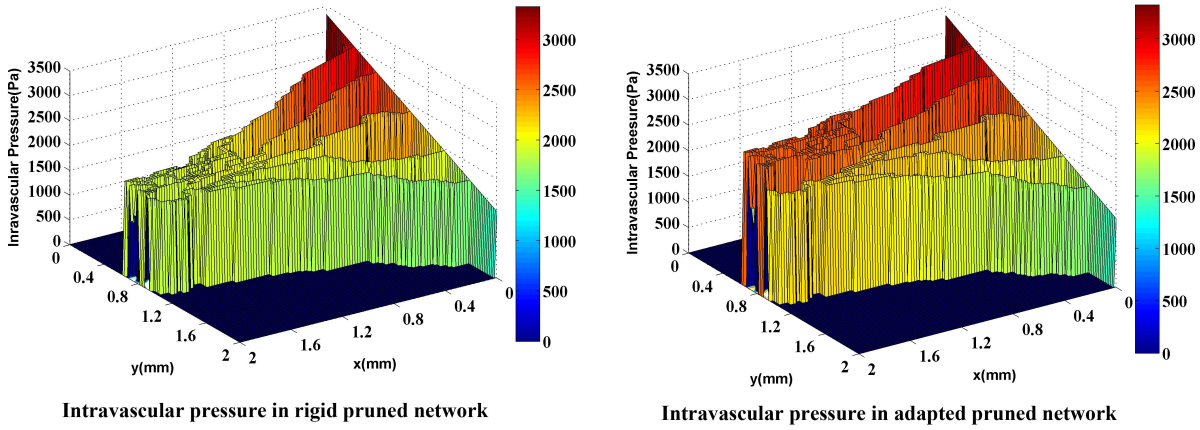

Figure 5.21: Intravascular pressure in the two cases simulated: rigid network and adaptable capillary for the network with 5 ECs. The adaptable network shows higher pressure near the solid tumor. This pressure can affect interstitial fluid flow in this region.

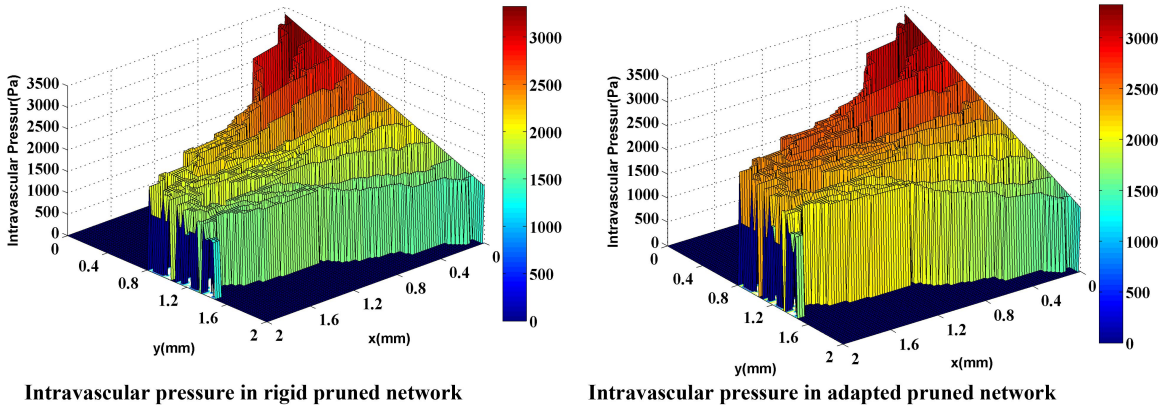

Figure 5.22: Intravascular pressure in the two cases simulated: rigid network and adaptable capillary for the network with 10 ECs. The adaptable network shows higher pressure near the solid tumor. This pressure can affect interstitial fluid flow in this region.

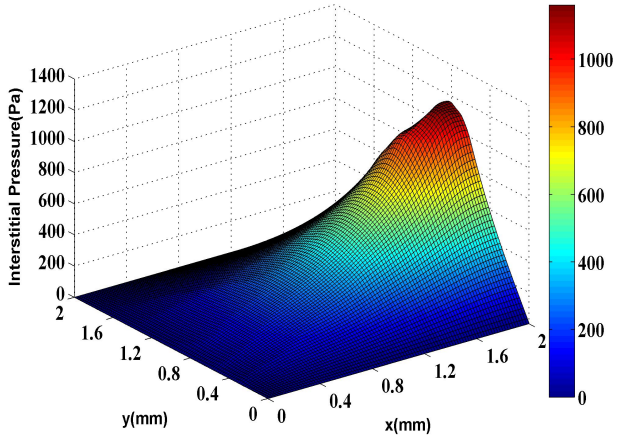

Figure 5.23: 3D graph of interstitial pressure in the computational domain for both normal and tumor tissues for a network with 5 ECs in the parent vessel

Figures 5.23 and 5.24 show the interstitial pressure in normal and tumor tissues when the adaptation method and phase distribution in the network are considered. 2D contours are illustrated in Figures 5.25 and 5.26. Results show higher pressure than in other cases introduced previously in this study.

5.7 Discussion

To accurately predict chemotherapy success, researchers must be able to precisely calculate the interstitial and intravascular pressure of tumors. In many studies, the intravascular pressure is considered to be constant in the fluid flow modeling of tissues which is not an accurate reflection of reality. This study simultaneously simulates the fluid flow in a tumor-induced capillary network and the interstitial fluid flow in normal and tumor tissues. For all simulations, a rectangular 2D domain, shown in Figure 5.7, is considered, in which a circular tumor is located on one side and the parent vessel is located on the opposite side.

To clarify the effect of considering a network on interstitial flow in tumor and surrounding tissue, for the first approach, the fluid flow in the interstitium is simulated without considering a network. In other words, the governing equation for interstitial fluid is solved

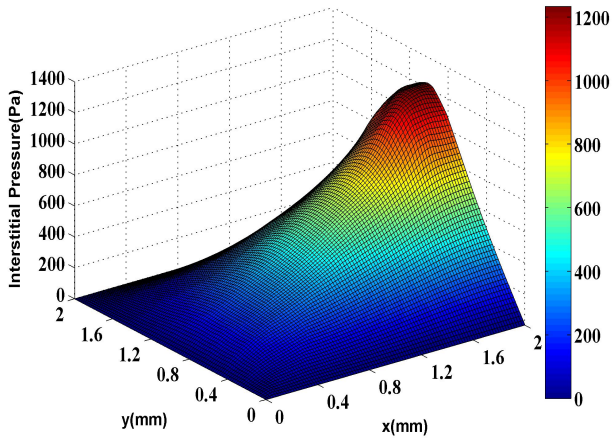

Figure 5.24: 3D graph of interstitial pressure in the computational domain for both normal and tumor tissues for a network with 10 ECs in the parent vessel

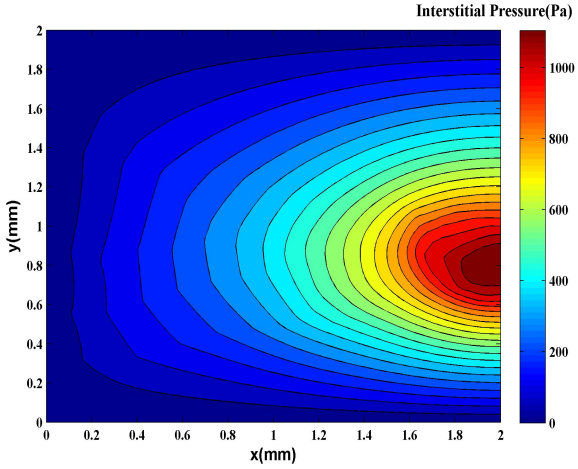

Figure 5.25: 2D contour of interstitial pressure in the computational domain for both normal and tumor tissues for a network with 5 ECs in the parent vessel. The maximum pressure is above $1100Pa$ in the tumor region.

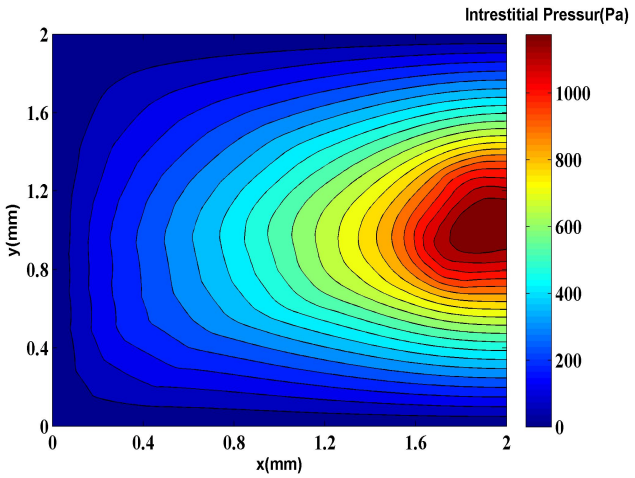

Figure 5.26: 2D contour of interstitial pressure in the computational domain for both normal and tumor tissues for a network with 10 ECs in the parent vessel. The maximum pressure is above $1200Pa$ in the tumor region.

for the above-mentioned domain with an assumed constant value for blood pressure and uniform distribution of the source term in the Darcy's equation. The values calculated for the interstitial pressure of a $0.2mm$ radius solid tumor located in a $2mm \times 2mm$ domain, shown in Figures 5.11 and 5.12, show that the maximum pressure is approximately $500Pa$. Numerical results show that the interstitial pressure value is at its maximum at the center of the tumor and decreases towards the periphery, thus showing good agreement with results in the literature [92, 93]. As mentioned in previous studies, the governing equation is the combination of Darcy's law and the continuity equation that considers a uniform source of mass flow from vessels through Starling equation [92, 93].

To investigate the effect of a capillary network on flow characteristics in normal and tumor tissues, the tumor-induced capillary network is generated by a discrete angiogenesis model. Two networks are produced, one with five endothelial cells and the other with ten endothelial cells on the parent vessel.

As mentioned, two approaches, rigid and adaptable capillary networks, are studied. The comparison of blood flow illustrated in Figures 5.19 and 5.20 for the two networks shows that the blood flow in the capillary network for the remodeled networks has a more logical distribution than the networks with rigid capillaries. To show these results, another pruning method is also applied to eliminate those capillaries that have a flow rate of less

than 1% of the network's maximum flow rate. In the first approach, many capillaries near the tumor are eliminated; however, in the remodeled network, these capillaries remain.

The proper distribution of blood flow in the remodeled network that causes decreased blood-flow resistance far from the parent vessel increases the value of intravascular pressure in the network, especially near the tumor, as shown in Figures 5.21 and 5.22. This increased intravascular pressure causes an increase of the rate of transvascular flow based on Starling' equation and therefore it affects the interstitial pressure.

Results of interstitial pressure distribution for both networks and two approaches are shown in Figures 5.15, 5.16, 5.23, and 5.24. The two approaches to blood flow modeling through capillaries considered in the fluid flow simulation for both networks show significantly different results than those for the case without a network (uniform distribution of vessels [92, 93]). When the size of the vessels is constant, the maximum value of the interstitial pressure is higher than $700Pa$ for the network with 5 ECs initially and $800Pa$ for the network with 10 ECs initially. The differences between the two networks are due to the higher density of vessels close to the tumor region. Generally, the results show an approximately 1.5 times increase on the maximum pressure resulting from constant and uniform distribution of intravascular pressure.

The interstitial pressure calculations based on the third approach, an adaptable capillary, to blood flow simulation through capillaries, shown in Figures 5.23 and 5.24, predict pressure values of around $1100Pa$ for the network with 5 ECs initially and $1200Pa$ for the network with 10 ECs initially. For both networks, the results show pressure approximately 1.5 times greater than that of the rigid network and more than two times greater than that of the constant and uniform distribution of intravascular pressure. Thus, the results confirm the importance of considering a network generated by tumor-induced angiogenesis in simulations of fluid flow in normal and tumor tissues.

The contour of interstitial pressure for normal and tumor tissues without a network has regular distribution (Figure 5.12), but the evaluation of contours in Figures 5.17, 5.18, 5.25, and 5.26 indicates that the regular distribution of pressure is changed because of irregular source terms of mass flow to the tissue. Comparison of Figures 5.17 and 5.18 with Figures 5.25 and 5.26 shows the effect of considering remodeling of networks, especially in a network with an initial 10 ECs. The distribution of interstitial pressure, shown in Figure 5.18, has a tendency to the inlet of the parent vessel. Thus, the transvascular source term has greater value in the region near the inlet of the parent vessel. This effect is observed in blood flow distribution (Figure 5.20).

The interstitial pressure of the remodeled network, illustrated in Figure 5.26, indicates that the distribution of pressure has a tendency to move to the center of the domain.

Indicative of the better distribution of blood flow in the remodeled network, the pressure distribution in Figure 5.26 shows more-uniform distribution of the source terms calculated based on Starling's law. This effect is not clearly observed in the network with an initial 5 ECs, due to lower density of vessels near the tumor.

5.8 Conclusion

This study provides numerical simulation of fluid flow in normal and tumor tissues in two situations: constant and uniform distribution of intravascular pressure in the whole domain, and distribution of intravascular pressure based on tumor-induced vascular network, using two methods, first a rigid vascular network, and second, an adaptable vascular network. The interstitial pressure in the case considering a tumor-induced capillary network is higher than that shown in the modeling without a network and in previous work by our group, in which constant and uniform distribution of intravascular pressure was assumed. The second method of considering a capillary network shows the highest interstitial pressure in the tumor region. The third method assumes the capillary diameter to be adaptable (a function of hemodynamic and metabolic stimuli), and considers phase separation of red blood cells at bifurcation points and dependency of the blood viscosity on the diameter and hematocrit (Fahraeus Lindqvist effect). Considering the above-mentioned phenomena such as adaptability of vessels and non-continuous behavior of blood causes a more-uniform blood flow distribution than that for the rigid capillary network. In the latter method, capillaries far from a parent vessel have flow, but in the former method, using a rigid capillary network, many of these capillaries are eliminated because of their low flow rates. In the third approach results show the highest interstitial pressure in the tumor region. The high pressure in the tumor region and also low transvascular flow due to low intravascular pressure in the heterogeneous capillary network near the tumor region play a significant role in non-uniform distribution of drug in a solid tumor.

Chapter 6

Summary and Future Work

This thesis has introduced the problem of drug delivery to solid tumors and discussed the details of computational fluid flow in homogenized and heterogenized solid tumors. Simulation of solid tumor microvasculature has a significant role in improving chemotherapy, in which drug particles are introduced into a patient's body in the hope that they will reach tumor cells. Substantial clinical, laboratory, and theoretical research has been carried out to show that fundamental understanding of drug transport to tumor cells is very important to improving chemotherapy efficiency. Simulation results are used for predicting how therapeutic drugs are transported to tumor cells by blood flow through capillaries and tissues.

Solid tumor modeling involves a wide range of spatial and temporal scales. This multi-scale nature of tumor formation makes the governing equations involved in the mathematical modeling highly complex to solve. Multi-scale modeling involves three scales: convection and diffusion of fluid flow in normal and tumor tissues at the largest scale, studied in Chapters 2 and 3; blood flow distribution through a network generated by tumor angiogenesis, investigated in Chapter 4, at the middle scale; and simulation of blood flow convection in capillary vessels by considering non-continuous behavior of blood and adaption of diameter at the smallest scale, implemented in Chapter 5.

For the purposes of discussion, in homogenized tumors (Chapters 2 and 3), vasculature was first assumed to be distributed uniformly and tumor shapes were assumed to be idealized. Then other, irregular shapes, such as prolate and oblate solid tumors, were considered. In heterogenized tumors (Chapters 4 and 5), the capillary network model of angiogenesis was applied to make a more-realistic model of vasculature in both tumor and normal tissues.

The distributions of interstitial fluid pressure and velocity have been calculated by numerical solutions of the governing equations. Comparison of these numerical solutions and experimental data in the literature shows that the maximum value for the interstitial pressure occurs at the center of the tumor and decreases towards the periphery and that the numerical values of interstitial fluid velocity and the experimental results reported in the literature agree. Interstitial fluid pressure is not uniform, whether the tumor vasculature is homogeneous or heterogeneous. Thus, in addition to the heterogeneous distribution of blood supply, high interstitial pressure plays a significant role in drug distribution in a solid tumor.

This study has introduced two new parameters, the critical tumor radius and critical necrotic radius. Simulation results show that for tumors below the critical tumor radius, the maximum interstitial fluid pressure is less than effective pressure; therefore, the transport of the drug to the center of smaller tumors is much easier than transport to the center of a tumor whose radius is greater than the critical tumor radius, as the maximum interstitial fluid pressure is much lower than effective pressure. This study shows that there is a critical necrotic radius, below which the interstitial fluid pressure at the center of the tumor is at its maximum value. If the tumor radius is greater than the critical tumor radius, this maximum pressure is equal to the effective pressure. Above this critical necrotic radius, the interstitial fluid pressure at the center of the tumor is below effective pressure.

This thesis has also shown that, as a rule, it is not true that the leakier the vessels, the higher the value of convective transport of drugs to solid tumors. The results do show that only in spherical solid tumors with a radius of less than $0.25cm$, or in spheroidal ones with the same volume, can drug convection be increased by making vessels more leaky. For spheroidal shapes, the convection of drugs inside is higher than it is in spherical ones, and it seems that for more irregular shapes, which are generally found in the body due to limitations imposed by neighboring tissues and organs such as the brain, this effect is more marked. For shapes studied in this dissertation, results show that the dependency of the maximized flux on size is much stronger than its dependency on shape. It should be mentioned that due to very low diffusivity, the high permeability of vessels cannot support homogeneous distribution inside tumors because this high value results in more diffusive transport only in a narrow area around the vessels.

In real cases of solid tumors, instead of assuming uniform distribution of vessels, it is better to use tumor-induced microvasculature. There are different models of angiogenesis. This study presents modifications of some features of the previously presented continuous and discrete models. These modifications are on the initial distribution of fibronectin and TAF in the domain and also in the interpretation of the effect of MDE in the continuous and discrete models. One of the main advantages of this work is the realistic probability dis-

tribution in the domain. Fibronectin degradation is clearly shown to establish haptotactic movement, and in the absence of MDE, the expected haptotactic movement decreases.

Having set the capillary network, numerical simulation of fluid flow in normal and cancerous tissues was finally studied under three conditions: constant and uniform distribution of intravascular pressure in the whole domain, a rigid vascular network, and an adaptable vascular network. The effect of tumor-induced vascular networks on fluid flow in normal and cancerous tissues is also investigated, as are the numerical simulation for blood flow in a microvascular network and fluid flow in the interstitium. First, fluid flow in the normal and cancerous tissue is simulated without considering a network of vessels and uniform distribution and constant values for blood pressure in tissues. Results of this simulation show the distribution and values of interstitial pressure in the normal and cancerous tissues. Then, two vascular networks with different numbers of initial ECs on parent vessels are generated using a discrete angiogenesis method.

Two approaches to simulating blood flow in networks can be employed. The first approach neglects the effect of the non-continuum and adaptability of vessels and considers Poiseuille equation's parameters such as the diameter of vessels and blood viscosity in the network to be constant and ignores the phase separation of blood in vessel bifurcation. These numerical solutions show that the interstitial pressure value is at its maximum at the center of the tumor and decreases towards the periphery. Results show that the second, more realistic approach has better distribution of fluid flow that the first one. This second approach regards vessel diameter as adaptable (a function of hemodynamic and metabolic stimuli), and considers phase separation of red blood cells at bifurcation points. The blood viscosity depends on the diameter and hematocrit (Fahraeus Lindqvist effect). Still in the second approach, vessels far from a parent vessel have flow, but in the first approach, many of these vessels are eliminated because of their low flow rates. The interstitial pressure in these two approaches is higher than that shown in the modeling without a network and previous work by our group in which constant and uniform distribution of intravascular pressure was assumed. In the second approach to blood flow simulation, with a more-realistic model for blood and vessel diameter, results show the highest interstitial pressure in the solid region, a situation that results in lower values of drug delivered to this part of a solid tumor. This result confirms experimental data in the literature.

The problem studied in this thesis is fairly complicated even with respect to the current knowledge about transport phenomena in biological tissues. This work is, however, still a limited study in many respects. Some of the limitations are due to technical constraints. First of all, the main assumption was that drug and interstitial fluid have the same velocity. To consider a more-realistic model we should solve the concentration equation involving advection and diffusion terms. Although not presented in the thesis, this step has been done

for spherical and spheroidal solid tumors but not for tumors with heterogenious distribution of microvessels. However, we leave this topic for a future study numerically quantifing this effect in all different cases. In the angiogenesis model, a number of key assumptions merit more discussion. Other interesting areas needing investigation are missing from the literature, as listed below. We also leave these for future consideration.

- Study the 3D capillary network model of angiogenesis and investigate fluid flow and solute equations in this network,
- Study the effect of the size and physical properties of solid tumors and physicochemical properties of drugs,
- Improve current models to include nanoparticle drug delivery to solid tumors in which nanoparticles have a velocity different from that of fluid, based on a continuum approach that will result in a model as a function of time and space,
- Solve the solute and fluid equations simultaneously as a multi-scale problem in more irregular shapes of solid tumors, which are generally found in the body due to limitations imposed by neighboring tissues and structures such as the skull,
- Study the fluid and mass transport of nanoparticles and solve their governing equations in a solid tumor for which the structure is known completely from image processing methods such as high resolution MRI or micro CT,
- Improve the model used in this thesis to include the heterogeneity and discontinuous form of blood vessels in solid tumors, such as with a model based on the three well-known regions of a solid tumor,
- Consider tumor growth (in a dynamic model) based on network vasculature remodeling to show the effect of fluid flow on angiogenesis and capillary formation,
- Investigate the effect of angiogenesis inhibition on the resulting capillary network,
- Investigate in detail the haptotactic movemnt mechanism in the discrete model of angiogenesis,
- Use *in vivo* and *in vitro* studies to compare the effect of matrix density and angiogenesis inhibition on the resulting capillary network,
- Study the effect of interstitial pressure in the angiogenesis process,

- Carry out sensitivity analysis in a fluid flow model, and
- Investigate the effect of interstitial pressure in the remodeling process.

References

[1] Adair T. H., Montani J. P. *Angiogenesis*. Morgan and Claypool Life Sciences, 2010.

[2] Alarcon T., Byrne H. M., Maini P. K. A cellular automaton model for tumor growth in an inhomogeneous environment. *J. Theor. Biol.*, 225(2):257–274, 2003.

[3] Alarcon T., Owen M. R., Byrne H. M., Maini P. K. Multiscale modeling of tumor growth and therapy: The influence of vessel normalisation on chemotherapy. *Comput. Math. Methods. Med.*, 7(2):85–119, 2006.

[4] Anderson A. R. A. Chaplain M. A. J. Continuous and discrete mathematical models of tumor-induced angiogenesis. *Bull. Math. Biol.*, 60:857–900, 1998.

[5] Bauer A. L., Jackson T. L., Jiang Y. A cell-based model exhibiting branching and anastomosis during tumor-induced angiogenesis. *Biophys. J.*, 92(2):3105–3121, 2007.

[6] Bauer A. L., Jackson T. L., Jiang Y. Topography of extracellular matrix mediates vascular morphogenesis and migration speeds in angiogenesis. *PLoS. Comput. Biol*, 5(7):e1000445, 2009.

[7] Baxter L. T., Jain R. K. Transport of fluid and macromolecules in tumors. (I) Role of interstitial pressure and convection. *Microvasc. Res.*, 37(1):77–104, 1989.

[8] Baxter L. T., Jain R. K. Transport of fluid and macromolecules in tumors. (II) Role of heterogeneous perfusion and lymphatics. *Microvasc. Res.*, 40(2):246–263, 1990.

[9] Baxter L. T., Jain R. K. Transport of fluid and macromolecules in tumors. (III) Role of binding and metabolism. *Microvasc. Res.*, 41(1):5–23, 1991.

[10] Bear J. *Dynamics of fluids in porous media*. Dover Publications Inc., 1988.

[11] Bear J., Y. Bachmat. *Introduction to modeling of transport phenomena in porous media*. Kluwer Academic publishers, 1991.

[12] Blakeslee S. Impenetrable tumors found to block even the newest cancer agents. *The New York Times*, 1989.

[13] Boucher Y., Baxter L. T., Jain R. K. Interstitial pressure gradients in tissue-isolated and subcutaneous tumors: Implication for therapy. *Cancer Res.*, 50(15):4478–4484, 1990.

[14] Butler, T. P., Grantham, F. H., Gullino, P. M. Bulk transfer of fluid in the interstitial compartment of mammary tumors. *Cancer Res.*, 35(11):3084–3088, 1975.

[15] Cai Y., Xu S., Wu J., Long Q. Coupled modeling of tumour angiogenesis, tumor growth and blood perfusion. *J. Theor. Biol.*, 279(1):90–101, 2011.

[16] Campbell, N. A. *Biology*. The Benjamin/Cummings Publishing Co. Inc., 4th edition, 1996.

[17] Carmeliet P., Jain R. K. Angiogenesis in cancer and other diseases. *Nature*, 407:249–257, 2000.

[18] Chaplain M. A. J., McDougall S. R., Anderson A. R. A. Mathematical modeling of tumor-induced angiogenesis. *Annu. Rev. Biomed. Eng*, 8:233–257, 2006.

[19] Chapman S.J., Shipley R.J., Jawad R. Multiscale modeling of fluid transport in tumors. *Bull. Math. Biol.*, 70(8):2334–2357, 2008.

[20] Ciofalo M., Collins M. W., Hennessy T. R. *Nanoscale fluid dynamics in physiological processes, A review study* , chapter Microhydrodynamics phenomena in the circulation. WIT Press, 1999.

[21] Clague D. S., Phillips R. J. Hindered diffusion of spherical macromolecules through dilute fibrous media. *Phys. Fluids*, 8:1720–1731, 1996.

[22] Cope D. A., Dewhirst M. W., Friedman H. S., Bigner D. D., Zalutsky M. R. Enhanced delivery of a monoclonal antibody F(ab)2 fragment to subcutaneous human glioma xenografts using local hyperthermia. *Cancer Res.*, 50:1803–1809, 1990.

[23] Curry F. E. *Mechanics and thermodynamics of transcapillary exchange, Handbook of physiology, Section 2: The cardiovascular system*. Amer. Physiol. Soc., 1984.

[24] Darcy H. *Les Fontaines Publiques de la Ville de Dijon.* translated in English, 1856.

[25] de Boer R. *Theory of porous media: Highlights in the historical development and current state.* Springer, 2000.

[26] Deen W. M. Hindered transport of large molecules in liquid-filled pores. *AIChE*, 33(9):1409–1425, 1987.

[27] Dreher M. R., Liu W., Michelich C. R., Dewhirst M. W., Yuan F., Chilkoti A. Tumor vascular permeability, accumulation, and penetration of macromolecular drug carriers. *J. Natl. Cancer I.*, 98(5):335–344, 2006.

[28] Dykes P. W., Bradwell A. R., Chapman C. E., Vaughan A. T. M. Radioimmunotherapy of cancer: Clinical studies and limiting factors. *Cancer Treat. Rev.*, 14:87–106, 1987.

[29] El-Kareh A. W., Secomb T. W. Effect of increasing vascular hydraulic conductivity on delivery of macromolecular drugs to tumor cells. *Int. J. Radiation Oncology Biol. Phys.*, 32(5):1419–1423, 1995.

[30] Folkman J. Tumor angiogenesis: Therapeutic implications. *N. Engl. J. Med.*, 285:1182–1186, 1971.

[31] Folkman J. The vascularization of tumors. *Sci. Am.*, 234(5):58–64, 1976.

[32] Fung, Y. C.,. *Biomechanics-Mechanical properties of living tissues*, chapter Blood rheology in microvessels. Science Technique Publisher, China, 1986.

[33] Goh Y. M. F., Kong H. L., Wang C. H. Simulation of the delivery of doxorubicin to hepatoma. *Pharmaceutical Res.*, 18(6):761–770, 2001.

[34] Goldacre R. J., Sylven B. On the access of blood-borne dyes to various tumor regions. *Brit. J. Cancer*, 16:306–322, 1962.

[35] Gross J. F., Popel A. S. *Mathematical models of transport phenomena in normal and neoplastic tissue, Tumor blood circulation.* CRC Press, 1979.

[36] Gullino P. M. *Extracellular compartments of solid tumors, Cancer.* Plenum Press., 1975.

[37] Ivanchenko O., Sindhwani N., Linninger A. A. Experimental techniques for studying poroelasticity in brain phantom gels under high flow microinfusion. *J. Biomech. Eng.*, 132(5):051008, 2010.

[38] Jain R. K. Transport of molecules in the tumor interstitium: A review. *Cancer Res.*, 47:3039–3051, 1987a.

[39] Jain R. K. Transport of molecules across tumor vasculature. *Cancer Metastasis Rev.*, 6:559–594, 1987b.

[40] Jain R. K. Determinants of tumor blood flow: A review. *Cancer Res.*, 48:2641–2658, 1988a.

[41] Jain R. K. Transvascular and interstitial transport in tumors. *Vascular Endothelium in Health and Disease*, pages 215–220, 1988b.

[42] Jain R. K. Delivery of molecular and cellular medicine to solid tumors. *Adv. Drug. Deliv. Rev.*, 46:149–168, 2001.

[43] Jain R. K. Normalization of tumor vasculature: An emerging concept in antiangiogenic therapy. *Science*, 307:58–62, 2005.

[44] Jain R. K. Baxter L. T. Mechanisms of heterogeneous distribution of monoclonal antibodies and other macromolecules in tumors: significance of elevated interstitial pressure. *Cancer Res.*, 48:7022–7032, 1988.

[45] Jain R. K., Tong R. T., Munn L. L. Effect of vascular normalization by antiangiogenic therapy on interstitial hypertension, peritumor edema, and lymphatic metastasis. *Cancer Res.*, 67(6):2729–2735, 2007.

[46] Jain R. K., Ward-Hartley K. Tumor blood flow-characterization, modifications, and role in hyperthermia. *IEEE Trans. Sonics and Ultrason.*, 31:504–526, 1984.

[47] Jain R. K., Wei J. Dynamics of drug transport in solid tumors: Distributed parameter model. *J. Bioeng.*, 1:313–330, 1977.

[48] Jain R. K., Wei J., Gullino P. M. Pharmacokinetics of methotrexate in solid tumors. *J. Pharmacokinet. Biopharm.*, 7(2):181–194, 1979.

[49] Jang S. H., Wientjes M. G., Lu D., Au J. L. S. Drug delivery and transport to solid tumors. *Pharm. Res.*, 20(9):1337–1350, 2003.

[50] Johnson E. M., Berk D. A., Jain R. K., Deen W. M. Hindered diffusion in agarose gels: Test of effective medium model. *Biophys. J.*, 70(2):1017–1023, 1996.

[51] Jones P. L., Gallagher B. M., Sands H. Autoradiographic analysis of monoclonal antibody distribution in human colon and breast tumor xenografts. *Cancer Immunol. Immunother.*, 22(2):139–143, 1986.

[52] Kerbel R. S. Tumor angiogenesis. *N. Engl. J. Med.*, 358(19):2039–2049, 2008.

[53] Khawli L. A., LeBerthon B., Charak B. S., Mazumder A., Epstein A. L. Enhanced tumor uptake of monoclonal antibodies induced by a novel vasoactive immunoconjugate. *Antib. Immunoconjug. Radiopharm.*, 4:205, 1991.

[54] Kohler, G., Milstein, C. Continuous cultures of fused cells secreting antibody of predefined specificity. *Nature*, 256:495–497, 1975.

[55] LeBerthon B., Khawli L. A., Alauddin M., Miller G. K., Charak B. S., Mazumder A., Epstein A. L. Enhanced tumor uptake of macromolecules induced by a novel vasoactive interleukin 2 immunoconjugate. *Cancer Res.*, 51(10):2694–2698, 1991.

[56] Levin V. A., Patlak C. S. Landahl H. D. Heuristic modeling of drug delivery to malignant tumors. *J. Pharmacokinet. Biopharm.*, 8(3):257–296, 1980.

[57] Levine H. A., Pamuk S., Sleeman B. D., Nilsen-Hamilton M. Mathematical modeling of capillary formation and development in tumor angiogenesis: Penetration into the stroma. *Bull. Math. Biol.*, 63:801–863, 2001.

[58] Levine H. A., Tucker A. L. , Nilsen-Hamilton M. A mathematical model for the role of cell signal transduction in the initiation and inhibition of angiogenesis. *Growth Factors*, 20(4):155–175, 2002.

[59] Linninger A. A., Somayaji M. R., Erickson T., Guo X., Penn R. D. Computational methods for predicting drug transport in anisotropic and heterogeneous brain tissue. *J. Biomech.*, 41(10):2176–2187, 2008.

[60] Linninger A. A., Somayaji M. R., Zhang L., Hariharan M. S., Penn R. D. Rigorous mathematical modeling techniques for optimal delivery of macromolecules to the brain. *IEEE Trans. on Biomed. Eng.*, 55(9):2303–2313, 2008.

[61] Lutz R. J., Dedrick R. L., Straw J. A., Hart M. M., Klubes P., Zaharko D. S. The kinetics of methotrexate distribution in spontaneous canine lymphosarcoma. *J. Pharmacokinet. Biopharm.*, 3(2):77–97, 1975.

[62] Mantzaris N.V., Webb S., Othmer H.G. Mathematical modeling of tumor-induced angiogenesis. *J. Math. Biol.*, 49:111–187, 2004.

[63] McDougall S. R., Anderson A. R. A., Chaplain M. A. J. Mathematical modeling of dynamic adaptive tumour-induced angiogenesis: Clinical implications and therapeutic targeting strategies. *J. Theor. Biol.*, 241(3):564–589, 2006.

[64] McDougall S. R., Anderson A. R. A., Chaplain M. A. J., Sherratt J. A. Mathematical modeling of flow through vascular networks implications for tumor-induced angiogenesis and chemotherapy strategies. *Bull. Math. Biol.*, 64(4):673–702, 2002.

[65] Murray C. D. The physiological principle of minimum work. I. The vascular system and the cost of blood volume. *PNAS*, 12(3):207–214, 1926.

[66] Nakagawa H., Groothius D. R., Owens E. S., Fenstermacher J. D., Patlak C. S., Blasberg R. G. Dexamethasone effects on [125I] albumin distribution in experimental RG-2 gliomas and adjacent brain. *J. Cereb. Blood Flow Metab.*, 7(6):687–701, 1987.

[67] Netti P. A., Baxter L. T., Boucher Y., Skalak R. Jain R. K. Time-dependent behavior of interstitial fluid pressure in solid tumors: Implication for drug delivery. *Cancer Res.*, 55(22):5451–5458, 1995.

[68] Netti P. A., Hamberg L. M., Babich J. W., Kierstead D., Graham W., Hunter G. J., Wolf G. L., Fischman A., Boucher Y., Jain R. K. Enhancement of fluid filtration across tumor vessels: Implication for delivery of macromolecules. *PNAS*, 96(6):3137–3142, 1999.

[69] Netti P. A., Roberge S., Boucher Y., Baxter L. T., Jain R. K. Effect of transvascular fluid exchange on pressure-flow relationship in tumors: A proposed mechanism for tumor blood flow heterogeneity. *Microvasc. Res.*, 52(1):27–46, 1996.

[70] Orme M. E., Chaplain M. A. J. Two-dimensional models of tumour angiogenesis and anti-angiogenesis strategies. *IMA. J. Math. Appld. Med. Biol*, 14:189–205, 1997.

[71] Owen M. R. , Alarcon T., Maini P. K., Byrne H. M. Angiogenesis and vascular remodelling in normal and cancerous tissues. *J. Math. Biol.*, 58(4):689–721, 2009.

[72] Paweletz N., Knierim M. . Tumor-related angiogenesis. *Crit. Rev. Onco./Hema.*, 9(3):197–242, 1989.

[73] Phillips R. J. A hydrodynamic model for hindered diffusion of proteins and micelles in hydrogels. *Biophys. J.*, 79(6):3350–3353, 2000.

[74] Pozrikidis C. Numerical simulation of blood and interstitial flow through a solid tumor. *J. Math. Biol*, 60(1):75–94, 2010.

[75] Pozrikidis C., Farrow D. A. A model of fluid flow in solid tumors. *Ann. Biomed. Eng.*, 31(2):181–194, 2003.

[76] Press W. H., Flannery, B. P., Teukolsky, S. A., Vetterling, W. T. *Numerical recipes in FORTRAN 77: The art of scientific computing, 2nd ed.* Cambridge, England: Cambridge University Press, 1992.

[77] Pries A. R., Neuhaus D., Gaehtgens P. Blood viscosity in tube flow: Dependence on diameter and hematocrit. *Am. J. Physiol. Heart. Circ. Physiol.*, 263(6):1770–1778, 1992.

[78] Pries A. R., Reglin B., Secomb T. W. Structural adaptation of microvascular networks: Functional roles of adaptive responses. *Am. J. Physiol. Heart. Circ. Physiol*, 281(3):1015–1025, 2001.

[79] Pries A. R., Reglin B., Secomb T. W. Structural adaptation of vascular networks: Role of the pressure response. *Hypertension*, 38:1476–1479, 2001.

[80] Pries A. R., Secomb T. W. Modeling structural adaptation of microcirculation. *Microcirculation*, 15(8):753–764, 2008.

[81] Pries A. R., Secomb T. W., Gaehtgens P. Biophysical aspects of blood flow in the microvasculature. *Cardiovasc. Res.*, 32(4):654–667, 1996.

[82] Pries A. R., Secomb T. W., Gaehtgens P. Structural adaptation and stability of microvascular networks: Theory and simulations. *Am. J. Physiol. Heart. Circ. Physiol.*, 275(2):349–360, 1998.

[83] Qutub A. A., Gabhann F. M., Karagiannis E. D., Vempati P., Popel A. S. Multiscale models of angiogenesis. *IEEE Engineering in Medicine and Biology Magazine*, pages 14–31, 2009.

[84] Salathe E. P., An K. N. A mathematical analysis of fluid movement across capillary walls. *Microvasc. Res.*, 11(1):1–23, 1976.

[85] Saltzman W. M. Radomsky M. L. Drugs released from polymers: Diffusion and elimination in brain tissue. *Chem. Eng. Sci.*, 46(10):2429–2444, 1991.

[86] Sands H., Jones P. L. Physiology of monoclonal antibody accretion by tumors. *Cancer Treat. Res.*, 51:97–122, 1990.

[87] Sands H., Jones P. L., Shah S. A., Plame D., Vessella R. L., Gallagher B. M. Correlation of vascular permeability and blood flow with monoclonal antibody uptake by human clouser and renal cell xenografts. *Cancer Res.*, 48:188–193, 1988.

[88] Scheidegger A. E. *The physics of flow through porous media.* Univ. of Toronto Press, 1963.

[89] Senger D. R., Water L., Brown L. F., Nagy J. A., Yeo K. T., Yeo T. K., Berse B., Jackman R. W., Dvorak A. M., Dvorak H. F. Vascular permeability factor (VPF, VEGF) in tumor biology. *Cancer and Metastasis Rev.*, 12(3):303–324, 1993.

[90] Shamloo A., Heilshorn S. C. Matrix density mediates polarization and lumen formation of endothelial sprouts in VEGF gradients. *Lab Chip*, 10:3061–3068, 2010.

[91] Soltani M., Chen P. Shape design of internal flow with minimum pressure loss. *Advanced Science Letters*, 2:347–355, 2009.

[92] Soltani M., Chen P. Numerical modeling of fluid flow in solid tumors. *PLoS ONE*, 6(6):e20344, 2011.

[93] Soltani M., Chen P. Effect of tumor shape and size on drug delivery to solid tumors. *J. Biol. Eng.*, 6(4), 2012.

[94] Starling E. H. On the absorption of fluids from the connective tissue space. *J. Physiol.*, 19:312–326, 1896.

[95] Stauffer P. H. Flux flummoxed: A proposal for consistent usage. *Ground Water*, 44(2):125–128, 2006.

[96] Stephanou A., McDougall S. R., Anderson A. R. A., Chaplain M. A. J. Mathematical modeling of flow in 2D and 3D vascular networks: Applications to anti-angiogenic and chemotherapeutic drug strategies. *Math. Comput. Model.*, 41(10):1137–1156, 2005.

[97] Stephanou A., McDougall S. R., Anderson A. R. A., Chaplain M. A. J. Mathematical modeling of the influence of blood rheological properties upon adaptative tumour-induced angiogenesis. *Math. Comput. Model.*, 44(1):96–123, 2006.

[98] Stokes C. L., Lauffenburger D. A. Analysis of the roles of microvessel endothelial cell random motility and chemotaxis in angiogenesis. *J. Theor. Biol.*, 152(3):377–403, 1991.

[99] Tan W. H. K., Lee T., Wang C. H. Simulation of intratumoral release of Etanidazole: Effects on the size of surgical opening. *J. Pharm. Sci.*, 92(4):773–789, 2003.

[100] Tan W. H. K., Wang F., Lee T., Wang C. H. Computer simulation of the delivery of Etanidazole to brain tumor from PLGA wafers: Comparison between linear and double burst release systems. *Biotechnology and Bioengineering*, 82(3):278–288, 2003.

[101] Teo C. S., Tan W. H. K., Lee T., Wang C. H. Transient interstitial fluid flow in brain tumors: Effects on drug delivery. *Chem. Eng. Sci.*, 60(17):4803–4821, 2005.

[102] Vaughan A. T. M., Anderson P., Dykes P. W., Chapman C. E., Bradwell A. R. Limitations to the killing of tumors using radiolabelled antibodies. *Brit. J. Radiol.*, 60:567–578, 1987.

[103] Wang C. H., Li J. Three-dimensional simulation of IgG delivery to tumors. *Chem. Eng. Sci.*, 53(20):3579–3600, 1998.

[104] Wang C. H., Li J., Teo C. S., Lee T. The delivery of BCNU to brain tumors. *J. Controlled Release*, 61(1):21–41, 1999.

[105] Wiig H., Tveit E., Hultborn R., Reed R. K., Weiss L. Interstitial fluid pressure in DMBA-induced rat mammary tumors. *Scand. J. Clin. Lab. Invest.*, 42(2):159–164, 1982.

[106] Wood L., Kamm R., Asada H. Stochastic modeling and identification of emergent behaviors of an endothelial cell population in angiogenic pattern formation. *Int. J. Robot. Res.*, 30(6):659–677, 2011.

[107] Wu, J., Long, Q., Xu, S. *Modeling tumor vasculature: Molecular, cellular, and tissue level aspects and implications*, chapter 14 Blood perfusion in solid tumor with Normalized microvasculature. Springer, 2012.

[108] Wu J., Long Q., Xu S., Padhani A. R., Jiang Y. Simulation of 3D solid tumor angiogenesis including arteriole , capillary and venule. *Mol. Cell. Biomech.*, 5(4):217–227, 2008.

[109] Wu J., Xu S., Long, Q., Collins M. V., Konig G. S., Zhao G., Jiang Y., Padhani A. R. Coupled modeling of blood perfusion in intravascular , interstitial spaces in tumor microvasculature. *J. Biomech.*, 41(5):996–1004, 2008.

[110] Yang K. H., Fung W. P., Lutz R. J., Dedrick R. L., Zaharko D. S. In vivo methotrexate transport in murine lewis lung tumor. *J. Pharm. Sci.*, 68(8):941–945, 1979.

[111] Young J. S., Lumsden C. E., Stalker A. L. The significance of the tissue pressure of normal testicular and of neoplastic (Brown-Pearce carcinoma) tissue in the rabbit. *J. Pathol. Bacteriol.*, 62(3):313–333, 1950.

[112] Yuan F., Krol A., Tong S. Available space and extracellular transport of macromolecules: Effects of pore size and connectedness. *Ann. Biomed. Eng.*, 29(12):1150–1158, 2001.

[113] Zhao G. P., Chen E. Y., Wu J., Xu S. X., Collins M. W., Long Q. Two-dimensional discrete mathematical model of tumor-induced angiogenesis. *J. Appl. Math. Mech.*, 30(4):455–462, 2009.

[114] Zhao G., Wu J., Xu S., Collins M. W., Long Q., Konig C.S.,Jiang Y., Wang J., Padhani A. R. Numerical simulation of blood flow and interstitial fluid pressure in solid tumor microcirculation based on tumor-induced angiogenesis. *Acta. Mech. Sin.*, 23:477–483, 2007.

[115] Zhao J., Salmon H., Sarntinoranont M. Effect of heterogeneous vasculature on interstitial transport within a solid tumor. *Microvasc. Res.*, 73(3):224–236, 2007.